ABSTRACT

Title of dissertation: MAJORANA AND ANDREEV BOUND STATES IN SEMICONDUCTOR-SUPERCONDUCTOR NANOSTRUCTURES

Chun-Xiao Liu, Doctor of Philosophy, 2018

Dissertation directed by: Assistant Professor Jay Deep Sau
Department of Physics

Majorana bound states have been a topic of active research over the last decades. In the perspective of theoretical physics, Majorana bound states, which are their own antiparticles, are zero-energy quasi-particle excitations in exotic superconductive systems. From a technological perspective, Majorana bound states can be utilized for the implementation of fault-tolerant quantum computation due to their topological properties. For example, two well-separated Majorana bound states can form a fermionic qubit state, the quantum information of its occupancy is stored in a nonlocal way, being robust against local decoherence. Also since Majorana bound states obey non-Abelian statistics, quantum gates can be implemented by braiding. Such gate operations are robust because small deviations in braiding trajectories do not affect the braiding results.

So far the most promising platform for the realization of Majorana bound states is the one-dimensional semiconductor-superconductor nanostructures. The hallmark of the existence of Majorana bound states in such systems is a quantized zero-bias conductance peak in the tunneling spectroscopy for a normal-metal-superconductor junction. Although quantized zero-bias conductance peaks that

resemble the theoretical prediction have been observed in several experimental measurements, confusing aspects of the data muddy the conclusion. One source of confusion results from the existence of another type of excitation in these systems, i.e., the topologically trivial near-zero-energy Andreev bound states. These excitations mimic many behaviors of the topological Majorana bound states. In this thesis, we first investigate the tunnel spectrsocopy signatures of both Majorana and Andreev bound states. Then we discuss multiple proposals for differentiating between Majorana and Andreev bound states.

In Chapter 1, we give an overview for Majorana bound states in the context of both spinless p-wave superconductors and spin-orbit coupled nanowires in proximity with an s-wave superconductor. We also show how the existence of a zero-energy Majorana bound state leads to a quantized zero-bias conductance peak in tunneling spectroscopy at zero temperature. In Chapter 2, we discuss possible physical mechanisms responsible for the discrepancy between minimal theory of Majorana nanowire and real experimental observations. Specifically, we focus on the effect of dissipation inside the heterostructure. In Chapter 3, we show that a near-zero-energy Andreev bound state may arise quite generically in the semiconductor-superconductor nanowire in the presence of a smooth variation in chemical potential. Although such Andreev bound states are topologically trivial, they mimic the behaviors of the topological Majorana bound states in many aspects. In Chapter 4, we discuss multiple proposals for distinguishing between trivial Andreev bound states and topological Majorana bound states in the normal-metal-superconductor junction. In Chapter 5, we discuss a proposal for future experiments, i.e., a normal-superconductor-normal junction for a Coulomb blockaded superconductor. In this proposal, one can directly measure the topological invariant of the bulk superconductor. Finally Chapter 6 concludes the thesis.

MAJORANA AND ANDREEV BOUND STATES IN SEMICONDUCTOR-SUPERCONDUCTOR NANOSTRUCTURES

by

Chun-Xiao Liu

Dissertation submitted to the Faculty of the Graduate School of the
University of Maryland, College Park in partial fulfillment
of the requirements for the degree of
Doctor of Philosophy
2018

Advisory Committee:
Assistant Professor Jay Deep Sau, Chair/Advisor
Professor Sankar Das Sarma
Professor Victor M. Yakovenko
Assistant Professor James R. Williams
Professor Christopher Jarzynski

Acknowledgments

First and foremost, I thank my advisor Professor Jay Deep Sau for his mentorship and support over the years. As an advisor, he is always willing to interact with students, gives many helpful academic guidance and useful career path suggestions. As a physicist, he always comes up with novel and insightful ideas, and explains the physical picture in a clear and simple way. It is an enjoyable experience to work with him and explore the new fields of theoretical physics altogether. The thesis cannot be there if without his guidance.

I am also greatly indebted to my co-advisor Professor Sankar Das Sarma for his guidance and support. He has the taste for picking up important physical problems in the field. I always gained new insight when I worked on these problems. His immense knowledge over various fields of condensed matter physics broadens my knowledge a lot. When working closely with him, I can always feel his lasting passion for physics. I appreciate his suggestions on my career path.

I would like to thank Professors Victor M. Yakovenko, James R. Williams, and Christopher Jarzynski for serving on my dissertation committee.

I am very grateful to Professor Leo Kouwenhoven, Hao Zhang, and other people at Delft University of Technology for fruitful collaborations, through which I learnt the state of the art of the Majorana-related experiment. I am also very fortunate to work with Professor Maissam Barkeshli, Professor Tudor Stanescu on multiple projects.

I want to thank Professors Michael Levin, Adil Hassam, Xiangdong Ji, Theodore

R. Kirkpatrick, Raman Sundrum, Kaustubh Agashe, and Ted Jacobson for the informative graduate-level courses they taught.

I benefited a lot from the discussions with many postdoctoral researchers in CMTC – Ching-Kai Chiu, William S. Cole, Junhyun Lee, Xiao Li, Dong-Ling Deng, Shenglong Xu, Yi-Ting Hsu, Daniel Bulmash, Mike Schecter, Tom Iadecola, Yang Song, Jedediah H. Pixley, Xiaopeng Li, Bitan Roy, and Philip Brydon. They are always willing to share their expertise for physics and wisdom for life. I especially thank Ching-Kai Chiu also for many additional non-physics interactions like exploring national parks and playing board games together, which brought lots of fun to my life at leisure time.

I feel quite grateful to my PhD colleagues in CMTC – Setiawan, Hoi-Yin Hui, Yahya Alavirad, Ali Lavasani, Amit Nag, Yingyi Huang, Haining Pan, Sergey Pershoguba, Juraj Radic, Lance Boyer, Yi-Hua Lai and many others. Their great passion for theoretical condensed matter physics and their unique ways of doing research has influenced me positively. I will not forget the great pleasure of chatting with them while having a cup of coffee or tea.

I am lucky to have many friends in the department of physics – Renxiong Wang, Chiao-Hsuan Wang, Andi Tan, Ming Song, Prasoon Gupta, Seokjin Bae, Shavindra Premaratne, Qin Liu, Qile Zhang, Min Zhou, Yidan Wang, and many other friends outside the department. We had lots of good time together. They altogether made Maryland a wonderful place.

Finally, I want to thank my parents, grandparents and wife for their love and support. Especially, I owe most to my wife Shuang Liu who has shared every single

delightful and stressful moment in my PhD years and has been supportive for my career goals. I would have not made it so far without her love, care and support.

Table of Contents

List of Figures

List of Abbreviations

AB	Aharanov-Bohm
ABS	Andreev Bound State
AES	Ambegaokar-Eckern-Schön
BCS	Bardeen-Cooper-Schrieffer
BdG	Bogoliubov-de Gennes
BTK	Blonder-Tinkham-Klapwijk
HS	Hubbard-Stratonovich
MBS	Majorana Bound State
NS	Normal metal–Superconductor
NSN	Normal metal–Superconductor–Normal metal
SC	Superconductor/Superconductivity/Superconducting
SOC	Spin-Orbit Coupling / Spin-Orbit-Coupled
TQPT	Topological Quantum Phase Transition
TSC	Topological SuperConductor
ZBCP	Zero-Bias Conductance Peak
Φ_0	superconducting flux quantum $h/2e$

Chapter 1

Introduction

Majorana fermion was proposed in 1937 to be an elementary particle which is its own antiparticle [1]. Although 80 years have passed, Majorana fermions have yet to be detected as an elementary particle in high-energy physics. On other hand, in the context of condensed matter physics, people discovered that Majorana fermions [or equivalently Majorana bound states (MBS)] can be found as emergent zero-energy quasi-particle excitations inside the defects of some exotic p-wave superconductor [2, 3, 4, 5, 6, 7, 8]. What's more, on the side of applied technology, these MBSs in exotic superconductors can be utilized to work as quantum computing due to two of their unique properties [9, 10, 11, 12, 13, 14, 15, 16, 17, 18]. First, as two well-separated MBSs can form a nonlocal fermionic state, the quantum information of its occupancy is nonlocal and robust against any local decoherence effect. Second, MBSs of topological superconductors obey non-Abelian statistics when they are exchanged. So such type of braiding can implement quantum gates in a topological sense, because a small deviation in the braiding trajectory does not alter the braiding result.

Earlier proposals for MBS in condensed matter physics all require an exotic type of p-wave pairing in the superconductor(SC), which is quite rare in the real

nature world. Later on, however, people came up with the idea of heterostructures [19, 20, 21, 22, 23, 24]. In all these seminal works, a conventional s-wave superconductor is proximitized to a spin-polarized metallic phase, and the lowe-energy effective theory is a p-wave superconductor. These experimentally accessible proposals opened a new chapter for the field of Majorana fermions in condensed matter physics. Based on these proposals, a huge number of experimental progresses have been made in the following years [25, 26, 27, 28, 29, 30, 31, 32, 33, 34, 35, 36]. The excitement of the subject is also reflected in a number of review and popular articles [37, 38, 39, 40, 41, 42, 43, 44, 45].

Among these proposals, the most feasible one is the one-dimensional spin-orbit coupled(SOC) semiconductor nanowire proximitized by an s-wave SC in the presence of an external Zeeman field parallel to the axis of the nanowrie [20, 21, 22, 23]. When the Zeeman field exceeds the critical value, the superconductor will enter the topological phase and host a pair of MBSs at the wire ends. The most direct experimental measurement to detect MBSs is the tunneling spectroscopy of a normal-metal-supercoductor (NS) junction. In the presence of the mid-gap MBS, the tunnel conductance through the junction will show a zero-bias conductance peak(ZBCP) of height $2e^2/h$ at zero temperature [46, 47, 48, 49, 50]. Indeed, such predicted ZBCPs have been observed in many experimental setups. But there are still many discrepancies between theory and experiment. What's more, even in the absence of disorder, a smooth confinement potential could lead to a near-zero-energy Andreev bound state(ABS), mimicking most features of MBS.

In this thesis, we first discuss possible mechanisms that could explain the

discrepancy between theoretical prediction and experimental facts. We then talk about smooth potential-induced near-zero-bias peaks. Although they are topologically trivial ABS, they mimic most of the features of the topological MBS. We further give some theoretical proposal to differentiate these ABS and MBS. Finally, we go beyond NS junction and discuss a proposal for NSN junction, which measures the topological invariant in a direct way.

1.1 Spinless p-wave superconductivity

We first introduce a toy model whose low-energy effective Hamiltonian is described by unpaired Majorana fermions. This toy model was first proposed by A. Y. Kitaev in 2001 [2], which is the first theoretical model that hosts Majorana fermions in a one-dimensional nanowire system. Although it requires some stringent condition and therefore looks rather unrealistic, it captures most of the essential physics that will be helpful to the discussion of other heterostructure models. The Kitaev's model is a one-dimensional chain consisting of $L \gg 1$ sites:

$$H_{\mathrm{K}} = \sum_{j} \Big[-t(a_j^\dagger a_{j+1} + a_{j+1}^\dagger a_j) - \mu \left(a_j^\dagger a_j - \frac{1}{2} \right) + \Delta a_j a_{j+1} + \Delta a_{j+1}^\dagger a_j^\dagger \Big]. \quad (1.1)$$

Here t is a hopping amplitude, μ a chemical potential, and $\Delta = |\Delta| e^{i\theta}$ the induced SC gap. We can hide the dependence of the phase parameter into the definition of

electron creation and annihilation operators as

$$a_j \to e^{i\theta/2} a_j, \quad a_j^\dagger \to e^{-i\theta/2} a_j^\dagger. \tag{1.2}$$

Furthermore, every electron creation and annihilation operator can be decomposed into two Majorana operators

$$\gamma_{2j-1} = (a_j + a_j^\dagger)/\sqrt{2}, \quad \gamma_{2j} = (a_j - a_j^\dagger)/\sqrt{2}i, \quad j = 1, 2, ..., N \tag{1.3}$$

which satisfies the relations

$$\gamma_m^\dagger = \gamma_m, \quad \{\gamma_m, \gamma_l\} = \delta_{ml}, \quad m, l = 1, 2, ..., 2N. \tag{1.4}$$

In terms of these Majorana operators, the Hamiltonian becomes

$$H_{\rm K} = i \sum_j \Big[-\mu \gamma_{2j-1}\gamma_{2j} + (t + |\Delta|)\gamma_{2j}\gamma_{2j+1} + (-t + |\Delta|)\gamma_{2j-1}\gamma_{2j+2} \Big]. \tag{1.5}$$

There are two distinct universality classes for this model, which can be represented by the following two special cases.

(a) The trivial case (insulator): $|\Delta| = t = 0, \mu < 0$. Then

$$H_{\rm K} = -i\mu \sum_j \gamma_{2j-1}\gamma_{2j}. \tag{1.6}$$

The Majorana operators $\gamma_{2j-1}, \gamma_{2j}$ from the same site j are paired together to form

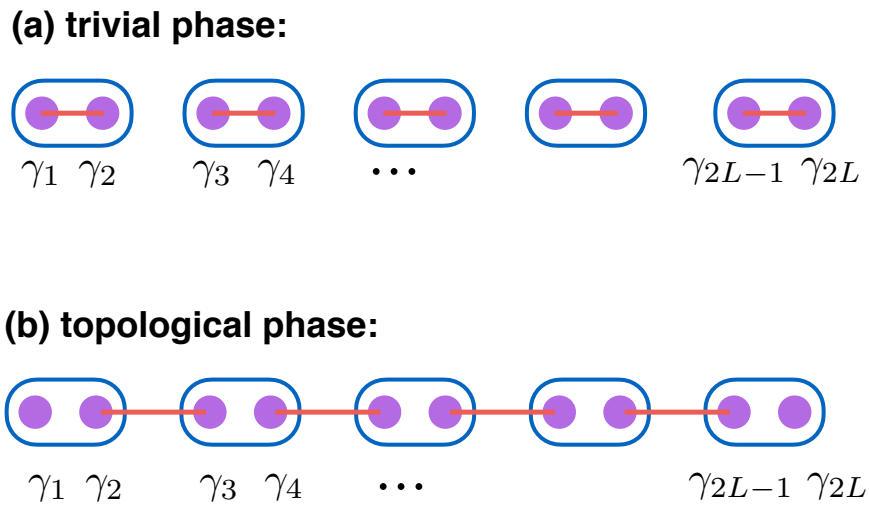

Figure 1.1: Schematic of the Kitaev chain with two distinct universality classes: (a) trivial phase with $|\Delta| = t = 0, \mu < 0$, and (b) topological phase with $|\Delta| = t > 0, \mu = 0$. The blue circle denotes the sites for the electrons, while the purple dots denotes the Majorana operators. Red lines represents the coupling between Majorana operators.

a ground state with the occupation number 0 on each site, and therefore the phase is an insulator.

(b) The topological case (TSC): $|\Delta| = t > 0, \mu = 0$.

$$H_{\mathrm{K}} = it \sum_j \gamma_{2j}\gamma_{2j+1}. \tag{1.7}$$

Now the Majorana operators $\gamma_{2j}, \gamma_{2j+1}$ from different sites are paired together. If we define a new fermionic operator

$$\widetilde{a}_j = (\gamma_{2j} + i\gamma_{2j+1})/\sqrt{2}, \quad \widetilde{a}_j^\dagger = (\gamma_{2j} - i\gamma_{2j+1})/\sqrt{2}, \tag{1.8}$$

and the Hamiltonian becomes

$$H_{\mathrm{K}} = t \sum_j (\widetilde{a}_j^\dagger \widetilde{a}_j - \frac{1}{2}). \tag{1.9}$$

Ground states should satisfies $\widetilde{a}_j|\psi\rangle = 0$ for $j = 1, 2, ...N-1$. On the other hand, the Majorana operators at the two ends of the nanowire, i.e., γ_1 and γ_{2L} remain unpaired, because they do not even enter the Hamiltonian. So if we define a fermionic mode in terms of these two Majorana operators:

$$b = (\gamma_1 + i\gamma_{2L})/\sqrt{2}, \quad b^\dagger = (\gamma_1 - i\gamma_{2L})/\sqrt{2}, \tag{1.10}$$

the ground state of the wire would be degenerate:

$$b|\psi_0\rangle = 0, \quad b|\psi_1\rangle = |\psi_0\rangle. \tag{1.11}$$

These two ground states have opposite fermionic parity. $|\psi_0\rangle$ has an even fermionic parity and $|\psi_1\rangle$ has an odd parity. It might seem that the two cases are special with fine-tuned parameters. However, they correspond to two distinct universality classes in this model. The phase in each universality class goes to the other only when the bulk gap in the system closes. So the conclusion holds for a quite general choice of parameters.

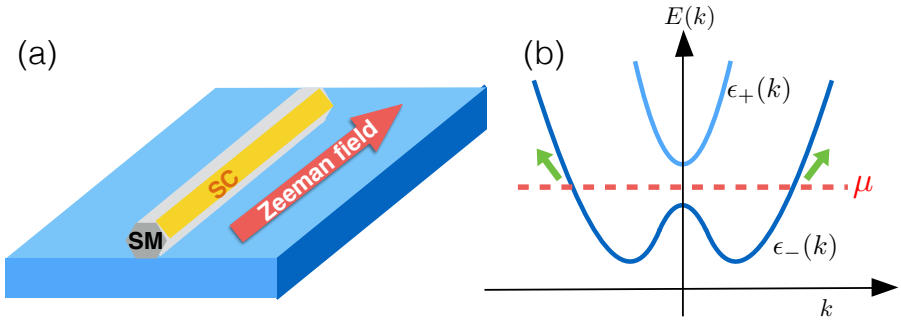

Figure 1.2: (a) Schematic of the one-dimensional SOC semiconducting nanowire proximitized by an s-wave SC. A Zeeman field is applied in parallel to the axis of the wire. (b) Band structure for one-dimensional hybrid nanowire (before proximity SC is included).

1.2 Superconductor-semiconductor hybrid nanowire

The proposal of SOC semiconducting nanowires in proximity with s-wave SC in the presence of external Zeeman field is so far the most promising proposal for realizing MBS in one-dimensional systems [20, 21, 22, 23]. The schematic is shown in Fig. 1.2(a). Almost all of the experimental groups nowadays are using such hybrid nanowire setups to search for MBS, because every single ingredient in the proposal is easy to access in the experimental lab. This thesis also focus on such hybrid nanowire structures, and therefore it is helpful to see why such type of one-dimensional nanowire can host MBS in the topological regime. The second quantized Hamiltonian for the superconductor-semiconductor hybrid nanowire is ($\hbar = 1$)

$$
\begin{aligned}
H_{\mathrm{NW}} &= \frac{1}{2}\int dx \Psi^\dagger(x) H_{\mathrm{BdG}}(x) \Psi(x), \\
H_{\mathrm{BdG}}(x) &= \left(-\frac{1}{2m^*}\partial_x^2 - i\alpha_R \partial_x \sigma_y - \mu\right)\tau_z + V_Z \sigma_x + \Delta \tau_x,
\end{aligned}
\tag{1.12}
$$

where m^* is the effective mass, α_R the SOC, μ the chemical potential, V_Z the Zeeman spin splitting field, and Δ induced SC gap. The Nambu spinor is $\Psi(x) = \left[c_\uparrow(x), c_\downarrow(x), c_\downarrow^\dagger(x), -c_\uparrow^\dagger(x)\right]^\intercal$. Before the inclusion of SC, we first transform the Hamiltonian of the SOC nanowire into the momentum space, and diagonalize the single-particle Hamiltonian to get the band structure $\epsilon_\pm(p)$ and eigenvectors. If we further assume that the chemical potential lies inside the Zeeman gap, there is only one Fermi point in half of the Brillouin zone and only the lower band is occupied. Now if we add the s-wave SC, the nanowire would be topological. We see this by looking at the Hamiltonian projected onto the lower band:

$$H_P = \sum_p \epsilon_-(p) c_-^\dagger(p) c_-(p) + \Delta_-(p) c_-^\dagger(-p) c_-^\dagger(p) + \text{H.c.}, \tag{1.13}$$

where the projected order parameter $\Delta_-(p) = i\alpha_R p\Delta/\sqrt{\alpha_R^2 p^2 + V_Z^2}$ has p-wave symmetry. The superconductor-semiconductor hybrid nanowire is effectively a spinless p-wave superconductor if only the lower band is occupied. A more careful calculation shows that the condition for the superconductor to become topological is

$$V_Z > \sqrt{\Delta^2 + \mu^2}. \tag{1.14}$$

When the Zeeman field is larger than the critical value $\sqrt{\Delta^2 + \mu^2}$ and the hybrid nanowire has open boundary, a pair of MBSs forms, with one being located at each end.

1.3 Perfect Andreev resonance of Majorana bound state

The most direct method of detecting MBS inside a topological superconductor is to measure the tunneling differential conductance through an NS junction. Figure 1.3 shows the schematic of such an experimental setup. Due to the fact that MBS is an zero-energy mode, and that Majorana fermion is its own anti-particle, the corresponding differential conductance through the NS junction would show a peak of height $2e^2/h$ at zero-bias voltage. Here we show the derivation of such a conductance feature using S-matrix method.

Quantum-mechanically, people can describe transport through the NS interface as a scattering problem. An incoming wave function Ψ_{in} propagates in the left metallic electrode, until it is reflected back at the interface with the superconductor, turning into an outgoing wave function Ψ_{out}. They are associated by the reflection matrix:

$$\begin{aligned} \Psi_{\text{out}} &= r(V)\Psi_{\text{in}}, \\ r(V) &= \begin{pmatrix} r_{ee} & r_{eh} \\ r_{he} & r_{hh} \end{pmatrix}. \end{aligned} \tag{1.15}$$

When the voltage in the normal metal V is less than the gap of the superconductor, there is no propagating mode inside the superconductor. All incoming electrons or holes will be reflected to the same electrode. Therefore, the reflection matrix is

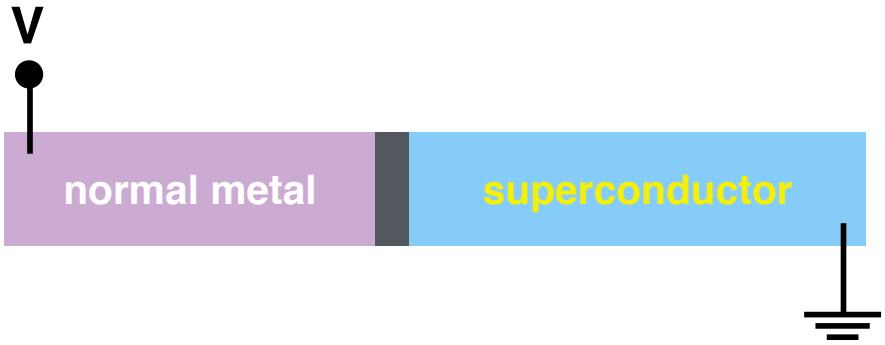

Figure 1.3: Schematic of the normal metal-superconductor(NS) junction. A bias voltage V is applied to the normal electrode (purple), while the superconductor electrode (blue) is grounded. A tunnel barrier (grey) lies at the interface between the two electrodes.

unitary:

$$r^\dagger r = 1,$$
$$|r_{ee}|^2 + |r_{he}|^2 = |r_{eh}|^2 + |r_{hh}|^2 = 1. \tag{1.16}$$

As we are considering a SC system, particle-hole symmetry is another crucial constraint for the scattering problem. Particle-hole symmetry relates the positive and negative eigenfunctions by an anti-unitary operator $P = \tau_x K$: $\Psi(-E) = P\Psi(E)$. Thus the corresponding reflection matrices are related by:

$$\tau_x r^*(-V)\tau_x = r(V). \tag{1.17}$$

A special point is the zero-bias voltage $V = 0$, which relates the reflection matrix

to itself:

$$\tau_x r_0^* \tau_x = r_0, \tag{1.18}$$

where $r_0 = r(0)$ is the reflection matrix at zero-bias voltage. Next, we focus on a quantity

$$Q = \det(r_0). \tag{1.19}$$

The particle-hole symmetry

$$Q = \det(r_0) = \det(\tau_x r_0^* \tau_x) = \det(r_0)^* = Q^* \tag{1.20}$$

constrains Q to be real. Unitarity constrains Q to be uni-modular,

$$1 = \det(r_0^\dagger r_0) = |\det(r_0)|^2 = |Q|^2. \tag{1.21}$$

Thus Q can only take two possible values

$$Q = \det(r_0) = |r_{ee}|^2 - |r_{he}|^2 = \pm 1. \tag{1.22}$$

Along with the unitarity condition Eq. (1.16), we see that at zero-bias voltage, the reflection is either perfect normal reflection $|r_{ee}| = 1$ or perfect Andreev reflection $|r_{he}| = 1$. The latter corresponds to the existence of MBS in the topological super-

conductor, which leads to the quantized zero-bias conductance:

$$G_0 = 1 - |r_{ee}|^2 + |r_{he}|^2 = 2|r_{he}|^2 = 2e^2/h. \tag{1.23}$$

So we see that for an NS junction, a quantized ZBCP of height $2e^2/h$ forms at zero temperature, provided that a MBS exists in the superconductor.

Chapter 2

Realistic simulation of Majorana nanowire

In this chapter, we carry out a realistic simulation of Majorana nanowires in order to understand the latest high quality experimental data [30, 34, 35] In the process, we develop a comprehensive picture for what physical mechanisms may be operational in realistic nanowires leading to discrepancies between minimal theory and experimental observations (e.g., weakness and broadening of the zero-bias peak and breaking of particle-hole symmetry). Our focus is on understanding specific intriguing features in the data, and our goal is to establish matters of principle controlling the physics of the best possible nanowires available in current experiments. We identify dissipation, finite temperature, multi-subband effects, and the finite tunnel barrier as the four most important physical mechanisms controlling the ZBCP. Our theoretical results including these realistic effects agree well with the best available experimental data in ballistic nanowires.

A recent tunneling experiment by Zhang *et al.* [30, 34, 35] in ballistic InSb nanowires in proximity to superconducting NbTiN provides by far the best measured ZBCP in the literature, with the measured ZBCP values reaching almost $0.5e^2/h$ above the background conductance. In addition, the measured tunneling conductance in Ref. [30, 34, 35] shows remarkable qualitative agreement with the

theoretical predictions in terms of magnetic field and gate voltage dependence, providing perhaps the strongest phenomenological evidence for the predicted existence of MBSs in nanowires. However, there are still some issues in the data [30, 34, 35] which appear to be incompatible with theoretical expectations. First, the ZBCP is still a factor of 5 smaller than the quantized MBS value in spite of the quoted experimental temperature being very low (~ 50 mK). Second, the ZBCP is broad covering essentially all of the topological gap instead of being sharply localized at zero bias. Third, the measured tunneling conductance manifestly breaks particle-hole (p-h) symmetry, which is considered to be an exact symmetry in superconductors. Fourth, the data do not reflect the expected "Majorana oscillations" [51, 52, 53, 54] as a function of magnetic field arising from the overlap of the two MBSs localized at the two ends of the nanowire. In addition, the finite-field topological gap is soft precisely where the ZBCP shows up. It is, therefore, unclear whether the measured tunneling conductance in Ref. [30, 34, 35] could be taken as unequivocal evidence in support of the existence of non-Abelian MBSs in nanowires.

In this chapter we carry out a realistic simulation of Majorana nanowires in order to understand the data of Ref. [30, 34, 35] and, in the process, develop a comprehensive picture for what physical mechanisms in realistic nanowires may lead to discrepancies between minimal theory and experimental observations (e.g., the breaking of p-h symmetry). There have been earlier works [53, 55, 54, 56, 57, 49, 58, 59, 60, 61, 62, 63] simulating various realistic aspects of Majorana nanowires, but our work has little overlap with them since our focus is on understanding specific intriguing features in the data of Ref. [30, 34, 35], and our goal is to establish matters

of principle controlling the physics of the best possible nanowires available in current experiments. Our reason for focusing on Ref. [30, 34, 35] is not only the high quality of its data with the large ZBCP and hard zero-field proximity gap, but also the fact that the ballistic nanowires used in Ref. [30, 34, 35] are relatively disorder free, thus eliminating the need to consider extrinsic disorder effects [64, 65, 66, 67, 68, 69, 70, 71, 72, 73].

2.1 Theoretical model

We use the following low-energy effective Hamiltonian for the Majorana nanowire [20, 22, 23]

$$\begin{aligned} \hat{H} &= \frac{1}{2}\int dx \hat{\Psi}^\dagger(x) H_{NW} \hat{\Psi}(x), \\ H_{NW} &= \left(-\frac{\hbar^2}{2m^*}\partial_x^2 - i\alpha_R \partial_x \sigma_y - \mu\right)\tau_z + V_Z \sigma_x + \Delta\tau_x - i\Gamma, \end{aligned} \tag{2.1}$$

where $\hat{\Psi} = \left(\hat{\psi}_\uparrow, \hat{\psi}_\downarrow, \hat{\psi}_\downarrow^\dagger, -\hat{\psi}_\uparrow^\dagger\right)^T$, and $\sigma_\mu(\tau_\mu)$ are Pauli matrices in spin (particle-hole) space. Some parameters are fixed by experimental measurements [30, 34, 35], e.g. effective mass $m^* = 0.015m_e$, induced SC gap $\Delta = 0.9$meV, and nanowire length $\sim 1.3\mu$m. Zeeman energy is $V_Z[\text{meV}] = 1.2B[T]$, based on an estimation $g_{\text{InSb}} \simeq 40$. The unknown parameters are spin-orbit coupling α_R, chemical potential μ, and the phenomenological dissipation parameter Γ [74] (which is further discussed below). The lead and barrier are also described by Eq. (2.1), but without the last two terms on the right-hand side, and with an additional on-site energy E that represents gate

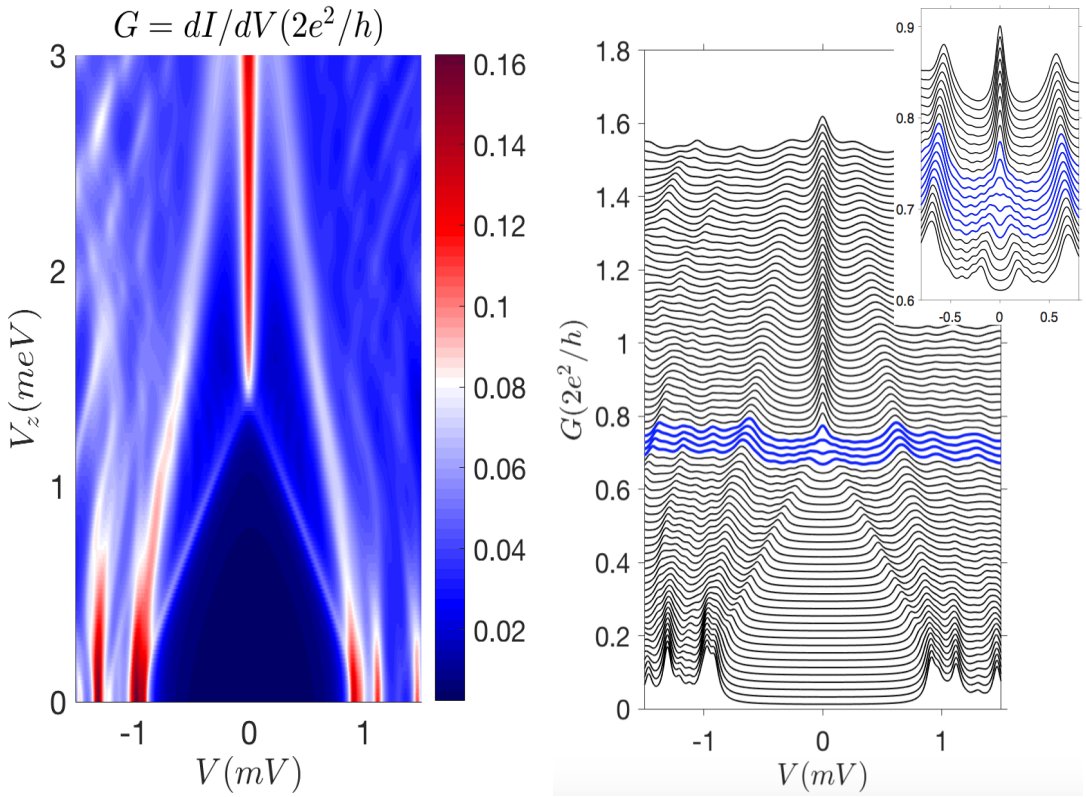

(a) (b)

Figure 2.1: (a) Best-fitting conductance. Gate voltage in the lead is assumed to give $E_{\text{lead}} = -20$ meV. The narrow barrier has width $D = 20$ nm and height $E_{\text{barrier}} = 30$ meV. (b) Linecuts from the data in (a) with vertical offsets $0.02 \times 2e^2/h$. Inset zooms into the region close to the topological phase transition with vertical offsets $0.01 \times 2e^2/h$.

voltage. Multi-subband effect is introduced by constructing two separate nanowires with different chemical potentials.

2.2 Best-fit conductance plot

Figure 2.1 shows the calculated conductance for the NS junction with optimal parameters, which agrees well with the data in Ref. [30, 34, 35]. The spin-orbit coupling parameter α_R, which controls the splitting of the ZBCP in a finite nanowire,

is chosen to be as large as $\alpha_R = 0.5$ eV$\mathring{A}$, since "Majorana oscillation" is not observed in experiments [30, 34, 35]. Chemical potentials of the two bands are tuned as $\mu_1 = 1$ meV, $\mu_2 = 5$ meV, such that within the regime $1.3 \lesssim V_Z < 3$ meV, only one band is topological. Due to such a difference in Fermi momentum of the two bands, barrier potential affects them differently: increasing barrier width would give larger side peaks, assuming the ZBCP is kept the same. Thus in order to match the data in Ref. [30, 34, 35] quantitatively, we choose a narrow barrier. The temperature in Fig. 2.1 is chosen to be $T = 50$ mK consistent with the quoted temperature in the experiment [30, 34, 35], and changing T to 100 mK does not change the results in Fig. 2.1(higher-T results are shown in Fig. 2.2). Dissipation of each band is assumed to depend on Zeeman field: $\Gamma_1 = 0.05(1 + 0.2V_Z)$ meV, $\Gamma_2 = 0.05(1 + V_Z)$ meV such that the side peaks are less obvious at large Zeeman energies, as observed experimentally (other choices for dissipation, including constant Γ, do not make any qualitative difference). One interesting feature is that a dip in conductance at zero bias grows into a peak when the system undergoes a topological phase transition [blue cutlines in Fig. 2.1(b)]. This general phenomenon is consistent with experimental observations [25, 27, 26, 28, 29, 75, 30, 32]. We also reproduce the finite-field soft gap feature as observed in Ref. [30, 34, 35] and other experiments.

2.3 Finite temperature

Finite temperature is one of the mechanisms that can explain the significant discrepancy between the theoretically predicted $T = 0$ quantized conductance

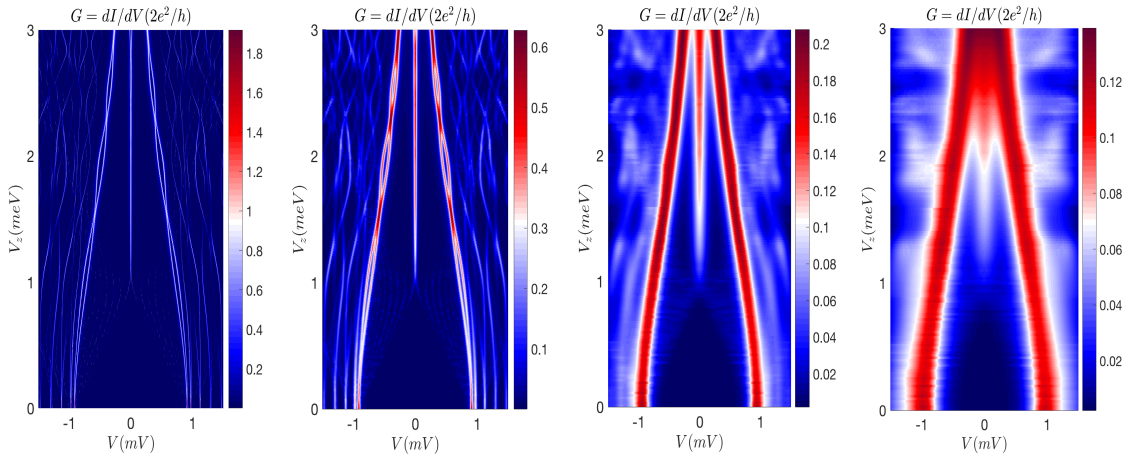

(a) $T = 0.0meV$ (b) $T = 0.01meV$ (c) $T = 0.05meV$ (d) $T = 0.1meV$

Figure 2.2: Tunneling conductance at different temperatures without dissipation. Finite temperature broadens the ZBCP and lowers its peak value simultaneously, without breaking any p-h symmetry. Chemical potential of the first band is $\mu_1 = 0$ meV. Only (a) is calculated by KWANT; others are generated by convolution.

$(2e^2/h)$ and the much lower value observed experimentally. The conductance at finite temperature is computed from the zero-temperature conductance (assuming we neglect the voltage dependence of the barrier) by a convolution with the derivative of Fermi distribution:

$$G_T(V) = -\int dE G_0(E) f_T'(E - V). \tag{2.2}$$

As shown in Fig. 2.2, with rising temperature, conductance profiles, including the ZBCP, get broadened and peak values go down without breaking any p-h symmetry. In this paper we consider temperature up to 0.1 meV $\sim$ 1.2 K [e.g., Figs. 2.2(d) and 2.4] Without dissipation, however, such a ZBCP width is then simply the thermal broadening.

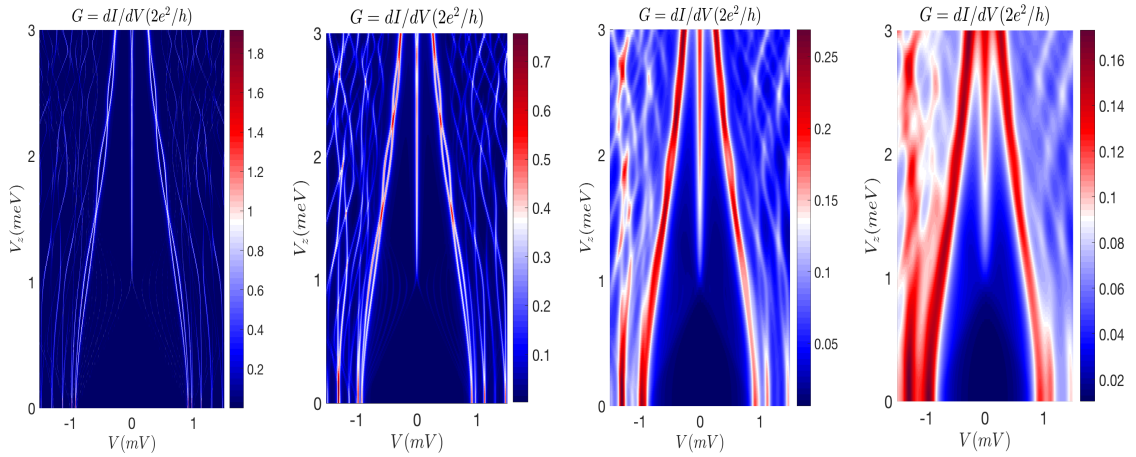

(a) $\Gamma = 10^{-4} meV$ (b) $\Gamma = 0.01 meV$ (c) $\Gamma = 0.05 meV$ (d) $\Gamma = 0.1 meV$

Figure 2.3: Tunneling conductance with various dissipation at zero temperature. Dissipation lowers the peak value of ZBCP and broadens its width. Furthermore, it breaks p-h symmetry in conductance at finite energies. Chemical potential of the first band is $\mu_1 = 0$ meV. All the four plots are generated by KWANT.

2.4 Dissipation

As we will argue later in the chapter, dissipation through a fermionic bath [74] appears critical to understanding certain features in the conductance data. Physically the dissipation considered here not only includes energy loss but also loss of fermions as in the presence of a fermion bath. At magnetic fields beyond the critical magnetic field, the superconductor becomes populated with vortices containing normal cores that can behave as a fermion bath. Additionally (and more importantly at lower magnetic fields) such dissipation may potentially arise from the combination of disorder and interaction. Disorder can lead to subgap states in the middle of the wire, which would not be visible in conductance. Electrons in the process of Andreev reflections from bound states at the end of the wire can decay into these deeper bound states through the interactions. This effectively leads to dissipation similar

to a fermion bath. The parent superconductor itself in the presence of disorder and vortices provides an additional dissipative mechanism. All these microscopic mechanisms are summarized phenomenologically into an imaginary part of the on-site energy (i.e., Γ) in Eq. (2.1). Numerical simulations including dissipation are shown in Fig. 2.3: dissipation broadens the conductance profile, including the ZBCP, and lowers their peak values (and also softens the gap somewhat). Furthermore, dissipation introduces p-h asymmetry into the conductance at finite energies, while the ZBCP is still p-h symmetric. This interesting phenomenon can be understood according to Refs. [76, 77, 78], where it is shown that for a tunneling system with a nonequilibrium distribution, the p-h symmetry of the conductance profile is respected only if there is no extra bath (i.e., no dissipation). In contrast, with an extra bath causing dissipation which is much larger than the tunneling amplitude, the result goes back to the standard theory of electron tunneling in the NS junction [79], i.e., conductance at positive (negative) energy is proportional to electron (hole) density of states at that energy, which is not necessarily p-h symmetric. We believe this is what is going on in the Majorana nanowire experiments where p-h symmetry breaking seems generic. Here we ignore p-h asymmetry caused by the unequal barrier due to voltage bias, since such trivial effect should be minimal for p-h asymmetry at low voltage [80] (and can also be easily experimentally checked). As Fig. 2.3 shows, when dissipation is negligible [Fig. 2.3(a)], the conductance is p-h symmetric. With increasing dissipation, p-h asymmetry shows up more explicitly until when the dissipation is large enough such that the ratio between conductance at positive and negative biased voltage reaches some limit, which is the ratio of elec-

tron and hole weight of the BdG eigenfunction at that energy. However, regardless of dissipation, the ZBCP profile itself is always p-h symmetric, because MBS always has equal electron and hole weights. We therefore conclude that dissipation has qualitatively the same effect on the ZBCP strength (see Fig. 2.4) as finite temperature: both broaden and lower the ZBCP without breaking its p-h symmetry, and it is thus difficult to disentangle the two effects from the ZBCP. For conductance at finite energies, dissipation produces p-h asymmetry while temperature does not.

2.5 Temperature versus dissipation effects on ZBCP

Following the previous discussion, Fig. 2.4 gives a quantitative comparison, showing how the peak value and full width at half maximum (FWHM) of ZBCP vary with dissipation and temperature respectively. Both effects give almost identical variation of ZBCP profile, indicating that the huge discrepancy between the quoted temperature ($\sim 50mK$) and the peak value of ZBCP can be explained by dissipation mechanism, since at $T = 50mK$ (without any dissipation) the ZBCP value should be close to $2e^2/h$.

2.6 Particle-hole asymmetry at superconducting gap

While the inclusion of dissipation allows the possibility of p-h symmetry breaking it does not guarantee it, e.g., the conductance in the so-called tunneling (dissipation dominated) limit to a conventional BCS superconductor without spin-orbit or Zeeman fields [81] is known to be p-h symmetric. However, in the experimental

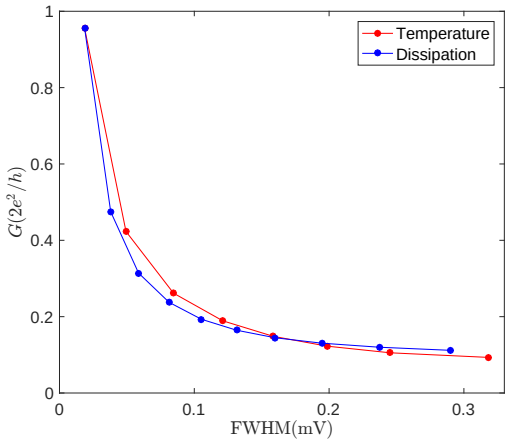

Figure 2.4: The peak value and FWHM of ZBCP for temperature and dissipation. Data points on the red curve are obtained at increasing temperature but without dissipation, while points on the blue curve are obtained with increasing dissipation at $T = 0$. $V_Z = 2$ meV, $\mu_1 = 0$ meV.

data [30, 34, 35], the SC gap at positive and negative biased voltages shows explicit p-h asymmetry. From the conventional theory of an s-wave superconductor, the p-h symmetry at and in the vicinity of the SC gap is due to the pair of Bogoliubov quasi-particles with the same excitation energy above and below the Fermi surface, and the small ratio of Δ/μ [79]. For the second band with $\mu_2 = 5$meV, the second condition is well satisfied, but its large SC coherence length would bring in significant finite-size effect. Therefore the quasi-particle pairs might not have the same excitation energy, causing p-h asymmetry at the order of (ξ/L). Put in another way, the p-h asymmetry at the SC gap arises because dissipation is less than the level spacing of the finite nanowire. In addition, the way of p-h symmetry breaking is random, i.e., either the electron or hole part could have larger contribution, depending on the relative position of the pair of quasi-particle excitations. Based on these arguments, the p-h asymmetry of the SC gap in the second band should decrease

with increasing nanowire length. For the first band ($\mu \sim 1$ meV), its large SC gap compared to the Fermi energy and the missing of the excitation branch below the Fermi surface at some threshold energy both can cause p-h asymmetry.

2.7 Conclusion

Through realistic simulations of Majorana nanowires and detailed comparison with recent experiments [30, 34, 35] we have identified dissipation, temperature, multi-subband, and finite barrier as the important physical mechanisms controlling MBS tunneling conductance properties. Our theoretical results agree well with recent experimental data including the puzzling observation of the breaking of the particle-hole symmetry.

Chapter 3

Andreev bound states in Majorana nanowire

In this chapter, we theoretically consider the interplay between Andreev and Majorana bound states in disorder-free quantum dot-nanowire semiconductor systems with proximity-induced superconductivity in the presence of spin-orbit coupling and Zeeman spin splitting (induced by an external magnetic field). The quantum dot induces ABSs in the SC nanowire which show complex behavior as a function of magnetic field and chemical potential, and the specific question is whether two such ABSs can come together forming a robust zero-energy topological MBS. We find generically that the ABSs indeed have a high probability of coalescing together producing near-zero-energy midgap states as Zeeman splitting and/or chemical potential are increased, but this mostly happens in the nontopological regime below the topological quantum phase transition(TQPT) although there are situations where the ABSs could indeed come together to form a zero-energy topological MBS. The two scenarios (two ABSs coming together to form a nontopological almost-zero-energy ABS or to form a topological zero-energy MBS) are difficult to distinguish just by tunneling conductance spectroscopy since they produce essentially the same tunneling transport signatures. We find that the "sticking together" propensity of ABSs to produce an apparent stable zero-energy midgap

state is generic in class D systems in the presence of superconductivity, spin-orbit coupling, and magnetic field, even in the absence of any disorder. We also find that the conductance associated with the coalesced zero-energy nontopological ABS is non-universal and could easily be $2e^2/h$ mimicking the quantized topological Majorana zero-bias conductance value.

A key experimental paper by Deng *et al.* has recently appeared in the context of ZBCPs in semiconductor-superconductor hybrid systems [31], which forms the entire motivation for the current theoretical work. In their work, Deng *et al.* studied tunneling transport through a hybrid system composed of a quantum dot-nanowire-superconductor, where no SC is induced in the quantum dot (i.e., the superconductivity is induced only in the nanowire). In Fig. 3.1, we provide a schematic of the experimental system, where the dot simply introduces a confining potential at one end of the nanowire which is covered by the superconductor to induce the proximity effect. Such a quantum dot may naturally be expected to arise because of the Fermi energy mismatch of the lead and the semiconductor much in the way a Schottky barrier arises in semiconductors. Reducing the potential barrier at the lead-semiconductor interface to produce a strong conductance signature likely requires the creation of a quantum dot as shown in Fig. 3.1. Thus a quantum dot might be rather generic in conductance measurements, i.e., one may not have to introduce a real quantum dot in the system although such a dot did exist in the set-up of Ref. [31]. The quantum dot may introduce ABSs in the nanowire, and the specific issue studied in depth by Deng *et al.* is to investigate how these ABSs behave as one tunes the Zeeman spin splitting and the chemical potential in the nanowire by

applying a magnetic field and a gate potential respectively. It is also possible that the ABSs in the Deng *et al.* experiment arise from some other potential fluctuations in the nanowire itself which is akin to having quantum dots inside the nanowire arising from uncontrolled potential fluctuations associated with impurities or inhomogeneities. (We consider both cases, the dot being outside or inside the nanowire, in this work.) The particular experimental discovery made by Deng *et al.*, which we theoretically examine in depth, is that ABSs may sometimes come together with increasing Zeeman splitting (i.e., with increasing magnetic field) to coalesce and form zero-energy states which then remain zero-energy states over a large range of the applied magnetic field, producing impressive ZBCPs with relatively large conductance values $\sim 0.5e^2/h$. Deng *et al.* speculate that the resulting ZBCP formed by the coalescing ABSs is a direct signature of MBSs, or in other words, the ABSs are transmuting into MBSs as they coalesce and stick together at zero energy. It is interesting and important to note that the sticking together property of the ABSs at zero energy depends crucially on the gate voltage in Deng *et al.* experiment, and for some gate voltage, the ABSs repel away from each other without coalescing at zero energy and at still other gate voltages, the ABSs may come together at some specific magnetic field, but then they separate out again with increasing magnetic field producing a beating pattern in the conductance around zero bias. Our goal in the current work is to provide a detailed description of what may be transpiring in the Deng *et al.* experiment within a minimal model of the dot-nanowire-superconductor structure elucidating the underlying physics of ABS versus MBS in this system. In addition, we consider situations where the quantum dot is, in fact, partially (or

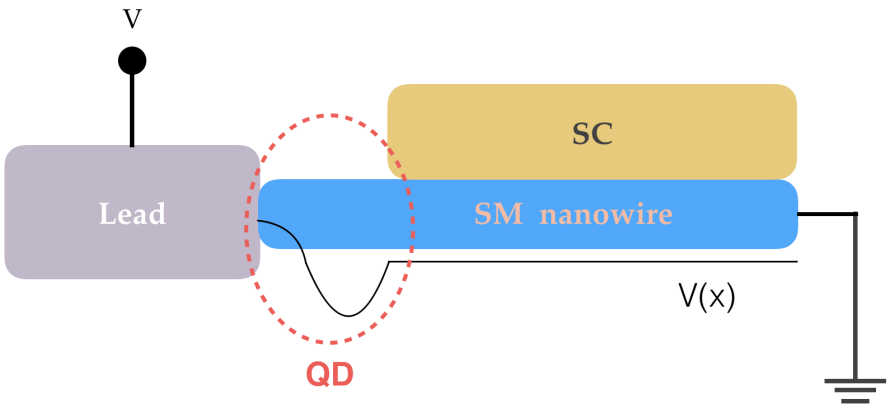

Figure 3.1: A schematic plot of the junction composed of lead and quantum dot-nanowire-superconductor hybrid structure. A semiconductor (SM) nanowire is mostly covered by a parent s-wave superconductor. One fraction of the nanowire is not covered by the SC and is subject to a smooth confinement potential. This part (encircled by the red dash line) between the lead and the superconducting nanowire is called quantum dot.

completely) inside the nanowire (i.e., the dot itself is totally or partially superconducting due to proximity effect), which may be distinct from the situation in Deng *et al.* experiment [31] where the quantum dot is not likely to be proximitized by the superconductor although any potential inhomogeneity inside the wire would act like a quantum dot in general for our purpose. Specific details of how the ABSs arise in the nanowire are not important for our theory as most of the important new qualitative features we find are generic as long as ABSs are present in the nanowire.

3.1 Theoretical model

It may be important here to precisely state what we mean by a "quantum dot" in the context of our theory and calculations. The "quantum dot" for us is simply a potential fluctuation somewhere in or near the wire which produces ABSs in

the system. This "quantum dot", being strongly coupled to the nanowire (perhaps even being completely inside the nanowire or arising from the Schottky barrier at the tunnel junction), does not have to manifest any Coulomb blockade as ordinary isolated quantum dots do. In fact, our theory does not include any Coulomb blockade effects because the physics of ABS transmuting into MBS or not is independent of Coulomb blockade physics (although the actual conductance values may very well depend on the Coulomb energy of the dot). The situation of interest to us is when the confined states in the dot extend into the nanowire (or are entirely inside the nanowire) so that they become ABSs. In situations like this, perhaps the expression "quantum dot" is slightly misleading (since there may or may not be any Coulomb blockade here), but we use this expression anyway since it is convenient to describe the physics of ABSs being discussed in our work.

The proximitized nanowire and the normal lead have exactly the same BdG Hamiltonian as Eq. (2.1), except in some discussions and calculated results we also replace the SC pairing term by a more complex self-energy term to mimic renormalization effects by the parent superconductor [82]:

$$\Sigma(\omega) = -\lambda \frac{\omega\tau_0 + \Delta(V_Z)\tau_x}{\sqrt{\Delta(V_Z)^2 - \omega^2}},$$
$$\Delta(V_Z) = \Delta_0 \sqrt{1 - (V_Z/V_{Zc})^2} \tag{3.1}$$

The quantum dot Hamiltonian is

$$H_{QD} = \left(-\frac{\hbar^2}{2m^*}\partial_x^2 - i\alpha_R \partial_x \sigma_y + V(x) - \mu \right) \tau_z + V_Z \sigma_x,$$
$$V(x) = V_D \cos(\frac{3\pi x}{2l}) \tag{3.2}$$

where $V(x)$ is the confinement potential. (We have ensured that other models for confinement potential defining the dot do not modify our results qualitatively.) The quantum dot size l is only a fraction of the total nanowire length L. The quantum dot is non-SC at this stage although later (in Sec. 3.4) we consider situations where the dot could have partial or complete induced superconductivity similar to the nanowire. We emphasize that there is no disorder in our model distinguishing it qualitatively from earlier work [83, 84, 85] where class D zero bias peaks in this context arise from disorder effects. Given this quantum dot-nanowire model, our goal is to calculate the low lying energy spectrum and the differential conductance of the system varying the chemical potential and the Zeeman splitting in order to see how any dot-induced ABSs behave. The specific goal is to see if we can qualitatively reproduce the key features of the Deng *et al.* experiment in a generic manner without fine-tuning parameters. Our goal is not to demand a quantitative agreement with the experimental data since too many experimental parameters are unknown(confinement potential, chemical potential, tunnel barrier, superconductor-semiconductor coupling, spin-orbit coupling, effective mass, Lande g-factor, etc.), but we do want to see whether ABSs coalesce generically and whether such coalescence around zero energy automatically implies a transmutation of ABSs into

MBSs.

3.2 Tunneling differential conductance

In nanowire tunneling experiments quantum dot physics is quite generic, and it may appear at the interface between the nanowire and the lead due to Schottky barrier effects as mentioned previously, since all that is needed is a small potential confinement region in between the lead and the wire which is non-SC. In our model, the only role played by the quantum dot potential is to introduce ABSs in the nanowire, and hence, if an experiment observes in-gap ABS in the superconducting nanowire, we model that by a "quantum dot" strongly coupled to the nanowire. In this section, we calculate the differential conductance of generic hybrid structures, for which the Hamiltonian is a combination of the nanowire Eq. (2.1) and the quantum dot Eq. (3.2).

3.2.1 Scan of Zeeman field

The calculated differential conductance through the dot-nanowire hybrid structure as a function of Zeeman field at various fixed chemical potentials ($\mu = 3.0,\ 3.8,\ 4.5$ meV) is shown in Fig. 3.2. Finite temperature $T = 0.02$ meV is introduced by a convolution between zero-temperature conductance and derivative of Fermi-Dirac distribution as Eq. (2.2). In each panel of Fig. 3.2, a pair of ABS-induced conductance peaks at positive and negative bias voltage tend to come close to each other when the Zeeman field is turned on. At finite Zeeman field (~ 1.5 meV), these two ABS

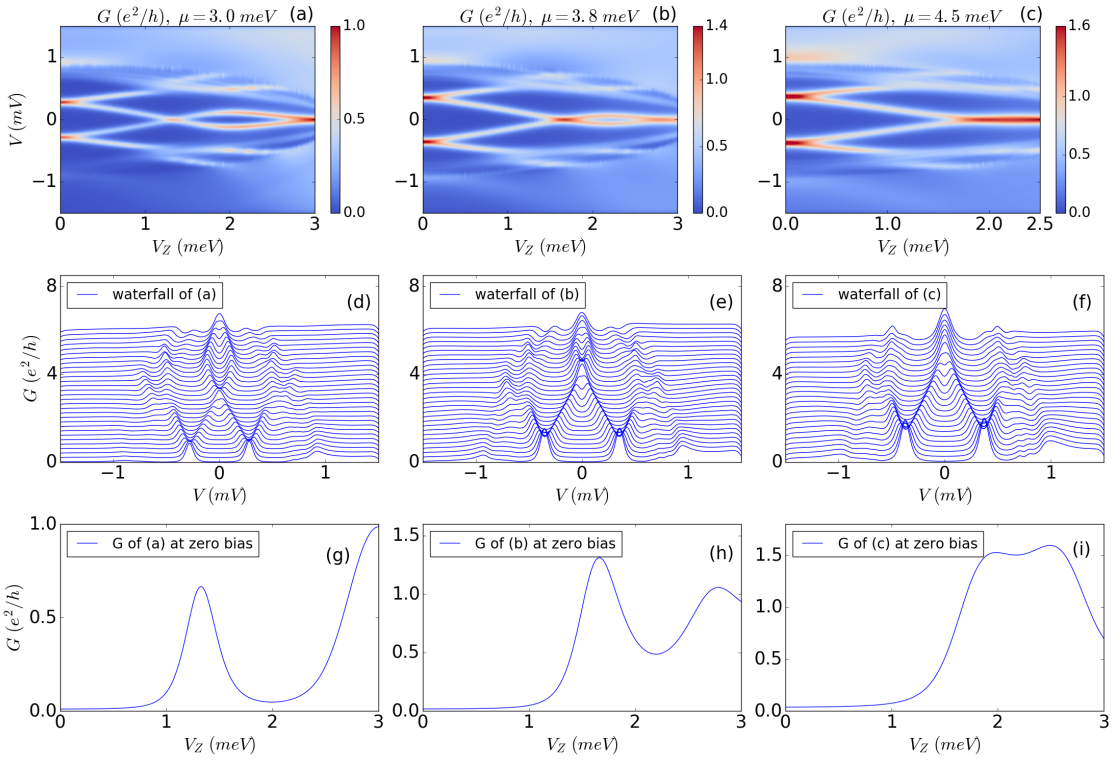

Figure 3.2: The calculated differential conductance through the dot-nanowire hybrid structure as a function of Zeeman field at various fixed chemical potentials ($\mu = 3.0,\ 3.8,\ 4.5$ meV) at $T = 0.02$ meV. (a)-(c) Conductance color plot as a function of Zeeman field and bias voltage. (d)-(f) "Waterfall" plots of conductance line cuts for different V_Z (increasing vertically upward by 0.1 meV for each line) corresponding to panels (a)-(c), respectively. (g)-(i) Calculated zero-bias conductance corresponding to panels (a)-(c), respectively. Note that these results include self-energy renormalization correction for the proximity effect.

peaks either cross zero bias and beat [Figs. 3.2(a) and (b)] or stick with each other near zero energy [Fig. 3.2(c)], all of which are similar to the observations in the Deng *et al.* experiment [31]. However these near-zero-energy peaks, especially the ZBCP formed by sticking of two ABSs, are all topologically trivial ABS peaks in Fig. 3.2 because $V_Z < \sqrt{\mu^2 + \Delta^2}$ with the Zeeman splitting explicitly being less than the critical value necessary for the TQPT. We emphasize that experimentally the TQPT critical field is unknown whereas in our theory we know it by definition. If we did not know the TQPT point, there was no way to discern (just by looking at these conductance plots) whether the ZBCP in Fig. 3.2 arises from trivial or topological physics! The generic beating or accidental sticking behavior from the coalesced ABS pair is the consequence of the renormalization of the bound states in the quantum dot in proximity with nanowire in the presence of Zeeman splitting and spin-orbit coupling, which has little to do with topology and Majorana. All we emphasize here is that coalescence of ABS pairs into a ZBCP [as in Fig. 3.2(c)] cannot be construed as ABSs merging into MBSs without additional supporting evidence. In Figs. 3.2(d)-(f) we provide further details by showing "waterfalls" patterns of conductance for increasing V_Z corresponding to the results in Figs. 3.2(a)-(c), respectively, whereas in Figs. 3.2(g)-(i) we show the calculated zero-bias conductance as a function of V_Z for results in Figs. 3.2(a)-(c), respectively.

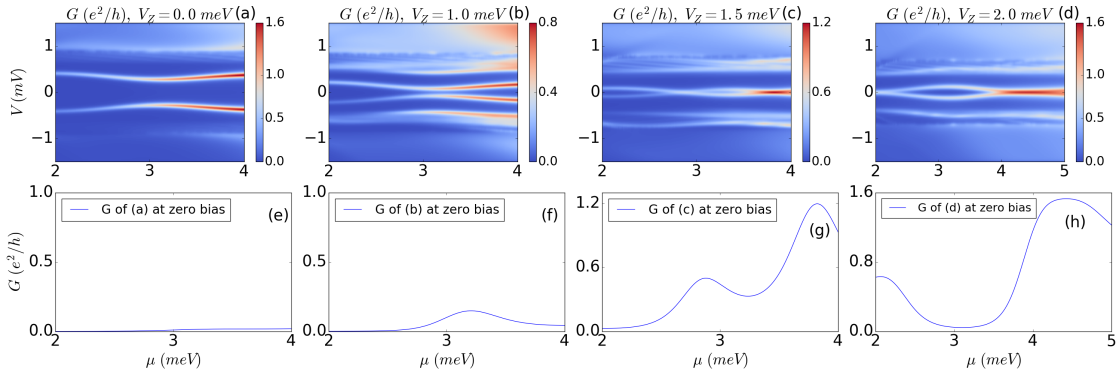

Figure 3.3: Calculated differential conductance through the hybrid structure as a function of chemical potential at various Zeeman fields at $T = 0.02$ meV. In (a) and (b), the ABS conductance peaks repel away from each other without coalescing at zero energy. In (c) the ABS peaks come together at some specific magnetic field, and beat with increasing chemical potential. In (d) ABS peaks beat and stick with each other. However, all of these near-zero-energy peaks are topologically trivial because $V_Z < \sqrt{\mu^2 + \Delta^2}$. In panels (e)-(h) we show the calculated zero-bias conductance corresponding respectively to panels (a)-(d) as a function of chemical potential at fixed V_Z. Note that the TQPT happens here at low $V_Z < 2.0$ meV (not shown).

3.2.2 Scan of chemical potential

Calculated differential tunnel conductance through the dot-nanowire hybrid structure as a function of chemical potential at various Zeeman fields at $T = 0.02$ meV is shown in Fig. 3.3. In Fig. 3.3(a) and (b), the ABS-induced conductance peaks repel away from each other without coalescing at zero energy. In Fig. 3.3(c) the ABS peaks come together at some specific magnetic field, and beat with increasing chemical potential. In Fig. 3.3(d) ABS peaks beat and stick with each other. All these features are similar to observations in the Deng *et al.* although the relevant variable in the experiment is a gate voltage whose direct relationship to the chemical potential in the wire (our variable in Fig. 3.3) is unknown, precluding any kind of direct comparison with experiment [31]. But all of these near-zero-energy peaks are

topologically trivial in our results of Fig. 3.3 because $V_Z < \sqrt{\mu^2 + \Delta^2}$ everywhere. We show in Figs. 3.3(d)-(f) the calculated zero-bias conductance corresponding to Figs. 3.3(a)-(c) respectively. Again, sticking together of ABSs at zero energy producing impressive ZBCP peaks are not sufficient to conclude that topological MBSs have formed. In Fig. 3.3, all the results are nontopological.

We note that the ABSs sticking to almost zero energy and producing trivial ZBCPs generically happen only for larger values of chemical potential (as should be obvious from Figs. 3.2 and 3.3) with the ABSs tending to repel away from each other or not quite stick to zero [e.g., Figs. 3.3(a) and (b)] for $\mu < \Delta$. We find this to be a general trend. Unfortunately, the chemical potential is not known in the experimental samples.

3.3 Understanding near-zero-energy ABS from reflection matrix theory

The absence of level repulsion in symmetry class D enhances the likelihood of a pair of levels sticking together at zero energy as some parameter such as the Zeeman splitting or the chemical potential is varied as discussed throughout this chapter. Despite this generic fact associated with symmetry class D that describes systems containing Zeeman splitting, spin-orbit coupling and superconductivity, the range of Zeeman splitting over which the spectrum sticks is not guaranteed to be large. In fact, the range of Zeeman field is typically not large for most disordered Hamiltonian [83]. In the experiment [31] and in our simulations (with quantum dots,

but no disorder), however, the zero-sticking propensity of trivial ABSs extends over a large range of Zeeman splitting (V_Z).

A more specific mechanism that provides a relatively robust (compared to the usual disordered class D) near-zero-energy states within symmetry class D involves the so-called smooth confinement [86, 55, 87]. The essential idea is that large Zeeman splitting (V_Z) compared to SC pairing (Δ) suppresses conventional s-wave pairing compared to p-wave pairing leading to a tendency for the formation of Majorana states at the end of the system for each spin-polarized channel in the nanowire. However, the end potential typically scatters between the different channels and gaps the Majorana fermions out, i.e., an MBS splitting develops. If the inter-channel scattering between different channels is weak then this Majorana splitting is small and there is a near-zero-energy state in such a potential. This near-zero-energy mode is, however, nontopological as it is arising from split Majorana modes at the wire end. Thus, the ABS producing the ZBCP is a composite of two MBSs, only one of which contributes to tunneling, leading to a robust almost-zero mode in the trivial regime.

In subsection 3.3.1, we will first show the energy spectra for the quantum dot-proximitized nanowire hybrid structure using various parameters (e.g., chemical potential μ, nanowire length L, dot length l, etc.) in order to show the trend of zero-energy sticking in the parameter regime. Second in subsection 3.3.2, we use reflection matrix theory to explain why such zero-sticking bound states exist in the relevant parameter regime.

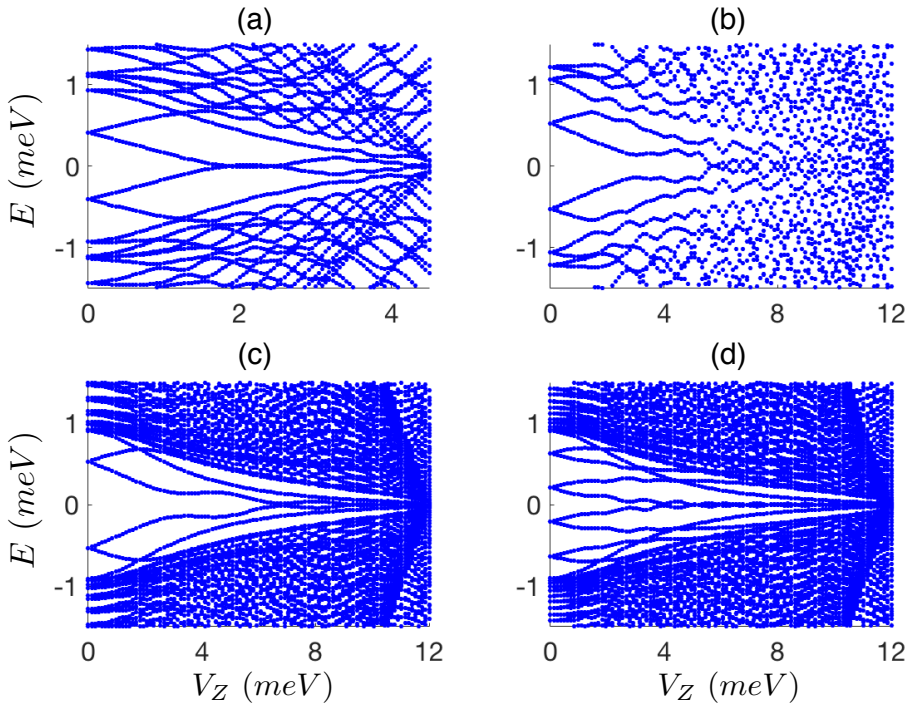

Figure 3.4: Energy spectra for hybrid structures with various parameters. (a): $\mu =$ 4.5 meV, nanowire length $L = 1.0$ μm, dot length $l = 0.3$ μm. (b): $\mu = 12.0$ meV, $L = 1.0$ μm, $l = 0.3$ μm. (c): $\mu = 12.0$ meV, $L = 4.0$ μm, $l = 0.3$ μm. (d): $\mu = 12.0$ meV, $L = 4.0$ μm, $l = 1.0$ μm.

3.3.1 Energy spectra for hybrid structures with various parameters

We show the energy spectra for various hybrid structures in Fig. 3.4. The few relevant parameters we focus on and thus vary between panels are chemical potential μ, length of the nanowire L, length of the quantum dot l, while all other parameters, e.g. pairing potential $\Delta_0 = 0.9$ meV and etc., are kept the same as the default values introduced in the previous sections. Fig. 3.4(a) shows the energy spectrum of a typical hybrid structure discussed in the previous sections, with the parameters conforming to the known values in the realistic experimental setup. There is a finite range of Zeeman splitting over which the energy of the topologically trivial

ABSs stick around zero. Through Fig. 3.4(b) to (d), we step by step increase the chemical potential μ, the length of the semiconductor-superconductor nanowire L, and the length of the quantum dot l. Finally with all the three parameters μ, L, l large in Fig. 3.4(d), the energy of the trivial ABS is even closer to zero energy, and even more strikingly, the range of Zeeman splitting for such near-zero-energy ABSs becomes extremely large, starting from a few times the pairing potential up to the chemical potential. The trend of decreasing ABS energy and increasing range of zero-energy sticking shown by Fig. 3.4(a) to (d) indicates that Fig. 3.4(a) and Fig. 3.4(d) are essentially adiabatically connected. In the following subsection, we will discuss why there exist such near-zero-energy ABSs over such a large range of Zeeman field in large μ, L, l limit using reflection matrix theory. Since realistic situation is adiabatically connected to this large μ, L, l limit, our understanding will also apply to most of the hybrid structures discussed in previous sections. Note that this discussion also explains why the zero-sticking of ABSs mostly arises in the large chemical potential regime.

3.3.2 Understanding zero-energy sticking from reflection matrix theory

In the previous subsection, numerical simulations show strong evidence that the energy of the ABSs approaches zero energy and the range of such near-zero-energy sticking increases with increasing chemical potential, increasing nanowire length, and increasing quantum dot length. Thus, here we try to understand this

phenomenon using reflection matrix theory. The setup is shown in Fig. 3.5, which is almost identical to that shown in Fig. 3.1. An imaginary piece of semiconductor is added between the quantum dot and the semiconductor-superconductor nanowire for the discussion of the reflection matrix theory. This imaginary semiconductor can also be regarded as a part of the quantum dot but with nearly homogeneous potential. For the propagating incoming mode in the normal lead, the total reflection matrix from the dot-nanowire structure is

$$\begin{aligned} r &= r_b + t' \left(r_{SC} + r_{SC} r_{QD} r_{SC} + ... \right) t \\ &= r_b + t' \left(1 - r_{SC} r_{QD} \right)^{-1} r_{SC} t, \end{aligned} \tag{3.3}$$

where r_b is the reflection matrix for the incoming modes in the lead reflected by the barrier, t is the transmission matrix for the lead modes transmitting to the semiconductor, r_{SC} is the reflection matrix for the semiconductor modes reflected by the proximitized nanowire, r_{QD} is the reflection matrix for the semiconductor modes reflected by the quantum dot, and t' is the is the transmission matrix for the semiconductor modes transmitted to the lead. The near-zero-energy differential conductance is

$$G = \frac{e^2}{h} Tr \left(\hat{1} - r_{ee}^{\dagger} r_{ee} + r_{he}^{\dagger} r_{he} \right) = \frac{2e^2}{h} Tr \left(r_{he}^{\dagger} r_{he} \right), \tag{3.4}$$

where r_{he} is the Andreev reflection matrix from the hybrid structure. The last step holds due to the unitarity of the total reflection matrix when bias voltage is

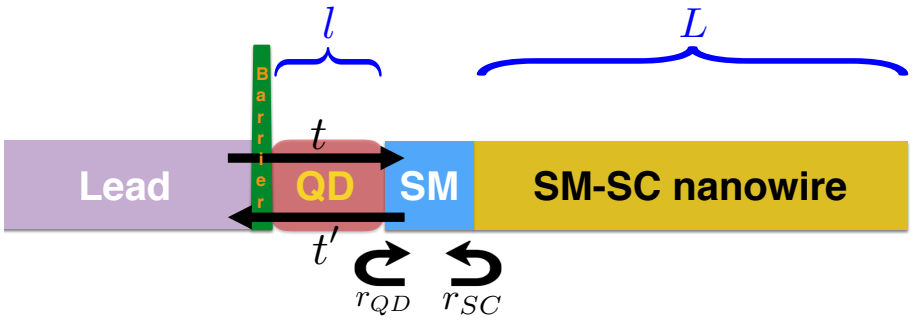

Figure 3.5: A schematic for the NS junction setup for the discussion of reflection matrix theory.

below the superconducting gap. The Andreev reflection is contained in the second term of Eq. (3.3), and the pole of $(1 - r_{SC}r_{QD})^{-1}$ corresponds to the peak of the differential conductance. On the other hand, the pole of the reflection matrix is also the condition for the formation of a bound state, i.e., a bound state forms when

$$Det\,(1 - r_{SC}r_{QD}) = 0 \tag{3.5}$$

is satisfied.

In the large Zeeman field limit, i.e., $V_Z \gg \Delta, \alpha_R$, the spin-orbit-coupled nanowire can be thought of as two spin-polarized bands with a large difference in chemical potential and Fermi momenta. When considering the scattering process between the effectively spin-polarized semiconductor and the semi-infinite superconductor, the momentum must be conserved in the limit of Andreev approximation $\Delta \ll \mu$. The constraint of momentum conservation prohibits the normal reflection between either the same or the other spinful channel due to the large difference in Fermi momenta between two channels. Thus the scattering process between semi-

conductor and the superconductor can be thought of as effectively two independent perfect Andreev reflection processes among each spin-polarized channel. So the reflection matrix for each channel can be written as

$$r_{SC} = \begin{pmatrix} 0 & e^{i\alpha} \\ e^{-i\alpha} & 0 \end{pmatrix}. \tag{3.6}$$

For the scattering process between the semiconductor and the quantum dot, when the dot potential is smooth, the normal reflection only connects the Fermi level within the same spinful channel, and thus again the two spin-polarized bands of the semiconductor can be thought of as independent of each other. So the reflection matrix for each band can be written as

$$r_{QD} = \begin{pmatrix} e^{i\beta} & 0 \\ 0 & e^{-i\beta} \end{pmatrix}. \tag{3.7}$$

The numerical evidence for the form of r_{SC} and r_{QD} are shown in Fig. 3.6, which is consistent with our argument in the large Zeeman field and Andreev approximation limit. It is easy to see that such zero-bias reflection matrices satisfy the condition for the formation of a bound state, i.e., Eq. (3.5). It indicates that in the large Zeeman field and Andreev approximation limit, the semiconductor-superconductor nanowire can be seen as consisting of two nearly spin-polarized p-wave superconductors, and each of them holds a MBS at the wire end. Since the interchannel coupling between the two p-wave superconductors is weak in the presence of a smooth dot potential

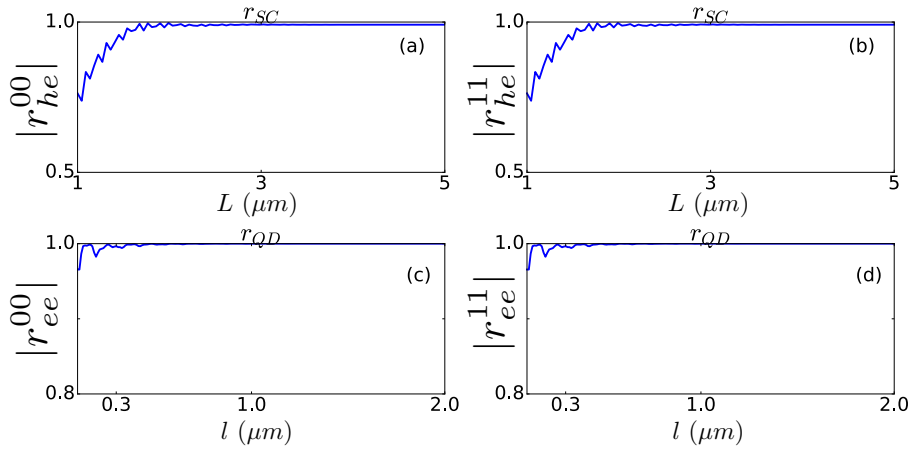

Figure 3.6: Matrix elements for the reflection matrices from the semiconductor-superconductor nanowire and the quantum dot, with chemical potential $\mu = 12$ meV, $V_Z = 8$ meV. The upper panels are the Andreev reflection between each spinful channel with in index 0 and 1 [i.e., the $|e^{i\alpha}|$ in Eq. (3.6)] as a function of nanowire length. In the long nanowire limit, the Andreev reflection becomes perfect. The lower panels are the normal reflection between each spinful channel [i.e., the $|e^{i\beta}|$ in Eq. (3.7)] as a function of dot length.

at the wire end, the two MBSs from two channels do not gap out each other, they form a near-zero-energy ABS.

Although the above discussion assumes large chemical potential, long semiconductor-superconductor nanowire, and long quantum dot, the conclusion well applies to the realistic situation with intermediate value of chemical potential, finite length of the nanowire and quantum dot, since these two situations are adiabatically connected with each other. This conclusion is explicitly verified by the extensive numerical results presented in this work.

3.4 Quantum dots as short-range inhomogeneity

So far in this chapter, our theoretical analysis has focused on quantum dots explicitly created at the end of a nanowire (see Fig. 3.1). In this case the quantum dot is normal (i.e., non-SC), while the rest of the wire is proximity-coupled to the parent SC. However, in general the quantum dot could be unintentional, i.e., the experimentalist may be unaware of its presence near the wire end, and it could be partially or completely covered by the SC. For example, such a situation may arise if a potential well with a depth of a few meV forms near the end of the proximitized segment of the wire. Similar phenomenology emerges in the presence of a low (but wide enough) potential barrier. After all, there is no easy way to rule out shallow potential wells (and low potential barriers) inside the nanowire or near its ends. In this context, we emphasize that a better understanding of the profile of the effective potential along the wire represents a critical outstanding problem. It turns out that all our results obtained so far still apply qualitatively even if the quantum dot is partially or completely inside the nanowire. In these cases we obtain exactly the same type of low-energy ABSs that have a tendency of sticking together near zero energy, thus producing ZBCPs that mimic MBS-induced ZBCPs. We present these results in detail below. We are providing these results here in order to go all the way from an isolated non-SC dot at the wire end (as in the previous sections of this paper) to a situation where the dot is inside the wire and is completely superconducting. We explicitly establish that the main results of the previous sections can be obtained everywhere within this range, i.e. from isolated

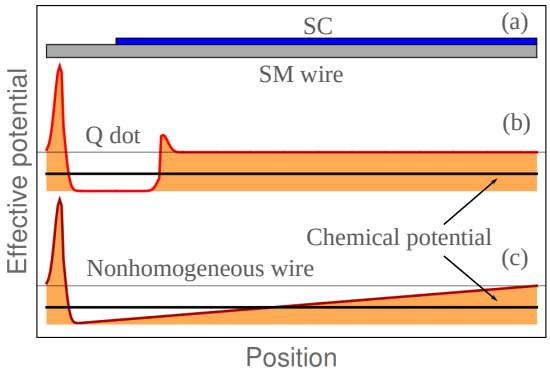

Figure 3.7: (a) Schematic representation of hybrid structure. (b) Effective potential as a function of position for a wire with a quantum dot near its left end. In the calculations the length of the quantum dot region is 250 nm, while the rest of the wire is 1 μm long. Note that the length parent superconductor (SC) can be varied, so that the quantum dot region can be uncovered, partially covered, or completely covered by the SC. (c) Smooth non-homogeneous effective potential. The peak at the left end of the wire represents the tunnel barrier.

dots to dots completely inside the nanowire. In fact, this behavior is rather generic in non-homogeneous semiconductor nanowires [87]. Finally, in this section we pay special attention to the profile of the ZBCPs associated with the almost-zero-energy ABSs. The key question that we want to address is whether or not a quantized ZBCP (i.e., a ZBCP with a peak height of $2e^2/h$) can be used as a hallmark for the MBSs expected to emerge beyond a certain critical field.

In Fig. 3.7, we represent schematically the hybrid structure [panel (a)] and the effective potential [panel (b)] corresponding to three different situations that we consider explicitly in this section using exactly the same model parameters: dot entirely outside the proximitized segment of the nanowire, dot completely inside the nanowire (i.e., the whole dot is superconducting), and dot partially covered by the parent superconductor. The depth of the potential well in the quantum dot region is about 1 meV and its length is 250 nm. The coupling between the quantum dot

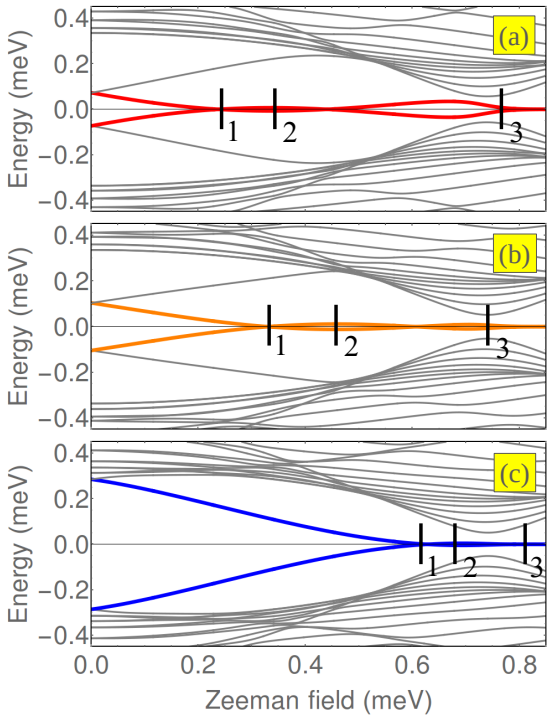

Figure 3.8: Dependence of the low-energy spectrum on the applied Zeeman field for a nanowire with a quantum dot near the left end (see Fig. 3.7). (a) Quantum dot outside the superconducting region. (b) Quantum dot half-covered by the parent superconductor. (c) Completely covered quantum dot. The induced gap is $\Delta_{ind} = 0.25$ meV and the chemical potential $\mu = -2.83\Delta_{ind}$, which corresponds to a critical Zeeman field of about 0.75 meV. The zero-temperature conductance along various constant field cuts marked "1", "2", and "3" are shown in Fig. 3.9.

and the rest of the wire is controlled by the height of the corresponding potential barrier [see panel (b) in Fig. 3.7]. In addition, the coupling depends on how much of the dot is covered by the superconductor. The parameters used in our calculations correspond to intermediate and strong coupling regimes. We note that replacing the potential well from Fig. 3.7 (b) with potential barrier of a height several times larger than the induced gap Δ_{ind} leads to low-energy features similar to those described below for the potential well. Finally, for comparison we also consider a nanowire with a smoothly varying non-homogeneous potential [panel (c) in Fig. 3.7].

In Fig. 3.8 we show the calculated low lying energy spectra for three cases: (a) normal dot (i.e. uncovered by the SC), (b) half-covered dot, and (c) fully-covered dot. The system is characterized by an induced gap $\Delta_{ind} = 0.25$ meV and a chemical potential $\mu = -2.83\Delta_{ind}$. The corresponding critical field associated with the topological quantum phase transition, $V_{Zc} \approx 3\Delta_{ind} = 0.75$ meV, is signaled by a minimum of the quasiparticle gap, as expected in a finite length system. First, we note that all three situations illustrated in Fig. 3.8 clearly show trivial almost-zero-energy ABSs in a certain range of Zeeman field (lower than the critical field). However, the Zeeman field V_Z^* associated with the first zero-energy crossing is significantly lower in the case of an uncovered dot [panel (a)] as compared to the partially-covered dot [panel (b)] and especially the fully covered dot [panel (c)]. Consequently, the range of Zeeman field corresponding to almost-zero-energy ABSs gets reduced with increasing the coverage of the quantum dot by the SC. Another key feature is the dependence of the energy of the ABS at $V_Z = 0$ on the dot coverage. For the fully covered dot [panel (c)], this energy is practically Δ_{ind}. In fact, by proximity effect, all the states that "reside" entirely under the parent SC have energies (at $V_Z = 0$) equal or larger than the induced gap for the corresponding band. By contrast, the zero-field energy of the ABSs in the half-covered [panel (b)] and uncovered [panel (a)] dots is significantly lower that induced gap. To obtain such a state it is required that a significant fraction of the corresponding wave function be localized outside the proximitized segment of the wire. We find that, quite generically, strongly coupled dots that are uncovered or partially covered (when the uncovered fraction is significant) can support ABSs that i) have energies

at $V_Z = 0$ much smaller than the induced gap and ii) are characterized by "merging fields" V_Z^* significantly lower than the critical value V_{Zc}. Consequently, in hybrid systems having strongly coupled dots at the end it is rather straightforward to obtain low-energy ABSs that merge toward zero and generate MBS-like ZBCPs in the topologically trivial regime, way before the TQPT. In a real system it is possible that superconductivity be suppressed by the magnetic field before reaching the critical value V_{Zc}. In such a scenario, a robust ZBCP that sticks to zero energy over a significant field range is entirely caused by (topologically trivial) merging ABSs, rather than (non-Abelian) MBSs.

Next, we address the following question: can one discriminate between a MBS-induced ZBCP and a trivial, ABS-induced ZBCP based on the height of the peak at zero temperature? More specifically, does the observation of a quantized peak guarantee its MBS nature? In short, the answer is no. However, observing a quantized ZBCP that is robust against small variations of parameters such as the Zeeman field, the chemical potential, and external gate potentials provides strong indication that the peak is probably not generated by merging ABSs partially localized outside the proximitized segment of the wire, i.e. scenarios (a) and (b) in Fig. 3.8. The results that support this conclusion are shown in Fig. 3.9. Each panel in Fig. 3.9 shows the (low-energy) differential conductance at $T = 0$ for three different values of the Zeeman field marked "1", "2", and "3" in the corresponding panel of Fig. 3.8. Generally, the largest value of the ZBCP obtains for Zeeman fields corresponding to the first zero-energy crossing, V_Z^*, marked "1" in Fig. 3.8. In this case, the maximum height exceeds $2e^2/h$. However, for the fully covered dot (bottom panel) the excess

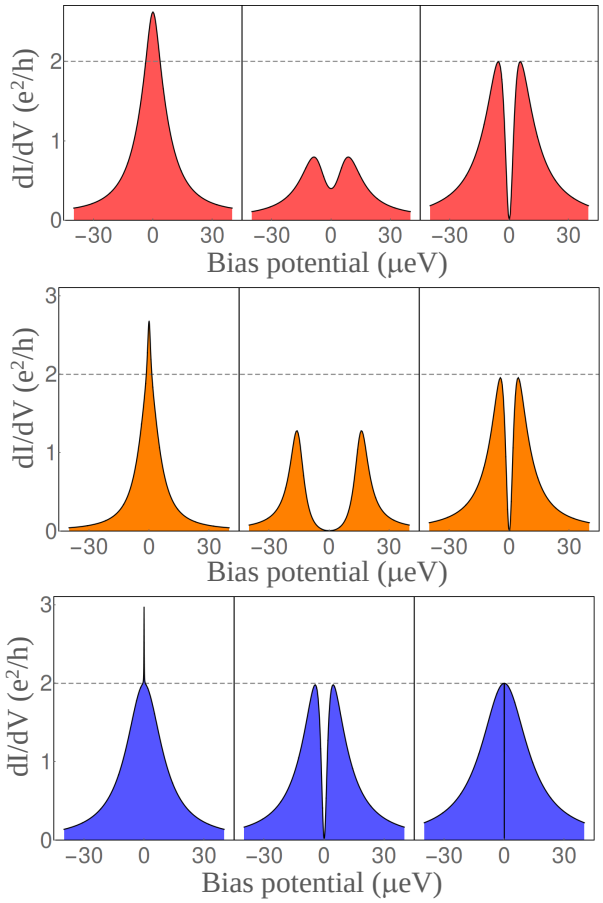

Figure 3.9: Differential conductance as function of the bias voltage for a quantum dot not covered by the superconductor (top panel), a half-covered dot (middle panel), and a fully-covered quantum dot (bottom panel). Each panel shows low-energy conductance peaks for three different values of the Zeeman field marked "1", "2", and "3" in the corresponding panel of Fig. 3.8.

conductance consists of a very narrow secondary peak that would be practically unobservable at finite temperature. In fact, we find that in the case of a fully covered dot, at low-temperature, the conductance peak height is practically quantized in both the trivial regime (field cuts "1" and "2") and the topological regime (field cut "3"), regardless of whether the ZBCP is split or not. By contrast, for the uncovered and the half-covered dots (top and middle panels, respectively) the peak height can have any value between 0 and $4e^2/h$ in the trivial regime and becomes quantized

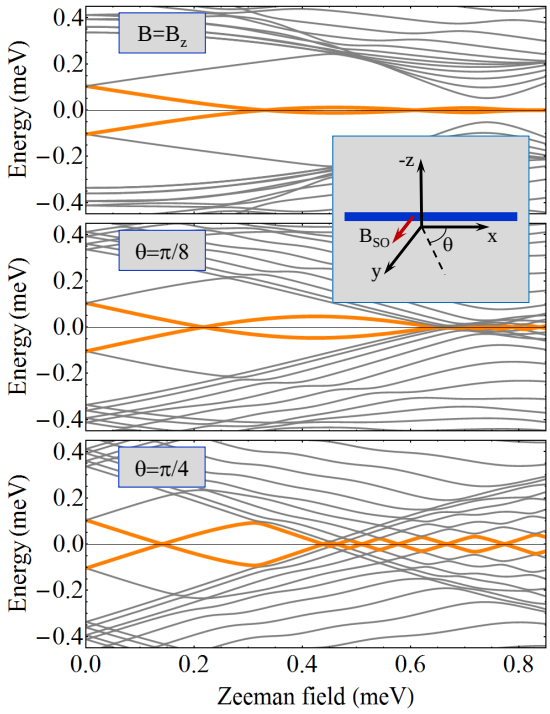

Figure 3.10: Dependence of the low-energy spectrum from Fig. 3.8 (b) on the orientation of the applied magnetic field. *Top*: Magnetic field oriented along the z axis (i.e. perpendicular to the wire and the effective SO field, see inset). The spectrum is identical to panel (b) from Fig. 3.8. *Middle and bottom*: Rotating the field in the x-y plane destroys the property of the ABSs to coalesce into stable nearly zero energy modes. In addition, the spectrum becomes gapless above a certain (angle-dependent) value of the Zeeman splitting.

in topological regime. Of course, a quantized ZBCP can be obtained even in the trivial regime at certain specific values of the Zeeman field, but its quantization is not robust against small variations of the control parameters (e.g., Zeeman splitting, chemical potential, SC gap).

A key requirement for the realization of topological superconductivity and MBSs in semiconductor-superconductor hybrid structures is that the applied magnetic field be perpendicular to the effective Rashba spin-orbit(SO) field. More specifically, the MBSs are robust against rotations of the applied field in the plane per-

pendicular to the SO field, but become unstable as the angle between the applied and the SO fields (which corresponds to $\pi/2-\theta$ in the inset of Fig. 3.10) is reduced. The natural question is whether the nearly-zero ABS modes induced by a quantum dot (or other type of inhomogeneity) show a similar behavior. We find that the coalescing ABSs (and, more generally, the low-energy spectrum) are insensitive to rotations of the applied field in the plane perpendicular to the effective SO field (i.e. the x-z plane in Fig. 3.10). This property is illustrated by the spectrum shown in the top panel of Fig. 3.10 corresponding to a field oriented along the z-axis. Note that this spectrum is identical to Fig. 3.8 (b), which corresponds to a field oriented along the x-axis. By contrast, when the field is rotated in the x-y plane, the nearly-zero ABS mode becomes unstable (see the middle and bottom panels in 3.10). In addition, the spectrum becomes gapless above a certain (angle-dependent) value of the Zeeman splitting. We conclude that the coalescing ABSs behave qualitatively similar to the MBSs with respect to rotations of the field orientation. To further support this conclusion, we calculate the low-energy spectra of the wire-dot system in the Majorana regime for two different orientations of the applied magnetic field. The results are shown in Fig. 3.11. We note that rotating the field in the x-z plane (i.e. the plane perpendicular to the SO field) does not affect the spectrum. By contrast, rotating the field in the x-y plane changes the low-energy features in a manner similar to that discussed in the context of coalescing ABSs.

Before concluding this section, we compare a hybrid system having a (strongly coupled) quantum dot near one end with an inhomogeneous system with a smooth effective potential as shown in Fig. 3.7 (c). In the language of Ref. [87], this would

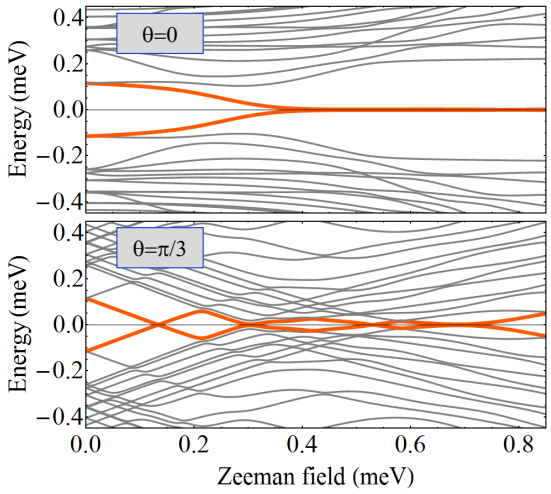

Figure 3.11: Dependence of the low-energy spectrum on the field orientation for a wire-dot system in the Majorana regime. The model parameters are the same as in Fig. 3.8 (b), except the chemical potential, which is set to $\mu = -0.25\Delta_{ind}$. The top panel corresponds to a field oriented along the wire (or any other direction in the x-z plane), while the bottom panel corresponds to an angle $\theta = \pi/3$ in the x-y plane (see inset of Fig. 3.10). Note the similarity with the bottom panel from Fig. 3.10.

correspond to a long-range inhomogeneity, in contrast to the quantum dots which can be viewed as short-range inhomogeneities. The low-energy spectrum of the non-homogeneous system is shown in Fig. 3.12. At zero field, the energy of the ABS is lower than the induced gap as a result of the nanowire being only partially covered (about 90%) by the parent superconductor, as discussed above. Note the striking absence of a minimum of the quasiparticle gap, which would signal the TQPT in a homogeneous system. The merging ABSs form a very robust nearly-zero mode, which, according the analysis in Ref. [87], consists of partially overlapping MBSs. The low-energy differential conductance corresponding to the nearly-zero mode in Fig. 3.12 is shown in Fig. 3.13 (as function of the Zeeman field for three different values of the bias voltage) and Fig. 3.14 (as function of the bias voltage for three different Zeeman fields marked "1", "2", and "3" in Fig. 3.12). The

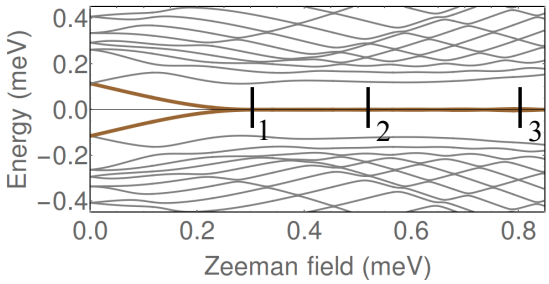

Figure 3.12: Low-energy spectrum as function of the applied Zeeman field for a system with smooth non-homogeneous effective potential [see Fig. 3.7, panel (c)]. The length of the parent SC is the same as in the case of half-covered quantum dot (i.e. a segment of the wire of about 125 nm is not covered). Note the robust (nearly) zero-mode and the absence of a well defined minimum of the quasiparticle gap corresponding to the crossover between the trivial and the "topological" regimes.

low-bias differential conductance traces shown in Fig. 3.13 have values between 0 and (almost) $4e^2/h$. In particular, the differential conductance exceeds $2e^2/h$ in the vicinity of the first zero-energy crossing, $V_Z \approx 0.3$ meV (see Fig. 3.12). However, in practice it would be extremely difficult to observe a ZBCP larger than $2e^2/h$ at finite temperature. This is due to the fact that the contribution exceeding the quantized value forms a very narrow secondary peak (see Fig. 3.14, left panel), similar to the completely covered dot shown in Fig. 3.9. We interpret the double-peak structure of the ZBCP as resulting from the partially-overlapping MBSs that form the ABS. The broad peak is generated by the MBS localized closer to the wire end (which is strongly coupled to the metallic lead), while the narrow additional peak is due to the MBS localized further away from the end (which is weakly coupled to the lead). Finally, we note that the low conductance values in Fig. 3.13 are due to the splitting of the ZBCP. However, the maximum value of the ZBCP is practically quantized at very low (but finite) temperature, as evident from the results shown in Fig. 3.14.

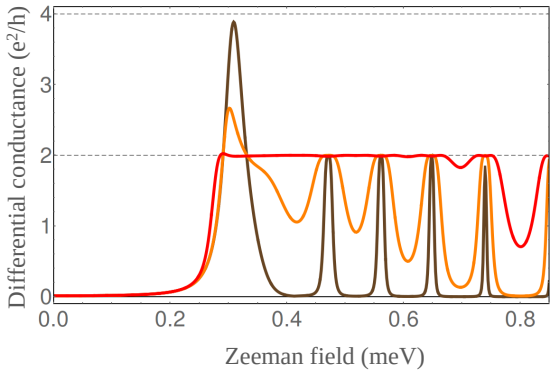

Figure 3.13: Dependence of the low-energy differential conductance on the Zeeman splitting for the non-homogeneous wire with the spectrum shown in Fig. 3.12. The black, orange, and red lines correspond to a bias voltage $V_{bias} = 0.05, 0.15$, and 0.75 μV, respectively.

In summary, the results presented in this section lead us to the following conclusions. First, semiconductor-superconductor hybrid systems having strongly-coupled quantum dots at the end of the wire, which can be viewed as systems with short-range potential inhomogeneities, generate ABSs that, quite generically, tend to merge at zero energy with increasing Zeeman field, but still within the topologically-trivial regime. Second, ABSs with energies at $V_Z = 0$ significantly lower than the induced gap and low values of the merging field V_Z^* are likely to generate extremely robust topologically-trivial ZBCPs. Third, measuring a quantized (to $2e^2/h$) ZBCP does not provide definitive evidence for MBSs (although finding ZBCP quantization which is robust over variations in many parameters, e.g., magnetic field, chemical potential, tunnel barrier, carrier density, would be very strong evidence for the existence of MBS). However, trivial conductance peaks generated by merging ABSs having wave functions partially localized outside the superconducting region are generally expected to produce ZBCPs with heights between 0 and $4e^2/h$. In this

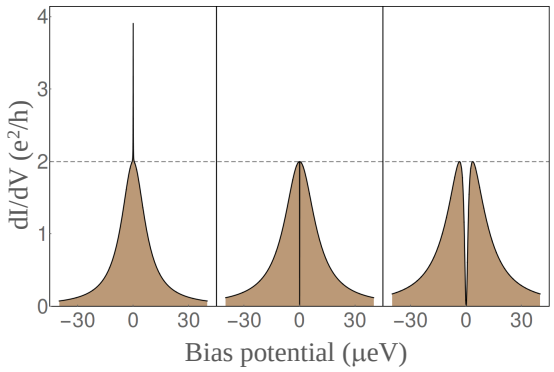

Figure 3.14: Zero temperature differential conductance as function of the bias voltage for three different values of the Zeeman field marked "1", "2", and "3" in Fig. 3.12.

regime, an accidental quantized peak will not be robust against small variations of the control parameters. By contrast, if the wave function is entirely inside the proximitized region, the ZBCP is (practically) quantized and cannot be distinguished from a MBS-induced conductance peak by a local tunneling measurement. In this case, a minimal requirement for the Majorana scenario is to be able to reproduce the (robust) ZBCP by performing a tunneling measurement at the opposite end of the wire, in the spirit of Ref. [53]. Finally, our fourth conclusion is that very similar phenomenologies can be generated using rather different effective potentials (i.e., the effective "quantum dot" leading to the ABS could arise from many different physical origins and could lie inside or outside the nanowire). A better understanding of the profile of the effective potential along the wire (which can be obtained, for example, by performing detailed Schrodinger-Poisson calculations) represents a critical task in this field.

3.5 Conclusion

Our conclusion is that in strongly-coupled dot-nanowire hybrid structures (and in the presence of superconductivity, Zeeman splitting, and spin-orbit coupling) ABSs generically coalesce around zero energy producing zero-bias tunneling conductance values that mimic Majorana properties, although the physics is non-topological. In fact, the transport properties of such "accidental" almost zero-energy trivial ABSs in class D systems are (locally) difficult to distinguish from the conductance behavior of topological MBSs. We show that this zero-energy-sticking behavior of trivial ABSs (superficially mimicking topological Majorana behavior) persists all the way from an isolated (i.e. non-SC) quantum dot at the end of the nanowire to a quantum dot completely immersed inside the nanowire (i.e. superconducting) as long as finite Zeeman splitting and spin-orbit coupling are present. Our theory thus connects the recent observations of Deng *et al.* [31] to the earlier observations of Lee *et al.* [88], who studied ABSs in a SC dot (not attached to a long nanowire), establishing that the physics in these two situations interpolates smoothly. In both theses cases ZBCPs may arise from trivial ABSs in the presence of superconductivity, spin-orbit coupling, and Zeeman splitting. Of course, in a small quantum dot, the concept of MBSs does not apply because of strong overlap between the two ends whereas in the Deng *et al.* experiment (i.e. in a dot-nanowire hybrid system) the ZBCP may arise from either trivial ABS or topological MBS. We establish, however, that in both cases the ABS can be thought of as overlapping MBSs, and hence the generic zero-sticking property of the ABS arises from the

combination of spin-orbit coupling, spin splitting, and superconductivity. An immediate (and distressing) conclusion of our work is that the observation of a ZBCP (even if the conductance value is close to the expected $2e^2/h$ quantization) cannot by itself be construed as evidence supporting the existence of topological MBSs. In particular, both trivial ABSs and topological MBSs may give rise to zero-bias peaks, and there is no simple way of distinguishing them just by looking at the tunneling spectra. Since the possibility that a given experimental nanowire may contain inside it some kind of accidental quantum dot can never be ruled out, the tunneling conductance exhibiting zero-bias peaks in any nanowire may simply be the result of the existence of almost-zero-energy ABSs in the system. Our work shows this generic trivial situation to be a compelling scenario, bringing into question whether any of the observed ZBCPs in various experiments by themselves can be taken as strong evidence in favor of the existence of MBSs since the possibility that these ZBCPs arising from accidental trivial ABSs cannot a priori be ruled out. Consequently, a ZBCP obtained by tunneling from one end of the wire cannot be accepted as a compelling topological Majorana signature (even when the height of the peak is quantized at $2e^2/h$), since a likely alternative scenario is that the zero-bias peak is, in fact, a signature of a trivial ABS associated with a strongly coupled quantum dot or other type of inhomogeneity (unintentionally) present in the system. One must carry out careful additional consistency checks on the observed ZBCPs in order to carefully distinguish between ABS and MBS.

Chapter 4

Differentiation between Majorana and Andreev bound states

As discussed extensively in Chapter 3, trivial ABSs arising from chemical potential variations could lead to ZBCPs at finite magnetic field in class D nanowires, precisely mimicking the predicted ZBCPs arising from the topological MBSs. This finding raises a serious question on the efficacy of using ZBCPs, by themselves, as evidence supporting the existence of topological MBSs in nanowires. In this chapter, we provide specific experimental protocols for tunneling spectroscopy measurements to distinguish between ABS and MBS without invoking more demanding nonlocal measurements which have not yet been successfully performed in nanowire systems. In particular, we discuss three distinct experimental schemes involving response of the ZBCP to local perturbations of the tunnel barrier, overlap of bound states from the wire ends, and most compellingly, introducing a sharp localized potential in the wire itself to perturb the ZBCPs.

Clearly, the definitive distinction between topological MBS and trivial ABS must await a nonlocal measurement involving braiding and interferometry. Here, we have a less ambitious goal. We explore experimental avenues within the tunneling spectroscopy measurements in order to provide plausible distinctive features between

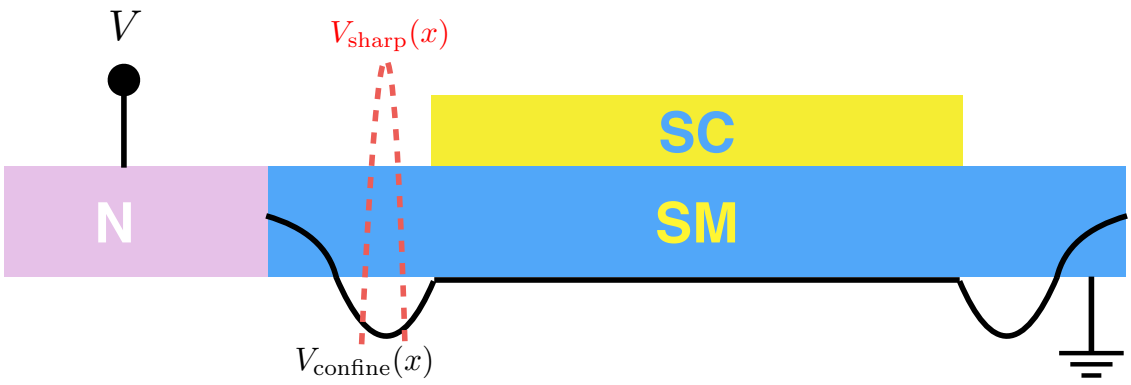

Figure 4.1: A schematic of the NS junction considered in this chapter. In Sec. 4.1, we test the stability of ZBCPs by varying the amplitude of the confinement potential. In Sec. 4.2, we also consider the interplay of a pair of confinement potential-induced ABSs located at both wire ends. The proposal of taking advantage of a sharp potential (red curve) to distinguish MBS and ABS is discussed in Sec. 4.4

ABS- and MBS-induced ZBCPs. Although such local transport measurements are unlikely to be absolutely definitive in distinguishing between ABS and MBS, they have the considerable advantage of being doable right away, thus, if successful, providing substantial boost to the MBS interpretation of ZBCP. In fact, some such transport-based proposed distinctions between ABS and MBS have already been discussed in the literature [89, 90, 91]. For example, the robustness of ZBCP strength (i.e., the conductance value at zero-bias voltage and its precise quantization) and location (i.e. precise zero voltage) with varying magnetic field and tunnel barrier strength is an indicator for MBS [36, 89], and this aspect is studied in some depth in the current work because of its importance and experimental feasibility.

We describe through extensive numerical simulations of the tunneling conductance three different physical scenarios in the context of using tunneling spectroscopy aimed at distinguishing between ABS and MBS. The first one, mentioned above, is

the sensitivity of the ZBCP to variations in the tunnel barrier potential. In general, the ZBCP arising from ABS (MBS) should be more (less) sensitive to the tunnel barrier, enabling a direct method of distinguishing ABS from MBS. The second topic is the interplay of two MBSs or ABSs localized at the two wire ends to see how the ZBCP is affected when two bound states overlap to some extent with the expectation that there are significant differences in the "overlap physics" between the two cases. The third topic, which is the most important new idea introduced in this work, is the sensitivity of the tunneling ZBCP to the introduction of a sharp local potential in the wire. The MBS should be insensitive to a sharp local potential since the MBS entanglement is topological and nonlocal whereas the ABS should be strongly affected by the sharp local perturbation, thus allowing for a clear distinction between ABS and MBS.

4.1 Variation of tunnel gate potential

4.1.1 Energy spectra for hybrid structures with ABS and MBS-induced zero modes

We first calculate the energy spectra for quantum dot-superconductor hybrid nanostructure, and the numerical results are in Fig. 4.2. Fig. 4.2(a) is the calculated spectrum as a function of chemical potential at fixed $V_Z = 2.0$ meV for $V_D = 4$ meV in Eq. (3.2) with topological MBS-(or trivial ABS-) induced zero modes at small (large) chemical potential regimes. Now, we ask how this spectrum evolves if we only vary V_D keeping everything else exactly the same. Fig. 4.2(b) presents the MBS

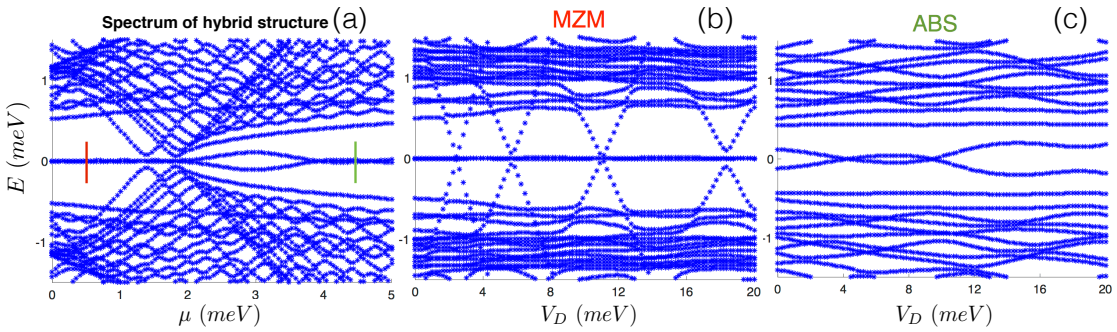

Figure 4.2: (a) Calculated energy spectrum of a hybrid structure as a function of chemical potential μ with fixed Zeeman splitting $V_Z = 2.0$ meV. Critical chemical potential is at $\mu_c \simeq 1.8$ meV with red (green) lines indicating topological (trivial) zero modes. (b) Fixed chemical potential in the topological regime $\mu = 0.5$ meV $< \mu_c$, to see how MBSs vary with the depth of the quantum dot. (c) Fixed chemical potential in the non-topological regime $\mu = 4.5$ meV $> \mu_c$, to see how near-zero-energy ABSs vary with the depth of the quantum dot.

spectrum (i.e., at small chemical potential) as a function of dot depth, showing that it is robust against change of dot depth. By contrast, Fig. 4.2(c) shows the ABS spectrum (i.e., large chemical potential) as a function of the dot potential depth, clearly showing that the ABS "zero mode" is not stable and oscillates (or splits) as a function of the dot potential. So varying the dot depth (e.g., by experimentally changing gate potential) will be a stability test distinguishing topological MBSs and non-topological ABSs. Note that it is possible (even likely) that the original ABS-induced ZBCP will split as the dot potential changes whereas a new trivial zero mode could appear, but the stability (or not) of specific ZBCPs to gate potentials could be a powerful experimental technique for distinguishing trivial and topological ZBCPs. Of course, experimentally tuning the dot potential by an external gate may turn out to be difficult in realistic situations, but modes which are unstable to variations in gate potentials are likely to be trivial ABS-induced ZBCPs.

4.1.2 Conductance for hybrid structures with ABS and MBS-induced zero modes

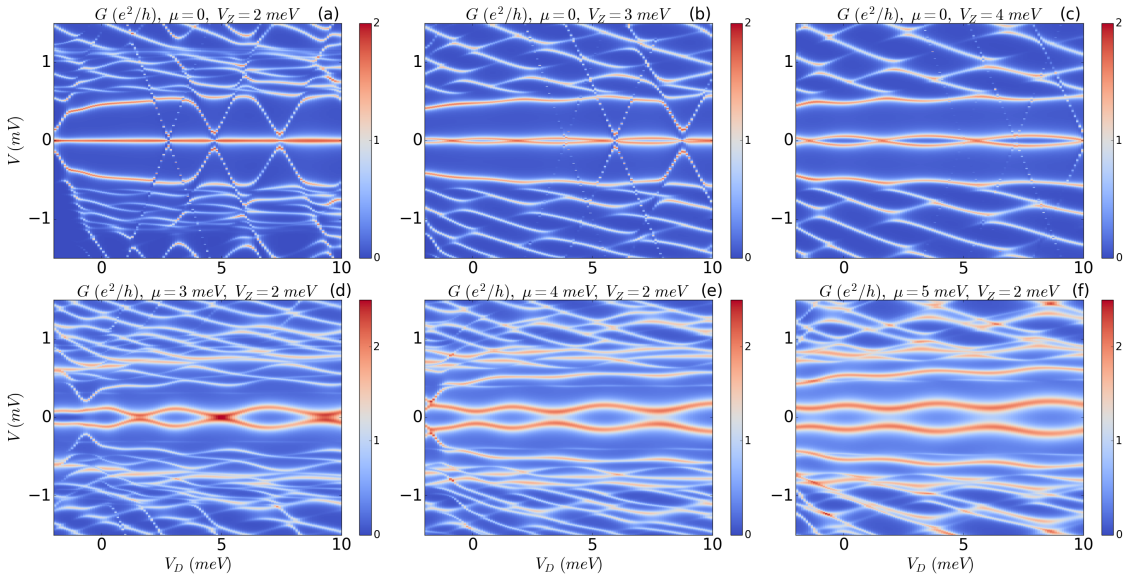

Figure 4.3: Differential conductance as a function of the dot depth for hybrid structures at various but fixed chemical potential and Zeeman field. (a)-(c) All the hybrid structures are in the topological regime, i.e., all the zero-bias or near-zero-bias conductance peaks are MBS-induced. (d)-(f), all the hybrid structures are topologically trivial, i.e., the zero-bias or near-zero-bias conductance peaks are ABS-induced.

We also show the calculated differential conductance through the hybrid structures as a function of the depth of the quantum dot and bias voltage, as shown in Fig. 4.3. The conductance color plots in the upper panels (a)-(c) are for topological nanowires, i.e., $V_Z > V_{Zc} = \sqrt{\mu^2 + \Delta^2}$, and thus all the zero-bias or near-zero-bias conductance peaks are MBS-induced. Such ZBCPs are stable against the variation of the depth of the quantum dot. With the increase of the Zeeman field, ZBCPs will be split and form Majorana oscillations as a function of the dot depth. By contrast, the conductance color plots in the lower panels (d)-(f) are for topologically trivial nanowires ($V_Z < \mu$), and thus all the near-zero-bias conductance peaks are ABS-

induced. These nontopological near-zero-bias peaks also show beating patterns as a function of the dot depth, which is quite similar to the patterns for Majorana oscillations, although the origin is nontopological. But the crucial difference between the two situations is that ABS-induced oscillations are not guaranteed to cross zero bias for a variation of the parameter choice, e.g., increasing chemical potential as shown in (e) and (f), while for MBS-induced oscillations, although the amplitude of oscillation will increase with parameters in the nanowire (e.g., Zeeman field), the oscillation itself is sure to pass through zero-bias voltage. The difference between the two situations rises from the crucial fact that ABS-induced ZBCPs are almost zero modes involving (always) some level repulsion whereas the MBS-induced ZBCP oscillations arise from the splitting of a true zero mode in the infinite wire limit.

4.2 Interplay between bound states from two ends

Now we study how the interaction between two MBSs or two ABSs would affect the differential conductance. We vary the degree of the overlap between two end states by comparing long and short wires, and the schematic is shown in Fig. 4.1. The numerical result is shown in Fig. 4.4. Figure 4.4(a) shows the differential conductance for an extremely long topological nanowire, where the two MBSs are faraway from each other and thus we can think of the wire effectively as containing a single MBS at the interface between the lead and the nanowire. Thus in the topological regime (large V_Z), a ZBCP forms exactly at zero-bias voltage. In Fig. 4.4(b), the length is shortened such that there is more overlap between the two

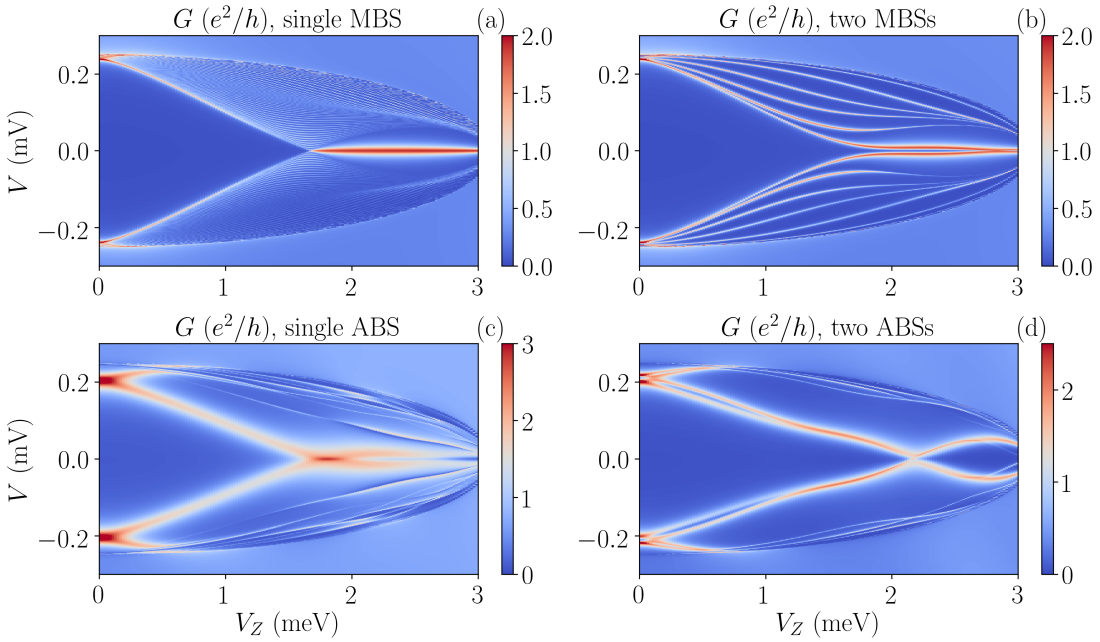

Figure 4.4: Differential conductance for nanowires with two MBSs or two ABSs. (a) long topological nanowire with $L = 3.0$ μm, $\mu = 0.7$ meV. (b) short topological nanowire with $L = 0.4$ μm, $\mu = 0.7$ meV. (c) long trivial nanowire with $L = 3.0$ μm, $\mu = 4.5$ meV. (d) short trivial nanowire with $L = 0.8$ μm, $\mu = 4.5$ meV. Note that in (c) and (d), there is a smooth confinement potential $V_D = 4.0$meV on both sides of the nanowire, while $V_D = 0$ for (a) and (b)

MBSs at wire ends, thus causing oscillations as a function of Zeeman splitting in the ZBCP at large Zeeman field regime. Figure 4.4(c) and (d) show the situation for the topologically trivial nanowires, for which there is a smooth confinement potential at each end of the nanowire so that two ABSs are formed inside the wire. Figure 4.4(c) shows the differential conductance for a long nanowire, which is quite similar to the single confinement potential case, i.e., a sticky ZBCP forms at large Zeeman field regime purely from nontopological mechanism. When the length is shortened, as in Fig. 4.4(d), the two ABSs strongly interact with each other and gap out each other, thus destroying the near ZBCP over a large range of the Zeeman field.

4.3 Interplay between bound states and external dot state

Another way to distinguish ABS and MBS is considered in Refs. [90, 91, 92] where an external dot state interacts with the fermionic state inside the nanowire. Reference [90, 91, 92] use the interaction between a quantum dot state and MBS or ABS at the same end to distinguish MBSs from ABSs. The basic idea is that since the ABS could be considered as a pair of MBSs at the same end, these two MBSs would be expected to have similar overlap with the quantum dot, which would be very different from the interaction with a single MBS at each end where only one MBS would strongly interact with the quantum dot. Therefore, in this sense the interaction of the quantum dot can be used to probe "non-locality" assuming that the tunneling matrix elements between the different MBSs involved are controlled by distance.

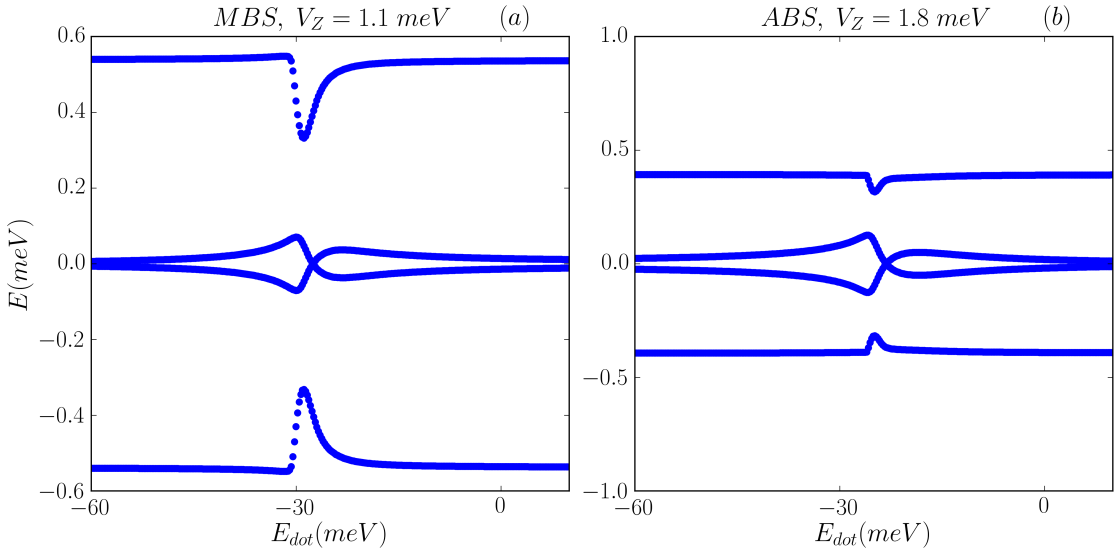

Figure 4.5: The anticrossing structures around zero energy are shown for (a) a MBS interacting with a dot induced state, and (b) an ABS interacting with a dot induced state. Note the identical qualitative nature of the zero energy anticrossing behaviors in the two cases, making it impossible to conclude whether an MBS or an ABS is involved in the anticrossing pattern. The parameters of the nanowire in (a) is $L = 0.4\mu$m, $\mu = 0.0$meV. For the nanowire in (b), $L = 1.3\mu$m, $\mu = 4.5$meV with the smooth potental being 0.3μm long.

Specifically the "non-locality" tested in these Refs. [90, 91, 92] is really the ratio of coupling of the two MBSs (that constitute the ABS or are at the ends of the wire) to the quantum dot. The ABSs considered in this work, arising from the smooth potential, are constituted by two MBSs which are produced by states at different Fermi momenta. Therefore these MBSs constituting the ABS, despite being spatially local relative to the quantum dot, have rather different couplings to the quantum dot or leads. For such ABSs the quantum dot would only couple to one of the MBSs producing the measurement proposed in Refs. [90, 91] and measured in recent experiments Ref. [92] leading to very similar results as expected from isolated MBSs. In Fig. 4.5 we show our numerical results for situations (1) where the external dot state interacts with a MBS [Fig. 4.5(a)] as considered in [90, 91], and (2) where the external dot state interacts with an accidental potential fluctuation-induced ABS [Fig. 4.5(b)]. The results of Fig. 4.5 show that the two situations give rise to essentially identical anticrossing patterns making it impossible to distinguish ABS from MBS in this case. Note that despite the fact that the two MBSs forming in the ABS here are at the same end of the wire as opposed to being at opposite ends, our results show that tunneling from one end cannot distinguish the two situations. This is because the tunneling matrix element generically couples one of these MBSs more strongly with the tunneling lead, thus effectively manifesting a single-MBS type tunneling current in spite of the bound state being a combination of two MBSs close together. We conclude therefore that the anticrossing behaviors of MBSs and ABSs with dot induced states can be similar, and thus no definitive conclusion can be drawn from such anticrossing patterns about the existence or not of MBSs.

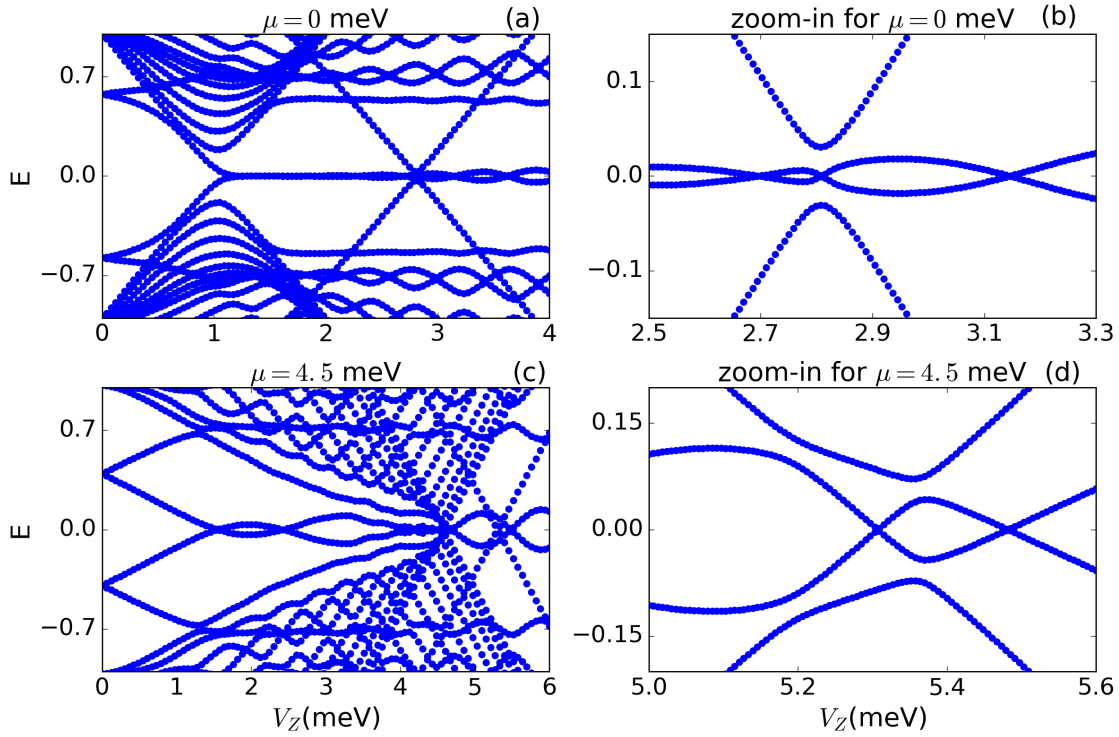

Figure 4.6: (a) Energy spectrum for a Majorana nanowire with $\mu = 0$ meV in the presence of a smooth confinement. The parameters for the nanowire is $L = 1.3\mu$m, $\Delta = 1.0$ meV, $V_D = 4.0$ meV, and $l_D = 0.3$ μm. Thus the nanowire enters the topological regime at $V_{Zc} \simeq 1.0$ meV hosting a pair of MBSs. (b) A zoom-in spectrum at Zeeman field where the bound state of the confinement potnetial interacts with the MBSs, showing the anti-crossing feature. (c) Energy spectrum for a Majorana nanowire with $\mu = 4.5$ meV in the presence of a smooth confinement. The other parameters are the same as (a) Thus the nanowire enters the topological regime at $V_{Zc} \simeq 4.6$ meV hosting a pair of MBSs. Note that in the nontopological regime, there are near-zero-energy ABSs because of the smooth confinement condition being satisfied. (d) A zoom-in spectrum at Zeeman field where the dot state interacts with the MBSs, showing the avoided-crossing feature.

In Fig. 4.6 , we show more details on our calculated interplay between MBS and ABS in an applied smooth potential. At zero chemical potential, there is no trivial ABS near zero energy in the presence of the smooth potential [Figs. 4.6(a) and (b)], and all we have is the approximate ZBCP associated with the MBS for $V_Z > V_{Zc}$. The smooth potential does, however, produce well-defined finite energy ABSs [which come close together anticrossing with each other at $V_Z \simeq 2.8$ meV $> V_{Zc} \simeq 1$ meV in Figs. 4.6(a) and (b)]. Near this ABS anticrossing, the MBS and ABS interact mildly, but nothing much happens at $\mu = 0$ except that both ABS and MBS are clearly visible in the spectra. The situation, however, changes substantially when we go to finite chemical potential [Figs. 4.6(c) and (d)] with $\mu = 4.5$ meV. Now near-zero-energy trivial ABSs exist in the nontopological $V_Z < V_{Zc} = 4.6$ meV regime, as can be seen for 1.5meV $< V_Z <$ 2.5meV and again for 4meV $< V_Z <$ 4.5 meV in Fig. 4.6(c). For $V_Z > V_{Zc}$, we see the usual ZBCP arising from the topological MBS (which manifests Majorana splitting oscillations in these results). The interesting region is 5.2meV $< V_Z <$ 5.5 meV [see Fig. 4.6(d)] in the topological regime, where there is a pair of finite-energy ABSs anticrossing at mid-gap. These ABSs also interact with the MBS, but the effect is rather small with a small distortion ("repulsion") of the ABS energy dispersion as a function of V_Z [$\simeq$ 5.4meV in Fig. 4.6(d)]. It is unclear if such small modifications in the ABS spectrum due to the interplay between ABS and MBS in the topological regime can be detected in experiments where there is invariable level broadening arising from temperature, disorder, and dissipation. The key problem in the experiments of course is that neither V_{Zc} nor μ is known, and hence the topological regime, which

is uniquely defined theoretically through V_{Zc}, is unknown experimentally and can only be inferred based on the observation of a near-zero-bias peak in the spectra. As one can see, in Fig. 4.6(c) and (d), a zero-bias peak could happen at $V_Z \simeq 1.5 - 2.5$ meV , 4 - 4.5 meV, and $>$ 4.6 meV – the first two zero modes are ABS whereas the last one is MBS which we know theoretically only because we know the precise location of $V_{Zc} \simeq 4.6$ meV.

4.4 Sharp potential

Our fourth proposal for differentiating between MBS and ABS-induced ZBCPs is to apply a sharp localized potential inside the smooth confinement potential (red dash line in Fig. **??**). To understand the effect of a sharp potential on the ABS, note that the pinning of ABSs to near zero energy relies on the ABS being composed of a pair of MBSs from states with different Fermi wavelengths [30]. Smooth confinement ensures that the MBSs couple to the lead with very different strengths leading to the MBS-like behavior of the ABS because one MBS (out of the pair forming the ABS) always couples more strongly to the tunneling lead. The introduction of a sharp potential should break the conservation of momentum that prevents the coupling of the pair of MBSs that constitute the ABS and lead to the ABS splitting away from zero energy. In contrast the sharp potential would have no impact on the single MBS in the topological nanowire because the coupling to the other Majorana, which is at the other end of the wire, should be exponentially suppressed by the length of the wire. To verify this expectation we consider topological and nontopological

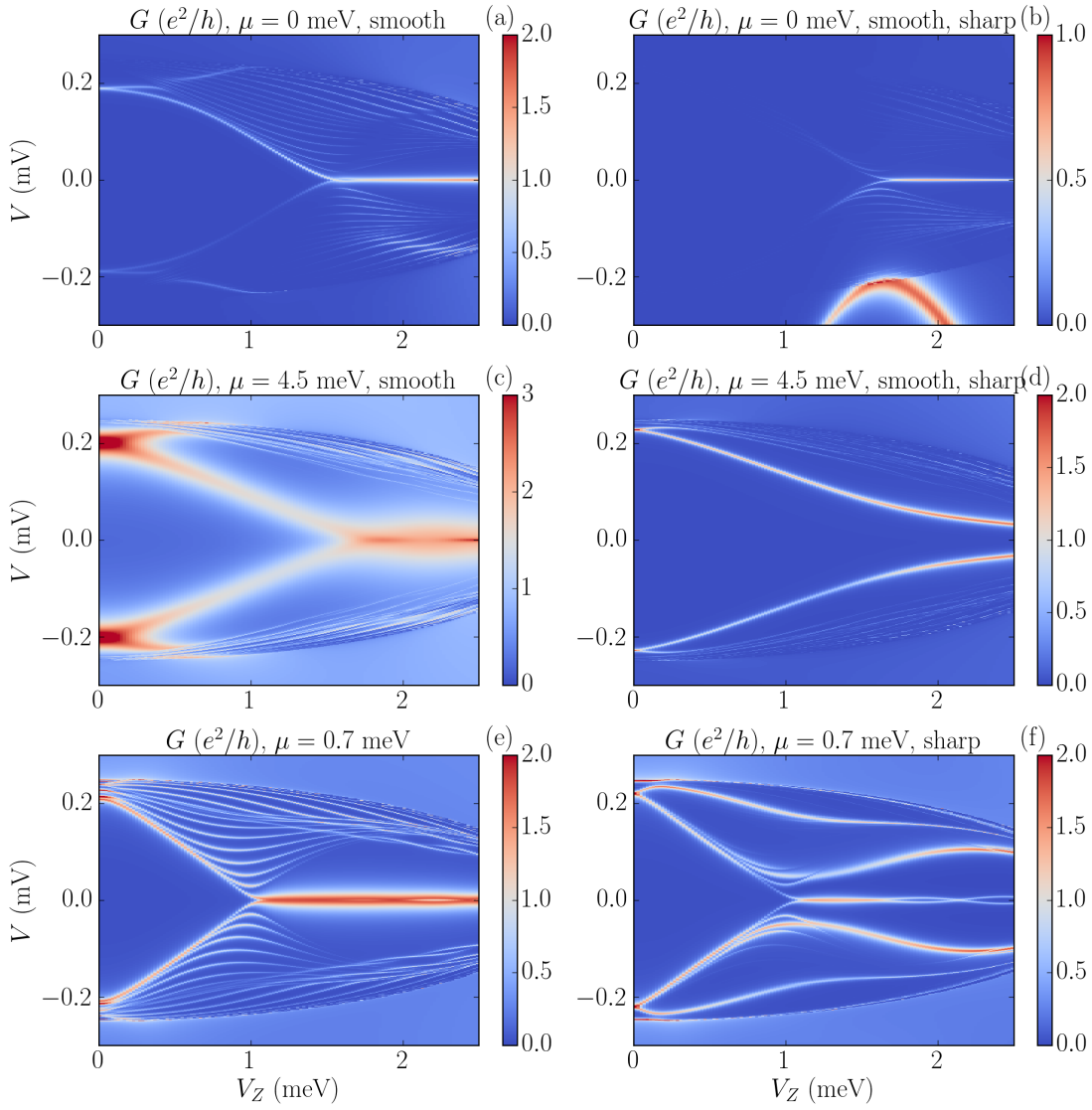

Figure 4.7: The differential conductance for nanowires without a sharp potential (left panels) and with the presence of a sharp potential (right panels). The sharp potential has height $V_s = 20$ meV, width $a = 25$ nm, and is located at $x_0 = 0.22$ μm. (a, b) There is a smooth confinement potential at the junction interface, and $\mu = 0$. A MBS-induced ZBCP forms at large Zeeman field. (c, d) There is a smooth confinement potential at the junction interface, and $\mu = 4.5$ meV. An ABS-induced ZBCP forms at large enough Zeeman field but the peak disappears when a sharp potential is present. (e, f) There is no confinement potential, and $\mu = 0.7$meV.

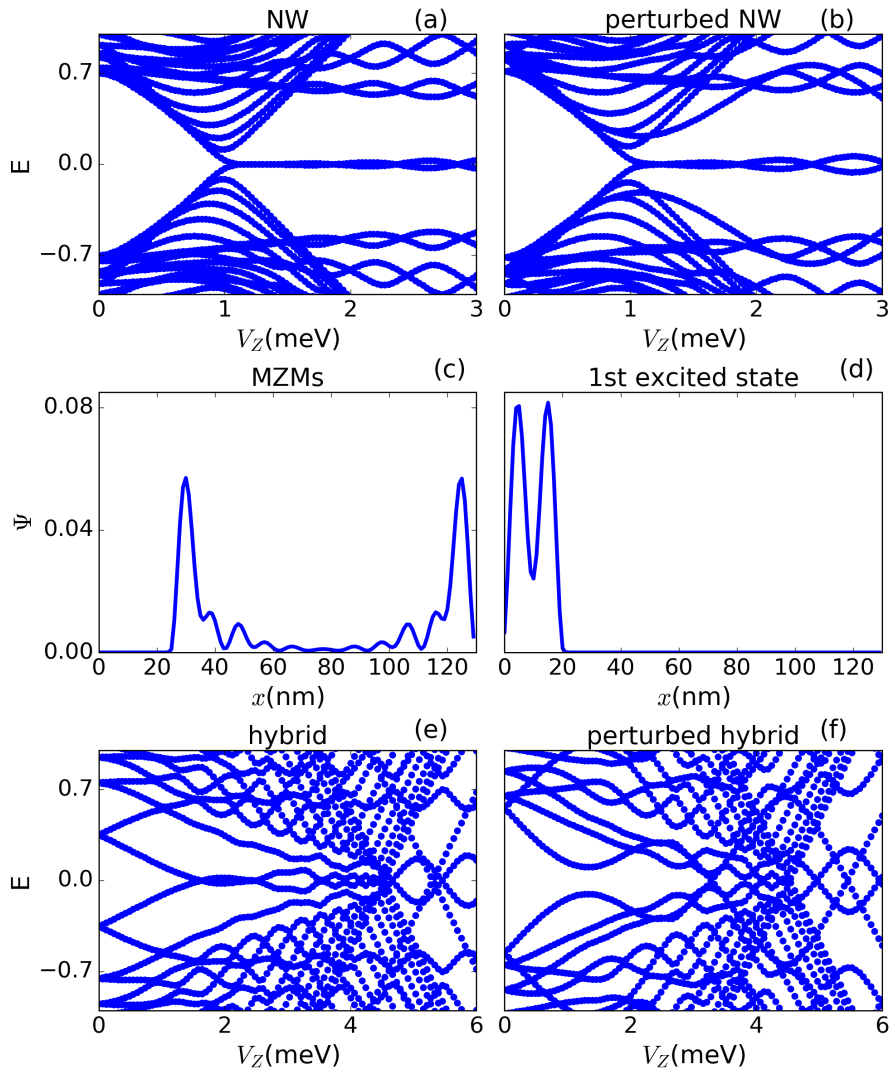

Figure 4.8: Energy spectra and wavefunctions for nanowires with length $L = 1.3$ μm and s-wave pairing $\Delta = 0.7$ meV. A smooth confinement potential with V_D =4.0 meV and length $l_D = 0.3$ μm may exist at the left end of the nanowire. A sharp square potential of height 40 meV may lie between $0.2 < x < 0.25$ μm as a perturbation. (a) Energy spectrum for a simple nanowire of chemical potential $\mu = 0.7$ meV. (b) The same nanowire as (a) but perturbed by a sharp potential. The sharp square potential is of height 40 meV and lies between $0.2 < x < 0.25$ μm. (c) the wavefunction for MBS for the nanowire with sharp potential. (d) the wavefunction for the first excited bound state confined to the left of the sharp potential. (e) energy spectrum for a trivial nanowire with $\mu = 4.5$ meV in the presence of a smooth confinement. The smooth confinement potential with V_D =4.0 meV and length $l_D = 0.3$ μm is located at the left end of the nanowire. (f) the same trivial nanowire as (e) but perturbed by a sharp square potential as (b).

nanowires in the presence or absence of a sharp potential. The numerical simulations for the corresponding differential conductance are shown in Fig. 4.7. Figure 4.7(a) shows the conductance for a topological nanowire with a smooth confinement potential at the junction interface. A MBS-induced ZBCP forms after the topological phase transition at large enough Zeeman field. In Fig. 4.7(b), a sharp potential is added inside the smooth confinement potential. Note that the inclusion of such a sharp potential changes some finite-voltage features, e.g., the gap closing pattern becomes less prominent and an additional bound state at finite energy leads to a strong resonance peak at finite voltage. However, the MBS-induced ZBCP at large Zeeman field is immune to the sharp potential due to its nonlocal topological nature. By contrast, the ABS-induced trivial ZBCP [Fig. 4.7(c)] disappears when a sharp potential is introduced, as in Fig. 4.7(d). The elimination of the near-zero-energy ABSs happens because of the breakdown of the smooth confinement condition (necessary for creating ABS). As a comparison, we also show the influence of the sharp potential on a nanowire without any confinement potential, as shown in Fig. 4.7(e) and 4.7(f). Similar to the situation in Fig. 4.7(a) and 4.7(b), the inclusion of a sharp potential only alters the conductance features at finite voltages without affecting the MBS-induced ZBCP in any essential way.

To further illustrate the effect of a sharp potential perturbation on the Majorana nanowire, we show the corresponding energy spectra and wavefunctions in Fig. 4.8. Figure 4.8(a) shows the energy spectra for a pristine Majorana nanowire, while Fig. 4.8(b) shows the spectrum for the nanowire with a sharp potential at one end. The difference between the two energy spectra is minor. The first difference

is that the amplitude for the MBS oscillation is larger in the perturbed nanowire. This happens because the MBS oscillation amplitude is an indicator for the degree of overlap between the MBSs at two wire ends. The larger MBS oscillation in Fig. 4.8(b) means a shorter distance between the two MBSs. This is confirmed in Fig. 4.8(c) where the nonlocal MBS wavefunction only resides on the right hand side of the sharp potential. The second difference between Fig. 4.8 (a) and (b) is an additional bound state at finite energy. This bound state arises from the confinement between the wire end and the sharp potential. The corresponding wavefunction is shown in Fig. 4.8(d), which is localized at one end. In Fig. 4.8 (e) and (f), we show the energy spectra for the nanowires with smooth potential at one wire end. In contrast with the pristine nanowire case, the energy spectra for the nanowire with smooth potential is strongly affected by the inclusion of a sharp potential perturbation. In the absence of any sharp potential, Fig. 4.8 (e) shows that there can be a near-zero-energy ABS in the topologically trivial regime. However, this near-zero-energy ABS is easily gapped out by a sharp potential located inside the smooth potential, as shown in Fig. 4.8 (f). So by a closer investigation of the energy spectra and wavefunctions, we find that MBSs are more robust than the ABSs against sharp potential perturbations, while smooth potential-induced ABSs easily disappear due to the presence of a sharp potential which efficiently manages to separate the ABS into distinct MBSs.

4.5 Conclusion

We have suggested, and validated through numerical simulations, simple tunneling experiment protocols in semiconductor-superconductor hybrid structures in order to provide a local distinction between trivial Andreev and topological Majorana bound states. Although any definitive evidence for such a distinction must come from nonlocal measurements in the future, the experiments proposed in the current work have the advantage of being immediately accessible experimentally. In particular, the sharp potential (Sec. 4.4) can be introduced during the growth of the nanowire enabling a prima facie distinction between ABS and MBS through a relatively straightforward transport measurement. Note that the sharp potential can be atomistically sharp, and can be easily introduced during the nanowire growth phase by suitable growth interruption on a few atomic sites to create a local defect.

We conclude by providing an outlook as well as a status update for the Majorana nanowire semiconductor-superconductor hybrid structures. Early experimental (2012-2014) observations of ZBCPs in nanowires used samples which are manifestly strongly disordered, and the ZBCPs in these experiments are likely to be simple zero-bias disordered peaks in class D systems [83, 93, 94, 71]. In these experiments, the SC gap was extremely soft and extremely weak and the ZBCP covered the whole gap. These experiments on imperfect samples are better thought of in terms of class D disorder peaks. But the recent experiments (2016-2018), starting with Deng *et al.* [31], are in clean epitaxial samples with a hard SC gap, where the issue of ABS versus MBS discussed become relevant [89]. The key question is whether

the ZBCPs in these epitaxial hard-gap, low-disorder samples arise from ABSs or MBSs. Unfortunately, as emphasized in this chapter and elsewhere, the ZBCP by itself cannot decisively settle this question since the location of the TQPT (i.e., the value of V_{Zc} in a sample) is *a priori* not known, and thus, one can never be sure whether a ZBCP, even an extremely beautiful one as in Ref. [36] with a conductance equal to the expected quantized value of $2e^2/h$, arise from MBS or ABS. Of course, if the ZBCP is seen often with the quantized conductance and the quantization is always stable to variations in V_Z and/or μ, the confidence in the existence of MBS increases substantially, but most experimental ZBCPs are results of experimental fine tuning, and as such, may arise from either MBS or ABS. Our current proposals, if experimentally implemented successfully, will greatly enhance the confidence in the existence of MBS in nanowires, but the only definitive way of establishing the existence of topological MBS is to produce a topological qubit with the appropriate non-Abelian braiding properties. Unfortunately, experiments are very far from this goal. Short of seeing successful non-Abelian braiding, one can look for end-to-end Majorana oscillation correlations as proposed in Ref. [53]. Unfortunately, even such correlation experiments have not yet been successfully performed, mainly because of problems with fabricating samples where tunneling from both wire ends can be successfully carried out (i.e., a true NSN system with tunneling possible from both ends). This is the context in which our proposed much simpler experiments make sense. The advantage of our proposals is that these experiments can be done now. The disadvantage is that, even if these experiments are successful, they would only enhance (perhaps substantially) our confidence level that the observed ZBCPs arise

from MBSs – a definitive evidence must still await the successful anyonic braiding measurement in a topological qubit.

Chapter 5

Beyond NS junction–Coulomb blockaded topological superconductor

In the previous chapters, we focused on how to detect a hybrid Majorana nanowire by observing the ZBCP in an NS junction. This is so far the most commonly performed experiment by multiple groups. However, as we discussed, it is very difficult to pin down the presence of MBSs in the Majorana nanowire simply by such NS junction measurements, since other nontopological origins for ZBCPs like smooth-confinement-induced ABSs cannot completely be excluded in principle. The reason is that NS junction conductance measurement is in principle a local measurement of the wavefunction amplitude at the interface between lead and the nanowire. It will detect a ZBCP of height $2e^2/h$ due to the particle-hole symmetry for the MBS, but it does not measure any bulk topological property of the nanowire. So in this chapter, we discuss another type of theoretical proposal which measures the topological invariant of the bulk superconductor in a more direct and definitive way.

A measure of the topological response that was originally proposed by Semenoff and Sodano [95, 96, 97, 98] involves measuring the coherent transport of electrons or "teleportation" of electrons through TSC wires with MBSs at the ends. It was

Liang Fu who realized that a charging energy is essential to the measurement of the teleportation signature using conventional transport property [99]. In the proposal, it is shown that near the Coulomb blockade resonance voltage, a single electron can tunnel from the left lead to the MBS at the left end of a Coulomb blockaded TSC nanowire, and then tunnel into the right lead from the MBS at the right end. Such a process of such single electron tunneling in and out of the TSC is coherent in nature. So if another nanowire is set up as a reference arm, and a magnetic flux is threading through the ring-shape device, the differential conductance through the NSN junction will show oscillating patterns due to the Aharanov-Bohm (AB) effect. What's more, for the TSC with opposite fermion parity, i.e., whether the fermionic state associated with the two MBSs is occupied or not, there is a π-phase shift in the oscillatory conductance pattern. Therefore, A-B effect with π-phase shift would be the hallmark of a Coulomb blockaded TSC ring.

Although the proposal is nice and elegant, there are still a couple of pitfalls for practical conductance measurement. First, Fu's teleportation proposal considers the low-energy effective theory for the TSC which is composed of MBSs only. In practice, however, the transmission quasiparticle transmission above the SC gap may also come in. Although their effects can be eliminated in the long wire limit, the precise value of the coherence length of the SC in the real experimental setup is unknown. Second, fermion parity of the TSC is not the only possible mechanism for π-phase shift in the conductance interference pattern. Nontopological reasons like trivial quantum dot can also lead to similar conductance interference patterns [100, 101, 102, 103, 104].

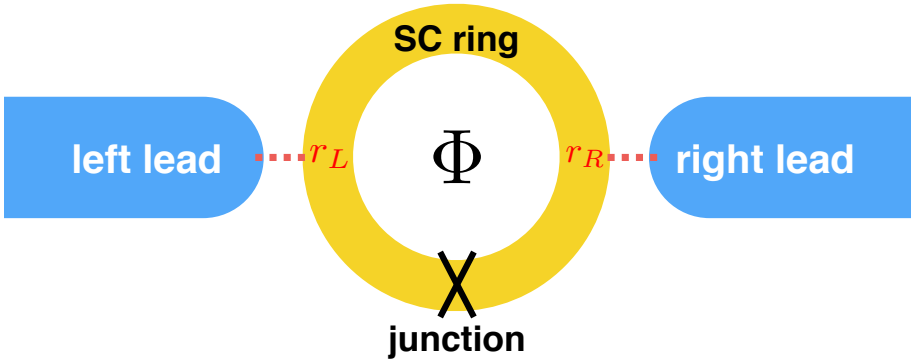

Figure 5.1: Set-up for probing Coulomb blockade transport through a TSC ring. The TSC ring is gated to allow resonant transport of a Cooper pair. Inserting a flux (entering via the junction) through the ring is expected to change the Fermion parity of the ring only in the TSC phase. The change in fermion parity pushes the ring off of resonant transport leading to a $2\Phi_0$-periodic flux dependent transport only when the ring is in a TSC phase. Increasing the transmission is expected to screen the charging energy of the ring and suppress the $2\Phi_0$-periodicity of the TSC phase.

Here, we give a proposal in which the topological invariant of a SC will show up explicitly as $2\Phi_0$-periodic oscillation in the tunneling conductance through the coulomb blockaded NSN junction. Another advantage of such an experimental setup is that the amplitude of such topological oscillation can be tuned by varying the transmission of the junction (represented by red dashed lines in Fig. 5.1). Therefore, we can know whether the oscillation is due to the topological property of the SC, or to a trivial quasi-particle transmission above the SC gap. Flux-dependent periodic conductance oscillations, i.e., AB oscillations, have already been measured in a related semiconductor ring geometry [105, 106, 107], which makes this an experimentally interesting possibility to study. We first consider transport through the TSC ring in Fig. 5.1 in weak tunneling where the rate equation formulation is used

for describing Coulomb blockade transport [108]. The ring is assumed to be gated into the resonant transmission regime for Cooper pair transport. The topological superconducting nature of the ring ensures that the parity of electrons on the ring changes [2, 3] on the insertion of a single SC flux quantum through the junction. The change in electron parity translates into a $2\Phi_0$-periodic oscillation of the conductance as seen in Fig. 5.2 (plot b). Following this, we account for the screening of the Coulomb blockade in the intermediate tunneling regime by generalizing the well-known Ambegaokar-Eckern-Schön(AES) model [109] for the description of the SC Coulomb blockade to the case of SC rings (shown in Fig. 5.1). From this description we show that the thermodynamic properties of the system, in the weak charging energy limit, depend explicitly on the topological invariant of the TSC ring [2]. From an analytic continuation of imaginary time correlations, we find that the $2\Phi_0$-periodic part of the conductance oscillations are screened (plot c in Fig. 5.2) and are virtually eliminated (plot d in Fig. 5.2) in the strong tunneling limit where the conductance oscillations are just Φ_0-periodic. The dependence of the conductance on the transmission through the ring allows us to clearly differentiate the non-topological $2\Phi_0$ oscillations (plot a) and $2\Phi_0$-periodic topological conductance oscillations (plot b) from Fig. 5.2. Finally, we talk about the conductance through the NSN junction in the limit of no Coulomb blockade.

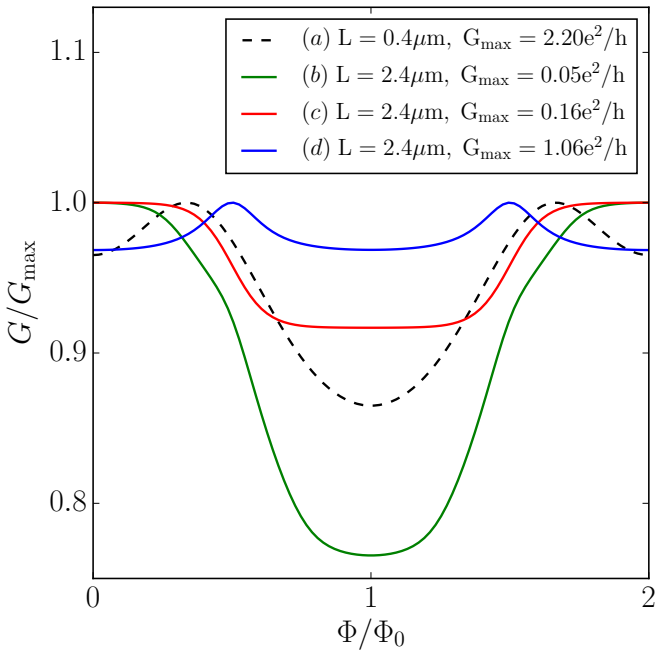

Figure 5.2: Conductance as a function of the magnetic flux Φ through the SC ring, as transmission through the ring, which determines $G_{\max}$ is varied. (a) shows $2\Phi_0$-periodic oscillations for a short non-topological SC ring due to the conventional AB effect. (b) shows topological $2\Phi_0$-periodic oscillations of a long TSC ring at small conductance $G_{\max}$ so as to be in the strong Coulomb blockaded regime. (c) shows the conductance of the TSC ring as $G_{\max}$ is increased, which in turn reduces the topological $2\Phi_0$-periodic oscillations. (d) shows that the $2\Phi_0$-periodic oscillations are completely eliminated in the long TSC ring at large $G_{\max}$, where there is no Coulomb blockade.

5.1 Strong Coulomb blockade

While the structure in Fig. 5.1 is reminescent of the interferometric teleportation measurement that would show $2\Phi_0$-periodic conductance oscillations for a topological state, it will be more convenient to think about the transport in terms of Andreev transport through a TSC ring similar to the one considered from the fractional Josephson effect. The fractional Josephson effect leads to a change in the

ground state charge of the TSC ring in Fig. 5.1 as the flux in the ring is changed by a SC flux quantum [3, 2]. In fact, this behavior uniquely characterizes the TSC state. This change in the ground state charge can be measured using Coulomb blockade transport through the ring in Fig. 5.1. By tuning the gate voltage to a degeneracy of even charge states of the ring so that Cooper pairs can be transported across the ring. For this value of gate voltage, the odd charge sector is non-degenerate and is essentially insulating in the strong Coulomb blockade limit. For conventional SC dots [108, 110], this gate voltage would correspond to a resonance of Cooper pair transport. In the case that the ring is in the TSC phase, the ground state has an odd number of electrons for fluxes that are odd multiples of Φ_0. The conductance through the ring is thus suppressed for fluxes Φ that are odd multiples of Φ_0 resulting in a $2\Phi_0$ flux periodicity of the conductance of the ring.

The $2\Phi_0$ flux periodicity for the conductance in the TSC state of the ring can be seen directly from the numerical result Fig. 5.2 (plot b). The conductance of the TSC ring in the strong Coulomb blockade (or equivalently weak tunneling) regime can be computed within the semi-classical approximation using the rate equation formalism analogous to previous work on conventional SC quantum dots [108]. In the limit of weak tunneling and low temperatures (compared to charging energy), we can restrict attention to three charge states $0, 1$ and 2 electrons (in the background of $2N$ electrons) with occupation probabilities $\pi_{0,1,2}$. Since the odd (i.e. charge 1) state is off-resonant in energy, it does not conduct and the conductance is found to

be essentially proportional to the even occupation $(\pi_0 + \pi_2)$ and is written as

$$G(\Phi) = (\pi_0 + \pi_2)2g_0 + G_d(\Phi), \tag{5.1}$$

where $G_d(\Phi)$ is an electron co-tunneling process that does not depend on the occupation probabilities π_j and is exponentially small in the limit of a large ring ($L \gg \xi$, where ξ is the coherence length). g_0 is the local Andreev reflection probability in the symmetric case in the limit of weak charging energy (compared to gap Δ), which has a weak but Φ_0-periodic flux dependence. In contrast the occupation factor $\pi_0 + \pi_2 \approx \{1 + \frac{1}{2}e^{-\beta\Delta_{\text{parity}}(\Phi)}\}^{-1}$, where $\Delta_{\text{parity}}(\Phi)$ is the energy difference between even and odd Fermion parity ground states, is $2\Phi_0$ periodic because of the $2\Phi_0$ periodicity of Δ_{parity}. This parity of Δ_{parity} is a necessary consequence of the change in the Fermion parity of the ground state from even to odd and back with every insertion of a SC flux quantum Φ_0 into the ring. The resulting conductance $G(\Phi)$ for the TS ring is plotted in Fig. 5.2 (plot b) and shows a $2\Phi_0$ periodicity of conductance.

5.2 Weak and intermediate Coulomb blockade

5.2.1 Partition function: Generalized AES model for NSN junction

The ability to clearly distinguish the $2\Phi_0$ oscillation arising from the TSC phase (Fig. 5.2 plot b) and the nontopological AB oscillations (Fig. 5.2 plot a) depends on being able to turn on and off the Coulomb blockade in a single device. We show that

this can be done by taking advantage of the screening of the Coulomb interaction that results from raising the tunnel coupling between the leads and the quantum dot (or TSC ring in Fig. 5.1). Such a quenching of charging energy, which depends on quantum coherent charge fluctuations between several charge states, has been demonstrated in related setups such as conventional metallic quantum dots [111] and also Majorana nanowires [112] using Bosonization. Below we generalize the AES [109, 113] approach to the class D superconducting quantum dots.

The starting point of the derivation of the AES model is the partition function for the Coulomb blockaded NSN junction as shown in Fig. 5.1. Using Feynman's imaginary-time path integral formalism [114, 115], the partition function is

$$
\begin{aligned}
Z &= \int \mathcal{D}\overline{\psi}\mathcal{D}\psi e^{-S}, \\
S &= S_0 + S_{\rm g} + S_{\rm c} + S_{\rm lead}, \\
S_0 &= \sum_{\alpha\beta} \int dx \overline{\psi}_\alpha(x) \Big[\partial_\tau \delta_{\alpha\beta} + h_{\alpha\beta}(\mathbf{r}) - \mu\delta_{\alpha\beta}\Big]\psi_\beta(x), \\
S_{\rm g} &= -g \int dx \overline{\psi}_\downarrow \overline{\psi}_\uparrow \psi_\uparrow \psi_\downarrow(x), \\
S_{\rm c} &= E_c \int_0^\beta d\tau \Big[N(\tau) - N_g\Big]^2, \\
S_{\rm lead} &= \sum_{\alpha=\uparrow\downarrow} \sum_{a=L,R} \int_0^\beta d\tau_2 d\tau_1 \overline{\psi}_\alpha(\tau_2, r_a) \Sigma_a^0(\tau_2 - \tau_1) \psi_\alpha(\tau_1, r_a), \\
\Sigma_a^0(\tau) &= \frac{-\Gamma_a/\beta}{\sin(\pi\tau/\beta)}, \quad \Gamma_a = \pi t_a^2 d(\epsilon_F, a)
\end{aligned}
\tag{5.2}
$$

where S_0 is the semiconductor or bare metal in the island, $S_{\rm g}$ is the point-like attractive pairing interaction which is responsible for the SC effect, $S_{\rm c}$ is the capacitive

charging energy of electrons on the island, and S_{lead} is the self-energy obtained by integrating out the electrons in the Normal-metal leads. $\psi_\alpha(x)$ is the Grassmann field for electrons on the island with spin α and time-space argument $x = (\tau, \mathbf{r})$. The imaginary time τ is bounded from 0 to inverse temperature β. $r_{L,R}$ are the locations at the edge of the island where electron tunneling between the lead and the semiconductor takes place, as shown in Fig. 5.1. $\Sigma_a^0(\tau)$ is the self-energy from the lead with t_a being the tunneling amplitude between lead-a and the SC island, and $d(\epsilon_F)$ being the local density of states at the end of the lead that is closer to the SC island. The detailed derivation of the self-energy term is in Appendix. A. Next, we need to decompose the quartic terms (S_{g} and S_{c}) into quadratic forms of Grassmann fields. We perform the Hubbard-Stratonovich transformation twice so that

$$
\begin{aligned}
Z &= \int \mathcal{D}\overline{\psi}\mathcal{D}\psi\mathcal{D}\overline{\Delta}\mathcal{D}\Delta\mathcal{D}V e^{-S}, \\
S &= S_{\text{sc}} + S_{\text{lead}} + \int dx \frac{|\Delta(x)|^2}{g} + \int d\tau \frac{V(\tau)^2}{E_c}, \\
S_{\text{sc}} &= S_0 + \int dx \Big[\Delta(x)\psi_\uparrow\psi_\downarrow(x) + \Delta^*(x)\overline{\psi}_\downarrow\overline{\psi}_\uparrow(x)\Big] - i\int d\tau V(\tau)\Big[N(\tau) - N_g\Big]. \quad (5.3)
\end{aligned}
$$

Here $\Delta(x)$ is the bosonic complex auxiliary field introduced by the Hubbard-Stratonovich(HS) transformation of the pairing interaction, and the physical meaning of $\Delta(x)$ is the SC order parameter. We can ignore the spatial dependence of the order parameter since a priori there is no supercurrent in the island. We also approximate the amplitude by the mean-field value and ignore the massive fluctuations. Therefore

the SC order parameter can be simplified as $\Delta(x) \simeq \Delta_0 e^{i\phi(\tau)}$. On the other hand, $V(\tau)$ is the bosonic real auxiliary field introduced by the HS transformation of the charging energy term, and the corresponding physical meaning is the source-drain voltage. After the HS transformation, our action becomes quadratic in terms of the Grassmann fields. But before we integrate out the electrons, we first perform a gauge transformation so that the new Grassmann field absorbs the phase of the SC order parameter:

$$\begin{aligned}
&\psi'_\alpha = e^{i\phi(\tau)/2}\psi_\alpha, \\
&\overline{\psi}'_\alpha = e^{-i\phi(\tau)/2}\overline{\psi}_\alpha, \\
&\partial_\tau \to \partial_\tau - i\frac{\phi(\tau)}{2}, \\
&\Sigma_a(\tau_2 - \tau_1) = \Sigma_a^0(\tau_2 - \tau_1)e^{\frac{i}{2}[\phi(\tau_2)-\phi(\tau_1)]}.
\end{aligned} \tag{5.4}$$

Note how the boundary condition for the Grassmann field changes after the gauge transformation. To be specific, the boundary condition of the gauged Grassmann field

$$\psi'_\alpha(\beta) = e^{i\phi(\beta)/2}\psi_\alpha(\beta) = -e^{i\phi(0)/2+i\pi n_w}\psi_\alpha(0) = (-)^{n_w+1}\psi'_\alpha(0), \tag{5.5}$$

is anti-periodic (periodic) boundary condition if the winding number of the SC phase is even (odd). This alternative boundary condition is crucial when we integrate out the electrons on the SC island. Another consequence of such a gauge transformation is the deviation of the chemical potential, i.e., $\delta\mu(\tau) = i\Big[\frac{\dot{\phi}(\tau)}{2} + V(\tau)\Big]$. The simple

fact that the hybrid nanowire (semiconductor+proximity SC) has a large density of electrons suppresses the chemical potential fluctuation and therefore locks the voltage and phase field by $V(\tau) = -\frac{\dot{\phi}(\tau)}{2}$, which is also called Josephson relation. Now the partition function becomes

$$
\begin{aligned}
Z &= \int \mathcal{D}\overline{\psi}\mathcal{D}\psi\mathcal{D}\phi e^{-S} = \sum_{n_w}\int_{n_w}\mathcal{D}\phi\int\mathcal{D}\overline{\psi}\mathcal{D}\psi e^{-S_{n_w}[\overline{\psi},\psi,\phi]},\\
S_{n_w}[\overline{\psi},\psi,\phi] &= \int d\tau\Big(\frac{\dot{\phi}^2}{4E_c} - \frac{i}{2}N_g\dot{\phi}\Big) + \sum_{\alpha,a}\int d\tau_2 d\tau_1 \overline{\psi}_\sigma(\tau_2, r_a)\Sigma_a(\tau_2,\tau_1)\psi_\alpha(\tau_1, r_a)\\
&+ \sum_{\alpha\beta}\int dx\overline{\psi}_\alpha\Big[\partial_\tau\delta_{\alpha\beta} + h_{\alpha\beta}(\mathbf{r}) - \mu\delta_{\alpha\beta}\Big]\psi_\beta + \Delta_0\int dx\Big(\psi_\uparrow\psi_\downarrow + \overline{\psi}_\downarrow\overline{\psi}_\uparrow\Big).
\end{aligned}
\tag{5.6}
$$

Now we can integrate out the electrons (see Appendix. B for details) and get the partition function for the NSN junction in terms of only the SC phase

$$
\begin{aligned}
Z &= \sum_{n_w} Z_{\mathrm{BCS}}^{P(n_w)}\int_{n_w}\mathcal{D}\phi(\tau)e^{-S_{n_w}[\phi]},\\
S_{n_w}[\phi] &= S_\phi^0 - \frac{1}{2}\mathrm{Tr}\log(1 - \mathrm{G_{sc}}\Sigma),\\
S_\phi^0 &= \int_0^\beta d\tau\left(\frac{\dot{\phi}^2}{4E_c} - iN_g\frac{\dot{\phi}}{2}\right).
\end{aligned}
\tag{5.7}
$$

Here $Z_{\mathrm{BCS}}^{P(n_w)}$ is the partition function for the isolated BCS mean-field SC. It depends only on the parity of the winding number $P(n_w) = n_w \bmod 2$. G_{sc}, Σ are the superconductor Green's function and the self-energy from lead both in the Nambu basis. The integral over the phase variable $\mathcal{D}\phi$ is split into winding number sectors labelled by n_w, which is defined by the boundary conditions of the superconducting phase as $\phi(\beta) - \phi(0) = 2\pi n_w$. Here $Z_{\mathrm{BCS}}^{P(n_w)}$ is the partition function of the isolated

superconducting ring within the BCS approximation, i.e., ignoring charging energy, which is included in the kinetic action of the phase. The partition function within the BCS approximation depends only on the parity of the winding number $P(n_w) = n_w \bmod 2$, since this parity sets the boundary conditions on the Grassmann field ψ. As a result, the BCS partition function of the isolated ring for different winding number parities is related as

$$Z^1_{\rm BCS} = Z^0_{\rm BCS} \text{sign Pf}(H_{\rm BCS}) \prod_m \tanh\Big(\frac{\beta\epsilon_m}{2}\Big), \tag{5.8}$$

where $H_{\rm BCS}$ is the BCS mean-field Hamiltonian in the Majorana basis [2] for the isolated ring in Fig. 5.1 and $\epsilon_m > 0$ are the excitation energies of $H_{\rm BCS}$.

The ratio $Z^1_{\rm BCS}/Z^0_{\rm BCS}$ contribution to the partition function is of particular interest because the factor sign Pf$(H_{\rm BCS})$, where $H_{\rm BCS}$ is the BdG Hamiltonian of the SC ring, is closely related to the topological invariant of the SC ring [2]. Specifically, the TSC phase is uniquely determined to be topologically non-trivial if sign Pf$(H_{\rm BCS})$ flips between $+1$ to -1 on insertion of a SC flux quantum into to the ring shown in Fig. 5.1. For a long SC ring, all other contributions to the conductance such as g_0 are Φ_0-periodic. This leads to a $2\Phi_0$-periodic contribution to the partition function and ultimately to the total conductance G of the system as a unique property of the TSC phase.

Coupling of the ring to the metallic lead in Fig. 5.1 appears in the partition function Eq. (5.7) through the term $G_{\rm sc}\Sigma$, where $G_{\rm sc}$ is the Green's function of the ring associated with $H_{\rm BCS}$. To simplify this lead coupling term in the action, we

assume the SC gap of $H_{\rm BCS}$ to be larger than both the charging energy and the temperature such that the SC Green's function $G_{\rm sc}$ can be assumed to be local in both time and space. Additionally assuming that the lead self-energy Σ is smaller than the gap $\Delta \sim G_{\rm sc}^{-1}$, we can expand the trace term in Eq. (5.7) up to quadratic order of $G_{\rm sc}\Sigma$, and the effective action for each winding number sector of the system becomes

$$S_{n_w}[\phi] = S_\phi^0 + \sum_a g_a \int \frac{d\tau_1 d\tau_2}{\beta^2} \frac{1-\cos[\phi(\tau_1)-\phi(\tau_2)]}{\sin^2[\pi(\tau_1-\tau_2)/\beta]}, \tag{5.9}$$

where $g_a \sim {\rm Tr}[{\rm G_{sc}}\Sigma_{\rm a}{\rm G_{sc}}\Sigma_{\rm a}]$ is the local conductance through either metallic lead to SC ring, as shown in Fig. 5.1. This effective action is an important result in our work, which is identical the dissipative tunneling action first derived by AES [109, 113]. It includes the effect of phase fluctuation in the Coulomb blockaded SC for which the charge quantization is apparent. What's more, what makes it different from the conventional AES action is the inclusion of a topological invariant in the ratio of odd/even winding number sector partition function, i.e., $Z^1_{\rm BCS}/Z^0_{\rm BCS}$. In this sense, we may call the generalization "topological AES action".

5.2.2 Conductance

While the partition function Eq. (5.7) for the NSN junction in Fig. 5.1 has a clear dependence on the topological invariant through Eq. (5.8), the most convenient observable associated with direct experimental measurement is the dc conductance. However, the conductance for tunneling junction is notoriously difficult to calcu-

late than thermodynamic averages, because it requires analytic continuation of the response functions from imaginary to real times or frequencies. To avoid the difficulty of direct analytic continuation, we take advantage of the fact that the dc conductance in the symmetric case (i.e., $g_L = g_R = g_0$) can be aproximated by the interpolation formula of a two-point phase correlator [116]

$$\begin{aligned} G &\simeq g_0 \mathcal{G}(\beta/2), \\ \mathcal{G}(\tau) &= \langle e^{i\phi(\tau)} e^{-i\phi(0)} \rangle. \end{aligned} \tag{5.10}$$

It gives a reasonable approximation for the conductance over the entire range of parameters, e.g., temperature T, bare conductance g_0, and reference electron number N_g. Using the winding number decomposition of the partition function in Eq. (5.7), the conductance G can be expressed as

$$G = g_0 \left[\mathcal{G}_0 + \frac{\sum_{n_w \neq 0} \left(\mathcal{G}_{n_w} - \mathcal{G}_0 \right) \frac{Z_{n_w}}{Z_0}}{1 + \sum_{n_w \neq 0} \frac{Z_{n_w}}{Z_0}} \right], \tag{5.11}$$

where $\mathcal{G}_{n_w}$ and Z_{n_w} are the two-point correlation function and partition function for the particular winding number sector n_w. As shown in Appendix.C, Z_{n_w} is suppressed by high temperature as $e^{-\pi^2 n_w^2 T/E_C}$ (in addition to tunneling) so that we can restrict the summation to $n_w = 0, \pm 1$:

$$G \simeq G_0 + \left(G_1 - G_0 \right) \frac{Z_1}{Z_0} + (1 \to -1). \tag{5.12}$$

The ratio $Z_{\pm 1}/Z_0$ computed in the Appendix.C is

$$\frac{Z_{\pm 1}}{Z_0} = \text{sign Pf}(H_{\text{BdG}}) \prod_m \tanh\Big(\frac{\beta\epsilon_m}{2}\Big) e^{\pm i\pi N_g} e^{-\frac{\pi^2}{\beta E_c}} e^{-2g_0}. \tag{5.13}$$

It shows that in addition to a high temperature suppression, $Z_{\pm 1}$ is also suppressed compared to Z_0 as the tunnel conductance g_0 is increased beyond $g_0 > 1$, which can be achieved for multi-channel metallic lead. While Eq. (5.12) contains a topological contribution proportional to $Z_{\pm 1}/Z_0$, this contribution can only be substantial only if $G_1 - G_0$ is comparable to G_0. Considering the fact that the conductance G is related to the phase correlator [Eq. (5.10)], we find (see Appendix C) that G_1 and G_0 have opposite signs according to the equation

$$\begin{aligned} G_{n_w} &\simeq (-1)^{n_w} g_0 C_{n_w} \\ C_{|n_w|} &= \prod_{p'_n>0} \exp\Big\{ - \frac{1}{\frac{\beta p'^2_n}{8E_c} + g_0(|n'_p| - |n_w|)\Theta(|n'_p| - |n_w|)} \Big\}, \end{aligned} \tag{5.14}$$

where $p'_n = 2\pi n'_p/\beta$, with $n'_p = 1, 3, 5, ...$

5.3 No Coulomb blockade

The $2\Phi_0$-periodicity in the Coulomb blockade limit despite being quite unique to the TSC phase can also arise from the conventional AB effect [117, 118, 119], which is contained in the G_d contribution in Eq. (5.1). This contribution does not depend on the occupation probabilities π_j and is not affected by the Coulomb blockade. Therefore, we expect that the conventional AB type contribution to the con-

ductance can be isolated from studying the conductance in the absence of Coulomb blockade [117, 118].

The conductance in the absence of Coulomb blockade can be computed by assiging a classical chemical potential to the superconductor and considering the device in Fig. 5.1 as two conductances in series. Specifically, the current in each lead L, R can be expressed in terms of the voltage difference $V_{j=L,R}$ of the lead j and the SC as $I_l = \sum_j G_{lj} V_j$, where G_{lj} are a set of condutances of an NSN junction that may be computed from the scattering matrix [120]. The total conductance of the so-called floating superconductor system can be shown to be [121, 122, 123]

$$G = \frac{G_{LL}G_{RR} - G_{LR}G_{RL}}{G_{LL} + G_{RR} + G_{LR} + G_{RL}}, \tag{5.15}$$

where the NSN junction conductances G_{jl} can be computed numerically using KWANT for a Majorana nanowire model as a function of flux Φ. As seen from plot a in Fig. 5.2, the off-diagonal conductance G_{LR}, G_{RL} (which are closely related to G_d) in a short wire, leads to a $2\Phi_0$ periodicity of the conductance for the Majorana nanowire (whether or not in the TS phase). This can be interpreted to be a result of the conventional AB effect resulting from quasiparticles interfering around the ring. Such non-local transport of quasiparticles is expected to be suppressed in the case of a long wire, which shows conventional (i.e. Φ_0) periodicity of conductance even in the TSC phase as seen from plot d in Fig. 5.2. Thus the doubled flux periodicity arising from the TSC phase can be distinguished from that arising from the AB effect by comparing the conductance with and without Coulomb blockade.

5.4 Discussion and Conclusion

In this chapter, we propose an NSN junction with a Coulomb blockaded SC ring being connected by two metallic leads. We show that in the intermediate Coulomb blockade regime, the topological invariant of the SC ring will explicitly show up in the tunnel conductance through the junction. For a TSC ring, the conductance shows a $2\Phi_0$-periodic pattern as a function of the magnetic flux threading through the Coulomb blockaded SC ring. What's more, such a $2\Phi_0$-periodic pattern in conductance can be amplified (reduced) by decreasing (increasing) the transmission through the junction. Therefore we can differentiate the $2\Phi_0$-periodic contribution between TSC and trivial quasi-particle transport. We emphasize that our proposal deals with the bulk property of the SC ring, and thus is robust against any local trivial mechanisms like disorder or trivial ABSs and etc.

Chapter 6

Conclusion

One-dimensional superconductor-semiconductor nanowire is a topic of active research over the last decade. It is so far the most feasible platform to host non-Abelian Majorana bound states and therefore can implement fault-tolerant topological quantum computation. Since the early theoretical proposal, a lot of experimental progress has been achieved, making it an exciting and dynamic field of research.

In Chapter 1, we gave an introduction of MBS in TSC. We focused on two models – one is the spinless p-wave superconductor (Kitaev chain), and the other is the SOC semiconductor-superconductor nanowire. The latter would be the theme for the rest of the thesis. We also discussed the most important experimental signal for the existence of MBS, i.e., a ZBCP of height $2e^2/h$ in the tunnel conductance through the NS junction.

In Chapter 2, we carried out a realistic simulation of Majorana nanowires in order to understand the high quality experimental data [30, 34, 35]. In the process, we developed a comprehensive picture for what physical mechanisms may be operational in realistic nanowires leading to discrepancies between minimal theory and experimental observations. We especially analyzed the role of dissipation in the nanowire to explain the weakness and broadening of the ZBCP and breaking of

particle-hole symmetry.

In Chapter 3, we discussed the possible existence of topologically trivial ABS induced by a smooth potential in disorder-free hybrid nanowires. They are also near-zero-energy bound states and resemble the MBS in the tunnel conductance spectra, although these smooth-potential-induced ABS are nontopological. For completeness, we considered the case of a smooth potential being located outside the nanowire and the case of inhomogeneous potential extending all the way into the nanowire. We find these two cases are adiabatically connected, with only the range of Zeeman field for the ABS being different. So such a topologically trivial ABS is very generic in superconductor-semiconductor nanowires, and one has to exclude these ABS before the confirmation of MBS.

In Chapter 4, following the discussion in Chapter 3, we gave multiple proposals for how to differentiate between ABS and MBS in the context of NS junction. Through extensive numerical simulations, we show how the variation of the tunnel potential, the variation of the effective length of the nanowire, the variation of an external dot state, and most importantly, the inclusion of a sharp potential would change the tunnel conductance spectra in cases with ABS or MBS.

In Chapter 5, we went beyond NS junction and gave a theoretical proposal to directly measure the topological invariant of the SC. The proposed experimental setup is an NSN junction with coulomb blockaded SC ring being located in the middle. The conductance would show a 2Φ-periodic oscillation as a function of the magnetic flux threading through the SC ring, if the SC is in the topological phase. Another advantage of such a junction is that we can differentiate the 2Φ-periodic

oscillation from topology and from quasi-particle transport, by simply varying the transmission transparency from the metallic leads.

In this thesis, we investigated signatures of both Majorana and Andreev bound states. One of our important finding is that smooth-potential-induced ABS can exist generically, and mimic many behaviors of MBS in the tunnel conductance spectra. Therefore people should be very cautious about interpreting the ZBCP as the indication of MBS, since it may also arise from trivial ABS. Based on the experimental status nowadays, we discussed several practical proposals to differentiate between ZBCPs induced by ABS and MBS. For future experiments, we also gave theoretical proposals that can detect the topological invariant of TSC in a direct way.

Appendix A

Self-energy from the normal-metal lead

In this appendix we derive the self-energy from the normal-metal lead in Chapter. 5. When an electronic system is coupled to a normal-metal lead, the influence from the lead on the system can be summarized in a term called self-energy. In this appendix, we call this electronic system 'dot' without loss of generality. The expression of self-energy shows up in a clear way in the path integral formalism. The partition function for the total system including the dot and the lead is

$$\begin{aligned} Z &= \int \mathcal{D}\overline{\psi}_L \mathcal{D}\psi_L \mathcal{D}\overline{\psi}_0 \mathcal{D}\psi_0 e^{-S_0 - S_L - H_T} \\ S_L &= \int dx \overline{\psi}_L (\partial_\tau + h_L)\psi_L(x) \\ H_T &= \int d\tau \Big[- t\overline{\psi}_L(\tau, R)\psi_0(\tau, r_0) - t^* \overline{\psi}_0(\tau, r_0)\psi_L(\tau, R) \Big], \end{aligned} \tag{A.1}$$

where S_0 (S_L) is the action for the dot (lead), and H_T describes the process of a single electron tunneling between r_0 in the dot and R in the lead. $x = (\tau, r)$ is the space-time argument of the Grassmann field for electrons. We then complete the square for fields in the lead, i.e.,

$$S_L + H_T = - \int (\overline{\psi}_L + \int \overline{\psi}_0 t^* G) G^{-1} (\psi_L + \int G t \psi_0) + \int \overline{\psi}_0 t^* G t \psi_0, \tag{A.2}$$

where $G = -\partial_\tau - h_L$ is the Green's function for the isolated lead. Now by integrating out the electrons in the lead, the partition function becomes

$$\begin{aligned} Z &\propto \int \mathcal{D}\overline{\psi}_0 \mathcal{D}\psi_0 e^{-S_0 - S_{\rm SE}}, \\ S_{\rm SE} &= \int_0^\beta d\tau_2 d\tau_1 \overline{\psi}_0(\tau_2, r_0)\Sigma(R, \tau_2 - \tau_1)\psi_0(\tau_1, r_0), \\ \Sigma(R, \tau_2 - \tau_1) &= t^* G(R, \tau_2 - \tau_1) t, \end{aligned} \tag{A.3}$$

where $\Sigma(R, \tau_2 - \tau_1)$ is the self-energy from the lead. Note that although the self-energy is local in space, it is nonlocal in time, as a typical electron will itinerate in the lead before tunneling back to the dot. We can further calculate the closed form of the self-energy by working in the frequency representation.

$$\begin{aligned} &\Sigma(R, i\omega_n) = t^2 G(r, i\omega_n) = t^2 \langle R|(i\omega_n - h_L)^{-1}|R\rangle \\ &\simeq t^2 d(\epsilon_F)|\langle R|k_F\rangle|^2 \int d\xi \frac{1}{i\omega_n - \xi} = -i\Gamma \,\mathrm{sgn}(\omega_n), \end{aligned} \tag{A.4}$$

where $i\omega_n = (2n+1)\pi/\beta$ and $\Gamma = \pi t^2 d(\epsilon_F)|\langle R|k_F\rangle|^2$. Here $d(\epsilon_F)$ is the density of states of the lead at Fermi energy, and $\langle R|k_F\rangle$ is the wavefunction amplitude at R.

On the other hand, to calculate the self-energy in the temporal representation, we first introduce an exponential ultra-violet suppression factor $e^{-|\omega_n|/\Lambda}$ and set Λ

to infinity at the end of the calculation, i.e.,

$$\sum_{\omega_n} \mathrm{sgn}(\omega_n) e^{-i\omega_n \tau} e^{-|\omega|/\Lambda} = \sum_{\omega_n > 0} \left[e^{(-i\tau - \Lambda^{-1})\omega_n} - e^{(i\tau - \Lambda^{-1})\omega_n} \right]$$
$$= \frac{e^{-i\tau\pi/\beta}}{1 - e^{-i\tau 2\pi/\beta}} - \frac{e^{i\tau\pi/\beta}}{1 - e^{i\tau 2\pi/\beta}} = \frac{-i}{\sin(\pi\tau/\beta)}. \tag{A.5}$$

Thus we obtain the self-energy term in the temporal representation:

$$\Sigma(\tau) \simeq \frac{1}{\beta} \sum_{\omega_n} \Sigma(i\omega_n) e^{-|\omega|/\Lambda} e^{-i\omega_n \tau} = \frac{-\Gamma/\beta}{\sin(\pi\tau/\beta)}. \tag{A.6}$$

Appendix B

Partition function of the mean-field SC

In this appendix, we calculate the partition function for the BCS mean-field superconductor with either anti-periodic or periodic boundary condition in imaginary time. The partition function is

$$
\begin{aligned}
&Z_{\mathrm{BCS}}^{n_w} = \int \mathcal{D}\overline{\psi}\mathcal{D}\psi e^{-S}, \\
&S = \sum_{\alpha\beta} \int dx \overline{\psi}_\alpha \Big[\partial_\tau \delta_{\alpha\beta} + h_{\alpha\beta}(\mathbf{r}) - \mu\delta_{\alpha\beta}\Big]\psi_\beta + \Delta_0 \int dx \Big(\psi_\uparrow\psi_\downarrow + \overline{\psi}_\downarrow\overline{\psi}_\uparrow\Big).
\end{aligned} \tag{B.1}
$$

To integrate out the electrons, we first transform the complex Grassmann numbers to real (Majorana) Grassmann numbers:

$$
\begin{aligned}
&\psi_a(\tau) = \Big[\gamma_{a1}(\tau) + i\gamma_{a2}(\tau)\Big]/\sqrt{2} \\
&\overline{\psi}_a(\tau) = \Big[\gamma_{a1}(\tau) - i\gamma_{a2}(\tau)\Big]/\sqrt{2}, \\
&\{\gamma_{ai}, \gamma_{bj}\} = 0,
\end{aligned} \tag{B.2}
$$

where a, b denote the combined indices of space and spin, and $i, j = 1, 2$. Thus the partition function becomes

$$
\begin{aligned}
Z_{\mathrm{BCS}}^{n_w} &= \int \mathcal{D}\Gamma(\tau) e^{-S}, \\
S &= \frac{1}{2} \int d\tau \Gamma^T(\tau) \Big[\partial_\tau + i A_{\mathrm{sc}} \Big] \Gamma(\tau),
\end{aligned}
\tag{B.3}
$$

where A_{sc} is real and anti-symmetric. A_{sc} can be further transformed into a nearly diagonal form D by an orthogonal transformation:

$$
\begin{aligned}
D = W A_{\mathrm{sc}} W^T &= \sum_{\oplus} D_m = \sum_{\oplus} \begin{pmatrix} 0 & \epsilon_m \\ -\epsilon_m & 0 \end{pmatrix}, \\
\chi &= W\Gamma,
\end{aligned}
\tag{B.4}
$$

with $\epsilon_m \geq 0$ being the single-particle excitation energies of the superconducting system and $\det(W) = \pm 1$. So the partition function can be written as

$$
\begin{aligned}
Z_{\mathrm{BCS}}^{n_w} &= \int \mathcal{D}\chi(\tau) J(W) e^{-S}, \\
S &= \frac{1}{2} \int d\tau \chi^T(\tau) \Big(\partial_\tau + i D \Big) \chi(\tau),
\end{aligned}
\tag{B.5}
$$

where the Jacobian for the orthogonal transformation is

$$
J(W) = \det(W)^{\dim(1_\tau)}, \tag{B.6}
$$

for which $\dim(1_\tau)$ is the dimension of the imaginary time space, which can be also obtained from the Fourier space. We perform the Fourier transformation for the Majorana Grassmann numbers:

$$\chi(\tau) = \frac{1}{\beta}\sum_{\omega_n}\chi(\omega_n)e^{-i\omega_n\tau},$$
$$\overline{\chi}(-\omega_n) = \chi(\omega_n), \tag{B.7}$$

where ω_n is odd(even) for even(odd) winding numbers. However $\chi(\omega_n)$ is no longer self-adjoint, so in order to have self-adjoint Grassmann numbers, we make one more unitary transformation

$$\chi_+(\omega_n) = \frac{1}{\sqrt{2}}\Big[\chi(\omega_n) + \chi(-\omega_n)\Big],$$
$$\chi_-(\omega_n) = \frac{-i}{\sqrt{2}}\Big[\chi(\omega_n) - \chi(-\omega_n)\Big], \tag{B.8}$$

for $\omega_n > 0$. Note that the zero-frequency mode χ_0, if there exists, is already self-adjoint. Now we can see that $\dim(1_\tau)$, which is equal to $\dim(1_\omega)$, is an even number for odd frequencies (even winding numbers), since the total space in frequency representation is the direct sum of 2-dimensional subspaces spanned by $\chi_\pm(\omega_n)$ for positive ω_ns, while $\dim(1_\tau)$ is an odd number for even frequencies (odd winding numbers) due to the additional 1-dimensional subspace spanned by χ_0. Thus the

Jacobian for the orthogonal transformation is

$$J(W) = \det(W)^{n_w}. \tag{B.9}$$

Now we are ready to calculate the partition function. First we calculate the odd frequency (even winding number) case, for which the partition function is

$$\begin{aligned} Z_{\mathrm{BCS}}^{\mathrm{even}} &= \int \mathcal{D}\chi e^{-S}, \\ S &= \frac{1}{2}\sum_{\omega_n>0}\sum_{m} \chi_{\omega,m}^{T} B_{\omega,m}\chi_{\omega,m}, \end{aligned} \tag{B.10}$$

where

$$B_{\omega,m} = \begin{pmatrix} 0 & \omega_n \\ -\omega_n & 0 \end{pmatrix} \otimes 1 + 1 \otimes \begin{pmatrix} 0 & i\epsilon_m \\ -i\epsilon_m & 0 \end{pmatrix} = \begin{pmatrix} 0 & i\epsilon_m & \omega_n & 0 \\ -i\epsilon_m & 0 & 0 & \omega_n \\ -\omega_n & 0 & 0 & i\epsilon_m \\ 0 & -\omega_n & -i\epsilon_m & 0 \end{pmatrix},$$

$$\chi_{\omega,m} = \left(\chi_{(\omega_n,m,+)}, \chi_{(\omega_n,m,-)}\right)^T. \tag{B.11}$$

The result for the Grassmann integral is

$$Z_{\mathrm{BCS}}^{\mathrm{even}} = \prod_{\omega>0,m} \mathrm{PfB}_{\omega,\mathrm{m}} = \prod_{\omega,\mathrm{m}} (\mathrm{i}\omega_{\mathrm{n}} - \epsilon_{\mathrm{m}}) = \prod_{\mathrm{m}} \exp \sum_{\omega_{\mathrm{n}}} \log(\mathrm{i}\omega_{\mathrm{n}} - \epsilon_{\mathrm{m}}) = \prod_{\mathrm{m}} \left(1 + \mathrm{e}^{-\beta\epsilon_{\mathrm{m}}}\right), \tag{B.12}$$

where we have relabeled the frequencies to include the negative Matsubara frequencies again. We ignore some unimportant prefactor, since finally the quantity to our interest is only related to the ratio of partition function, where the unimportant constant would cancel. On the other hand, for even frequency (odd winding number) case, the partition function is

$$
\begin{aligned}
Z_{\mathrm{BCS}}^{\mathrm{odd}} &= \det(W) \int \mathcal{D}\chi e^{-S}, \\
S &= \frac{1}{2} \sum_{m} \Big(\sum_{\omega_n > 0} \chi_{\omega,m}^{T} B_{\omega,m} \chi_{\omega,m} + \chi_{0,m}^{T} i D_{0m} \chi_{0,m} \Big),
\end{aligned}
\tag{B.13}
$$

where $B_{\omega,m}$ is identical to Eq. (B.11), and iD_m is defined in Eq. (B.4). So the partition function becomes

$$
\begin{aligned}
Z_{\mathrm{BCS}}^{\mathrm{odd}} &= \det(W)\mathrm{PfD} \prod_{\omega_{\mathrm{n}} \neq 0, \mathrm{m}} (\mathrm{i}\omega_{\mathrm{n}} - \epsilon_{\mathrm{m}}) = \det(\mathrm{W})\mathrm{sgnPfD} \prod_{\omega_{\mathrm{n}}, \mathrm{m}} (\mathrm{i}\omega_{\mathrm{n}} - \epsilon_{\mathrm{m}}) \\
&= \text{sign Pf}(\mathrm{A_{sc}}) \prod_{\mathrm{m}} \left(1 - \mathrm{e}^{-\beta\epsilon_{\mathrm{m}}}\right) = \mathrm{P}(\mathrm{H_{BCS}}) \prod_{\mathrm{m}} \left(1 - \mathrm{e}^{-\beta\epsilon_{\mathrm{m}}}\right)
\end{aligned}
\tag{B.14}
$$

where the mod of PfD, i.e. $\prod_m \epsilon_m$, is absorbed in the product of $(i\omega_n - \epsilon_m)$ as $i\omega_n = 0$, and $\mathrm{P}(\mathrm{H_{BCS}})$ is the parity of the ground state of the mean-field superconductor as shown in Eq. (B.1). We see that the BCS partition function depends only on the parity of the winding number $P(n_w)$. In this work, the most relevant quantity is the ratio of the partition function between winding number one and zero, which is

$$
Z_{\mathrm{sc}}^{1} / Z_{\mathrm{sc}}^{0} = \mathrm{P}(\mathrm{H_{BCS}}) \prod_{\mathrm{m}} \tanh(\beta\epsilon_{\mathrm{m}}/2). \tag{B.15}
$$

Appendix C

Partition function and two-point correlation function for a particular winding number sector

In this appendix, we calculate the two-point correlation function for a particular winding number sector. First we show that the total expectation value can always decomposed as weighted sum of expectation value in a particular sector.

The total partition function for the NSN junction can be written as the sum of partition functions in each topological sector:

$$\begin{aligned} Z &= \sum_{n_w} Z_{n_w}, \\ Z_{n_w} &= Z_{\mathrm{BCS}}^{P(n_w)} \int_{n_w} \mathcal{D}\delta\phi e^{-S[\phi]}. \end{aligned} \tag{C.1}$$

Note that Z_{n_w} includes both the partition function of the BCS mean-field SC with anit-periodic or periodic boundary condition and the corresponding phase fluctuations. Thus if we need to calculate the expectation value for any function of the

phase at some particular time point, i.e., $F\left[\{\phi(\tau_i)\}\right]$, the value will be

$$\begin{aligned}\langle F\rangle &= \frac{1}{Z}\sum_{n_w} Z_{sc}^{P(n_w)} \int_{n_w} \mathcal{D}\delta\phi F\left[\{\phi(\tau_i)\}\right] e^{-S[\phi]} = \frac{1}{Z}\sum_{n_w} \frac{\int_{n_w} \mathcal{D}\delta\phi F\left[\{\phi(\tau_i)\}\right] e^{-S[\phi]}}{\int_{n_w} \mathcal{D}\delta\phi e^{-S[\phi]}} Z_{n_w} \\ &= \frac{\sum_{n_w}\langle F\rangle_{n_w} Z_{n_w}}{\sum_{n_w} Z_{n_w}} = \langle F\rangle_0 + \frac{\sum_{n_w\neq 0}\Big(\langle F\rangle_{n_w} - \langle F\rangle_0\Big)\frac{Z_{n_w}}{Z_0}}{1+\sum_{n_w\neq 0}\frac{Z_{n_w}}{Z_0}} \\ &\simeq \langle F\rangle_0 + \Big(\langle F\rangle_1 - \langle F\rangle_0\Big)\frac{Z_1}{Z_0} + (1\to -1) + O\Big(\frac{Z_2}{Z_0}\Big),\end{aligned} \tag{C.2}$$

where the expectation value $\langle F\rangle_{n_w}$ for a specific topological sector n_w is defined as

$$\langle F\rangle_{n_w} = \frac{\int_{n_w} \mathcal{D}\delta\phi F\left[\{\phi(\tau_i)\}\right] e^{-S[\phi]}}{\int_{n_w} \mathcal{D}\delta\phi e^{-S[\phi]}}. \tag{C.3}$$

In the last step of Eq. (C.2), we assume $\frac{Z_{|n_w|\geq 2}}{Z_0} \ll \frac{Z_{\pm 1}}{Z_0} \ll 1$ so that topological sectors with winding number $|n_w|\geq 2$ can be ignored.

To calculate Z_{n_w}, we write the phase trajectory in the specific topological sector n_w as

$$\phi_{n_w}(\tau) = 2\pi n_w \tau/\beta + \delta\phi(\tau), \tag{C.4}$$

where $\delta\phi(\beta) = \delta\phi(0)$, and the action for the topological sector n_w is

$$\begin{aligned}S &= \int_0^\beta d\tau \left(\frac{\dot\phi^2}{4E_c} - iN_g\frac{\dot\phi}{2}\right) + g_0\int_0^\beta \frac{d\tau_1 d\tau_2}{\beta^2}\frac{1-\cos(\phi(\tau_1)-\phi(\tau_2))}{\sin^2(\pi(\tau_1-\tau_2)/\beta)} \\ &= \frac{\pi^2 n_w^2}{\beta E_c} - i\pi n_w N_g + \int_0^\beta d\tau \frac{\delta\dot\phi^2}{4E_c} + g_0\int_0^\beta \frac{d\tau_1 d\tau_2}{\beta^2}\frac{1-\cos(2\pi n_w(\tau_1-\tau_2)/\beta + (\delta\phi(\tau_1)-\delta\phi(\tau_2)))}{\sin^2(\pi(\tau_1-\tau_2)/\beta)}.\end{aligned} \tag{C.5}$$

If the charging effect is weak or intermediate, i.e., $\beta E_c \leq 1$, the phase fluctuation in the action Eq. (C.5) is suppressed. Thus it is legitimate to expand the phase fluctuations in the term proportional to g_0 in Eq. (C.5) up to the quadratic order, such that the g_0-term becomes

$$g_0 \int_0^\beta \frac{d\tau_1 d\tau_2}{\beta^2} \Big[A_0(\tau_1 - \tau_2) + A(\tau_1 - \tau_2)(\delta\phi_1^2 - \delta\phi_1\delta\phi_2) - 2B(\tau_1 - \tau_2)\delta\phi_1 \Big], \quad \text{(C.6)}$$

where

$$\begin{aligned} A_0(\tau) &= \frac{1 - \cos(2\pi n_w \tau/\beta)}{\sin^2(\pi\tau/\beta)}, \\ A(\tau) &= \frac{\cos(2\pi n_w \tau/\beta)}{\sin^2(\pi\tau/\beta)}, \\ B(\tau) &= \frac{\sin(2\pi n_w \tau/\beta)}{\sin^2(\pi\tau/\beta)}. \end{aligned} \quad \text{(C.7)}$$

It is easy to calculate these integrals using Fourier transformation, and the resulting expression for the partition function is

$$Z_{n_w} = Z_{\rm BCS}^{P(n_w)} \exp\Big\{ -\frac{\pi^2 n_w^2}{\beta E_c} - 2g_0|n_w| + i\pi n_w N_g \Big\} \prod_{p_n>0} \frac{\pi}{\frac{\beta p_n^2}{2E_c} + \alpha(ip_n)}. \quad \text{(C.8)}$$

In a similar way, we can calculate the two-point correlation function

$$\mathcal{G}_{n_w}(\tau) = e^{i2\pi n_w \tau/\beta} \langle e^{i[\delta\phi(\tau) - \delta\phi(0)]} \rangle_{n_w} = e^{i2\pi n_w \tau/\beta} \exp\Big\{ -\sum_{p_n} \frac{2 - 2\cos(p_n\tau)}{\frac{\beta p_n^2}{2E_c} + \alpha(ip_n)} \Big\}. \quad \text{(C.9)}$$

At $\tau = \beta/2$,

$$\mathcal{G}_{n_w}(\beta/2) = e^{i\pi n_w} C_{|n_w|}$$
$$C_{|n_w|} = \prod_{p'_n>0} \exp\Big\{ - \frac{1}{\frac{\beta p'^2_n}{8E_c} + g_0(|n'_p| - |n_w|)\Theta(|n'_p| - |n_w|)} \Big\}, \tag{C.10}$$

where $p'_n = 2\pi n'_p/\beta$, with $n'_p = 1, 3, 5, ...$

List of Publications

Publications this thesis is based on:

1. **Chun-Xiao Liu**, J. D. Sau, and S. Das Sarma, *Role of dissipation in realistic Majorana nanowires*, Phys. Rev. B **95**, 054502 (2017).

2. **Chun-Xiao Liu**, J. D. Sau, T. D. Stanescu, and S. Das Sarma, *Andreev bound states versus Majorana bound states in quantum dot-nanowire-superconductor hybrid structures: Trivial versus topological zero-bias conductance peaks*, Phys. Rev. B **96**, 075161 (2017).

3. Hao Zhang, **Chun-Xiao Liu**, Sasa Gazibegovic, *et al.*, *Quantized Majorana Conductance*, Nature , 26142 (2018).

4. **Chun-Xiao Liu**, Jay D. Sau, and S. Das Sarma, *Distinguishing topological Majorana zero modes from trivial Andreev bound states: Proposed tests through differential tunneling conductance spectroscopy*, Phys. Rev. B **97**, 214502 (2018).

5. **Chun-Xiao Liu**, and Jay D. Sau, *Measuring the topological invariant using Coulomb blockaded topological superconductors*, arXiv:1803.01872 (2018).

Other publications and preprints that I contributed to:

1. F. Setiawan, **Chun-Xiao Liu**, J. D. Sau, S. Das Sarma, *Electron temperature and tunnel coupling dependence of zero-bias and almost-zero-bias conductance peaks in Majorana nanowires*, Phys. Rev. B **96**, 184520[Editors' Suggestion] (2017).

2. **Chun-Xiao Liu**, F. Setiawan, J. D. Sau, and S. Das Sarma, *Phenomenology of the soft gap, zero-bias peak, and zero-mode splitting in ideal Majorana nanowires*, Phys. Rev. B **96**, 054520 (2017).

3. **Chun-Xiao Liu**, B. Roy, and J. D. Sau, *Ferromagnetism and glassiness on the surface of topological insulators*, Phys. Rev. B **94**, 235421 (2016).

4. G. Sharma, **Chunxiao Liu**, K. Seo, J. D. Sau, and S. Tewari, *Normal-state Nernst effect from bidirectional bond density wave state in high-T_c cuprates*, Phys. Rev. B **92**, 155114 (2015).

Bibliography

[1] E. Majorana, Il Nuovo Cimento (1924-1942) **14**, 171 (1937).

[2] A. Y. Kitaev, Physics-Uspekhi **44**, 131 (2001).

[3] N. Read and D. Green, Phys. Rev. B **61**, 10267 (2000).

[4] D. A. Ivanov, Phys. Rev. Lett. **86**, 268 (2001).

[5] N. B. Kopnin and M. M. Salomaa, Phys. Rev. B **44**, 9667 (1991).

[6] G. E. Volovik, Journal of Experimental and Theoretical Physics Letters **70**, 609 (1999).

[7] T. Senthil and M. P. A. Fisher, Phys. Rev. B **61**, 9690 (2000).

[8] S. Das Sarma, C. Nayak, and S. Tewari, Phys. Rev. B **73**, 220502 (2006).

[9] C. Nayak, S. H. Simon, A. Stern, M. Freedman, and S. Das Sarma, Rev. Mod. Phys. **80**, 1083 (2008).

[10] P. Bonderson, M. Freedman, and C. Nayak, Phys. Rev. Lett. **101**, 010501 (2008).

[11] P. Bonderson, M. Freedman, and C. Nayak, Annals of Physics **324**, 787 (2009).

[12] J. D. Sau, S. Tewari, and S. Das Sarma, Phys. Rev. A **82**, 052322 (2010).

[13] L. Mazza, M. Rizzi, M. D. Lukin, and J. I. Cirac, Phys. Rev. B **88**, 205142 (2013).

[14] T. Hyart *et al.*, Phys. Rev. B **88**, 035121 (2013).

[15] P. Bonderson, Phys. Rev. B **87**, 035113 (2013).

[16] D. Aasen *et al.*, Phys. Rev. X **6**, 031016 (2016).

[17] D. J. Clarke, J. D. Sau, and S. Das Sarma, Phys. Rev. X **6**, 021005 (2016).

[18] M. Ippoliti, M. Rizzi, V. Giovannetti, and L. Mazza, Phys. Rev. A **93**, 062325 (2016).

[19] L. Fu and C. L. Kane, Phys. Rev. Lett. **100**, 096407 (2008).

[20] J. D. Sau, R. M. Lutchyn, S. Tewari, and S. Das Sarma, Phys. Rev. Lett. **104**, 040502 (2010).

[21] J. D. Sau, S. Tewari, R. M. Lutchyn, T. D. Stanescu, and S. Das Sarma, Phys. Rev. B **82**, 214509 (2010).

[22] R. M. Lutchyn, J. D. Sau, and S. Das Sarma, Phys. Rev. Lett. **105**, 077001 (2010).

[23] Y. Oreg, G. Refael, and F. von Oppen, Phys. Rev. Lett. **105**, 177002 (2010).

[24] J. Alicea, Phys. Rev. B **81**, 125318 (2010).

[25] V. Mourik *et al.*, Science **336**, 1003 (2012).

[26] M. T. Deng *et al.*, Nano Lett. **12**, 6414 (2012).

[27] A. Das *et al.*, Nat. Phys. **8**, 887 (2012).

[28] H. O. H. Churchill *et al.*, Phys. Rev. B **87**, 241401 (2013).

[29] A. D. K. Finck, D. J. Van Harlingen, P. K. Mohseni, K. Jung, and X. Li, Phys. Rev. Lett. **110**, 126406 (2013).

[30] H. Zhang *et al.*, arXiv:1603.04069 (2016).

[31] M. T. Deng *et al.*, Science **354**, 1557 (2016).

[32] J. Chen *et al.*, Science Advances **3** (2017).

[33] F. Nichele *et al.*, Phys. Rev. Lett. **119**, 136803 (2017).

[34] H. Zhang *et al.*, Nature Communications **8**, 16025 EP (2017).

[35] Ö. Gül *et al.*, Nature Nanotechnology (2018).

[36] H. Zhang *et al.*, Nature **556**, 74 EP (2018).

[37] J. Alicea, Rep. Prog. Phys. **75**, 076501 (2012).

[38] M. Leijnse and K. Flensberg, Semicond. Sci. Technol. **27**, 124003 (2012).

[39] T. D. Stanescu and S. Tewari, J. Phys.: Condens. Matter **25**, 233201 (2013).

[40] C. Beenakker, Annu. Rev. Condens. Matter Phys. **4**, 113 (2013).

[41] S. R. Elliott and M. Franz, Rev. Mod. Phys. **87**, 137 (2015).

[42] S. D. Sarma, M. Freedman, and C. Nayak, Npj Quantum Information **1**, 15001 EP (2015).

[43] C. Beenakker and L. Kouwenhoven, Nature Physics **12**, 618 EP (2016).

[44] M. Sato and S. Fujimoto, J. Phys. Soc. Jpn. **85**, 072001 (2016).

[45] R. M. Lutchyn *et al.*, Nature Reviews Materials **3**, 52 (2018).

[46] K. Sengupta, I. Žutić, H.-J. Kwon, V. M. Yakovenko, and S. Das Sarma, Phys. Rev. B **63**, 144531 (2001).

[47] K. T. Law, P. A. Lee, and T. K. Ng, Phys. Rev. Lett. **103**, 237001 (2009).

[48] K. Flensberg, Phys. Rev. B **82**, 180516 (2010).

[49] M. Wimmer, A. Akhmerov, J. Dahlhaus, and C. Beenakker, New Journal of Physics **13**, 053016 (2011).

[50] F. Setiawan, P. M. R. Brydon, J. D. Sau, and S. Das Sarma, Phys. Rev. B **91**, 214513 (2015).

[51] M. Cheng, R. M. Lutchyn, V. Galitski, and S. Das Sarma, Phys. Rev. Lett. **103**, 107001 (2009).

[52] M. Cheng, R. M. Lutchyn, V. Galitski, and S. Das Sarma, Phys. Rev. B **82**, 094504 (2010).

[53] S. Das Sarma, J. D. Sau, and T. D. Stanescu, Phys. Rev. B **86**, 220506 (2012).

[54] D. Rainis, L. Trifunovic, J. Klinovaja, and D. Loss, Phys. Rev. B **87**, 024515 (2013).

[55] E. Prada, P. San-Jose, and R. Aguado, Phys. Rev. B **86**, 180503 (2012).

[56] R. M. Lutchyn, T. D. Stanescu, and S. Das Sarma, Phys. Rev. Lett. **106**, 127001 (2011).

[57] T. D. Stanescu, R. M. Lutchyn, and S. Das Sarma, Phys. Rev. B **84**, 144522 (2011).

[58] A. R. Akhmerov, J. P. Dahlhaus, F. Hassler, M. Wimmer, and C. W. J. Beenakker, Phys. Rev. Lett. **106**, 057001 (2011).

[59] I. C. Fulga, F. Hassler, A. R. Akhmerov, and C. W. J. Beenakker, Phys. Rev. B **83**, 155429 (2011).

[60] C.-H. Lin, J. D. Sau, and S. Das Sarma, Phys. Rev. B **86**, 224511 (2012).

[61] T. D. Stanescu, R. M. Lutchyn, and S. Das Sarma, Phys. Rev. B **87**, 094518 (2013).

[62] T. D. Stanescu, S. Tewari, J. D. Sau, and S. Das Sarma, Phys. Rev. Lett. **109**, 266402 (2012).

[63] A. Vuik, D. Eeltink, A. R. Akhmerov, and M. Wimmer, New Journal of Physics **18**, 033013 (2016).

[64] I. Adagideli, M. Wimmer, and A. Teker, Phys. Rev. B **89**, 144506 (2014).

[65] P. W. Brouwer, M. Duckheim, A. Romito, and F. von Oppen, Phys. Rev. B **84**, 144526 (2011).

[66] P. W. Brouwer, M. Duckheim, A. Romito, and F. von Oppen, Phys. Rev. Lett. **107**, 196804 (2011).

[67] J. D. Sau, S. Tewari, and S. Das Sarma, Phys. Rev. B **85**, 064512 (2012).

[68] W. S. Cole, S. Das Sarma, and T. D. Stanescu, Phys. Rev. B **92**, 174511 (2015).

[69] H.-Y. Hui, J. D. Sau, and S. Das Sarma, Phys. Rev. B **92**, 174512 (2015).

[70] S. Takei, B. M. Fregoso, H.-Y. Hui, A. M. Lobos, and S. Das Sarma, Phys. Rev. Lett. **110**, 186803 (2013).

[71] J. D. Sau and S. Das Sarma, Phys. Rev. B **88**, 064506 (2013).

[72] R. M. Lutchyn, T. D. Stanescu, and S. Das Sarma, Phys. Rev. B **85**, 140513 (2012).

[73] A. M. Lobos, R. M. Lutchyn, and S. Das Sarma, Phys. Rev. Lett. **109**, 146403 (2012).

[74] S. Das Sarma, A. Nag, and J. D. Sau, Phys. Rev. B **94**, 035143 (2016).

[75] S. Albrecht *et al.*, Nature **531**, 206 (2016).

[76] I. Martin and D. Mozyrsky, Phys. Rev. B **90**, 100508 (2014).

[77] A. Yazdani, B. A. Jones, C. P. Lutz, M. F. Crommie, and D. M. Eigler, Science **275**, 1767 (1997).

[78] W. Bauriedl, P. Ziemann, and W. Buckel, Phys. Rev. Lett. **47**, 1163 (1981).

[79] J. R. Schrieffer, *Theory of superconductivity* (Perseus Books, Reading, Massachusetts, 1999).

[80] J. Chen *et al.*, arXiv:1610.04555 (2016).

[81] M. Tinkham, *Introduction to superconductivity* (Dover Publications, Inc. Mineola, New York, 2004).

[82] T. D. Stanescu, J. D. Sau, R. M. Lutchyn, and S. Das Sarma, Phys. Rev. B **81**, 241310 (2010).

[83] J. Liu, A. C. Potter, K. T. Law, and P. A. Lee, Phys. Rev. Lett. **109**, 267002 (2012).

[84] D. Bagrets and A. Altland, Phys. Rev. Lett. **109**, 227005 (2012).

[85] D. Pikulin, J. Dahlhaus, M. Wimmer, H. Schomerus, and C. Beenakker, New J. Phys. **14**, 125011 (2012).

[86] G. Kells, D. Meidan, and P. W. Brouwer, Phys. Rev. B **86**, 100503 (2012).

[87] C. Moore, T. D. Stanescu, and S. Tewari, arXiv:1611.07058 (2016).

[88] E. J. H. Lee *et al.*, Nat. Nanotechnol. **9**, 79 (2014).

[89] C.-X. Liu, J. D. Sau, T. D. Stanescu, and S. Das Sarma, Phys. Rev. B **96**, 075161 (2017).

[90] E. Prada, R. Aguado, and P. San-Jose, Phys. Rev. B **96**, 085418 (2017).

[91] D. J. Clarke, Phys. Rev. B **96**, 201109 (2017).

[92] M. Deng *et al.*, arXiv:1712.03536 (2017).

[93] A. Altland and M. R. Zirnbauer, Phys. Rev. B **55**, 1142 (1997).

[94] S. Mi, D. Pikulin, M. Marciani, and C. Beenakker, JETP **119**, 1018 (2014).

[95] G. W. Semenoff and P. Sodano, arXiv preprint cond-mat/0601261 (2006).

[96] S. Tewari, C. Zhang, S. Das Sarma, C. Nayak, and D.-H. Lee, Phys. Rev. Lett. **100**, 027001 (2008).

[97] J. Ulrich and F. Hassler, Phys. Rev. B **92**, 075443 (2015).

[98] T. I. Ivanov, Phys. Rev. B **96**, 035417 (2017).

[99] L. Fu, Phys. Rev. Lett. **104**, 056402 (2010).

[100] A. Yacoby, M. Heiblum, D. Mahalu, and H. Shtrikman, Phys. Rev. Lett. **74**, 4047 (1995).

[101] G. Hackenbroich and H. A. Weidenmüller, Phys. Rev. Lett. **76**, 110 (1996).

[102] K. Kobayashi, H. Aikawa, S. Katsumoto, and Y. Iye, Phys. Rev. Lett. **88**, 256806 (2002).

[103] M. Sigrist *et al.*, Phys. Rev. Lett. **96**, 036804 (2006).

[104] K. Kobayashi, H. Aikawa, A. Sano, S. Katsumoto, and Y. Iye, Phys. Rev. B **70**, 035319 (2004).

[105] S. Gazibegovic *et al.*, Nature **548**, 434 EP (2017).

[106] S. Vaitiekėnas *et al.*, arXiv:1802.04210 (2018).

[107] F. Krizek *et al.*, arXiv:1802.07808 (2018).

[108] F. W. J. Hekking, L. I. Glazman, K. A. Matveev, and R. I. Shekhter, Phys. Rev. Lett. **70**, 4138 (1993).

[109] V. Ambegaokar, U. Eckern, and G. Schön, Phys. Rev. Lett. **48**, 1745 (1982).

[110] M. T. Tuominen, J. M. Hergenrother, T. S. Tighe, and M. Tinkham, Phys. Rev. Lett. **69**, 1997 (1992).

[111] L. Glazman and K. Matveev, JETP Lett **51** (1990).

[112] R. M. Lutchyn and L. I. Glazman, Phys. Rev. Lett. **119**, 057002 (2017).

[113] M. V. Feigelman, A. Kamenev, A. I. Larkin, and M. A. Skvortsov, Phys. Rev. B **66**, 054502 (2002).

[114] A. Altland and B. D. Simons, *Condensed Matter Field Theory* (Cambridge University Press, 2010).

[115] N. Nagaosa, *Quantum Field Theory in Condensed Matter Physics* (Springer Science & Business Media, 2013).

[116] E. Bascones, C. P. Herrero, F. Guinea, and G. Schön, Phys. Rev. B **61**, 16778 (2000).

[117] J. D. Sau, B. Swingle, and S. Tewari, Phys. Rev. B **92**, 020511 (2015).

[118] S. Rubbert and A. R. Akhmerov, Phys. Rev. B **94**, 115430 (2016).

[119] C.-K. Chiu, J. D. Sau, and S. Das Sarma, Phys. Rev. B **97**, 035310 (2018).

[120] C. W. J. Beenakker, Rev. Mod. Phys. **69**, 731 (1997).

[121] M. P. Anantram and S. Datta, Phys. Rev. B **53**, 16390 (1996).

[122] O. Entin-Wohlman, Y. Imry, and A. Aharony, Phys. Rev. B **78**, 224510 (2008).

[123] Y. Huang, F. Setiawan, and J. D. Sau, Phys. Rev. B **97**, 100501 (2018).